Persistent Luminescence in Strontium Aluminate: a Roadmap to a Brighter Future

David van der Heggen, Jonas J Joos, Ang Feng, Verena Fritz, Teresa Delgado, Nando Gartmann, Bernhard Walfort, Daniel Rytz, Hans Hagemann, Dirk Poelman, et al.

Persistent Luminescence in Strontium Aluminate: a Roadmap to a Brighter Future

David Van der Heggen*[1], Jonas J. Joos*[1], Ang Feng[1], Verena Fritz[1], Teresa Delgado[2], Nando Gartmann[3], Bernhard Walfort[3], Daniel Rytz[4] Hans Hagemann[5], Dirk Poelman[1], Bruno Viana[2], Philippe F. Smet[1]

[1] LumiLab, Department of Solid State Science, Ghent University, Krijgslaan 281/S1, 9000 Gent, Belgium / email: david.vanderheggen@ugent.be; jonas.joos@ugent.be; philippe.smet@ugent.be

[2] PSL Research University, Chimie ParisTech, IRCP, CNRS, Paris, 75005, France

[3] LumiNova AG, Speicherstrasse 60a, CH-9053, Teufen, Switzerland

[4] BREVALOR, Impasse des Frenes 1, CH-1669, Les Sciernes, Switzerland

[5] Département de Chimie Physique, Université de Genève, 30, quai E. Ansermet, CH 1211, Geneva 4, Switzerland

* Both authors contributed equally

Contents

1 Introduction **3**

2 The strontium aluminate host **7**

2.1 The SrO - Al_2O_3 phase diagram 7

2.2 Crystallography 7

3 Dopant incorporation in strontium aluminate **9**

3.1 The europium activator 9

3.2 Trivalent lanthanide codopants . . . 13
3.3 The role of boron: inert flux or active dopant? . . . 15
3.4 Synthesis . . . 18

4 Phenomena related to trapping and energy storage 20
4.1 Thermoluminescence . . . 20
4.2 Optically stimulated luminescence . . . 28
4.3 Mechanoluminescence . . . 31

5 Identifying the requirements for a correct model from experiments 37
5.1 The role of europium . . . 38
5.2 Electron or hole trapping? . . . 39
5.3 Local or global model? . . . 40
5.4 Nature of the trapping defects . . . 42

6 Energy level models for persistent luminescence 46
6.1 General theoretical considerations . . . 48
6.1.1 Orbital vs. multi-particle energy level schemes . . . 48
6.1.2 Trap depths and transition probabilities in global and local models . . . 51
6.2 Examples . . . 54
6.2.1 A global single-electron model . . . 54
6.2.2 A local multiparticle model . . . 56

7 Benchmarking: where do we stand? 58

8 Conclusions and perspective 62

Abstract

Glow-in-the-dark materials have been around for a long time. While formerly materials had to be mixed with radioactive elements to achieve a sufficiently long and bright afterglow, these have now been replaced by much safer alternatives. Notably $SrAl_2O_4$, doped with europium and dyspro-

sium, has been discovered over two decades ago and since then the phosphor has transcended its popular use in watch dials, safety signage or toys with more niche applications in e.g. stress sensing, photocatalysis, medical imaging or flicker-free light emitting diodes. A lot of research efforts are focused on further improving the storage capacity of $SrAl_2O_4$:Eu^{2+},Dy^{3+}, including in nanosized particles, and on finding the underlying physical mechanism to fully explain the afterglow in this material and related compounds. Here we present an overview of the most important results from the research on $SrAl_2O_4$:Eu^{2+},Dy^{3+} and discuss different models and the underlying physics to explain the trapping mechanism at play in these materials.

Keywords: Persistent luminescence, Strontium aluminate, Thermoluminescence, Optically stimulated luminescence, Mechanoluminescence

1 Introduction

Inorganic luminescent materials or phosphors have been around for a long time. Initially they were applied in fluorescent light bulbs, cathode ray tubes or electroluminescent displays but over the last decade they became increasingly important with the development and commercialisation of e.g. solid state lighting [1] and LED displays. [2] These phosphors are composed of an inorganic host with a wide band gap to which impurity ions are intentionally added. The luminescence is the result of localized transitions between electronic levels of the impurity center, often called the activator. The spectral characteristics of phosphors are determined mainly by the selected dopant ion, but interactions of the dopants with the host crystal give opportunities to tune transition energies and probabilities due to splitting and shifting of energy levels. [3] This is for example the case in the class of Eu^{2+}-doped strontium aluminates where the emission color resulting from the $4f^6 5d^1 - 4f^7$ transitions in Eu^{2+} can vary from the near ultraviolet (UV) to the red (see Figure 1), depending on the exact stoichiometry, i.e. the SrO:Al_2O_3 ratio. [4]

Specific dopant(s)-host combinations can also give rise to additional functionalities such as energy and charge transfer processes or quenching of the luminescence. Provided that an appropriate (trapping) defect is added to a luminescent material it can acquire the possibility to temporarily store energy after absorption of excitation light. This energy storage leads to the delayed emission

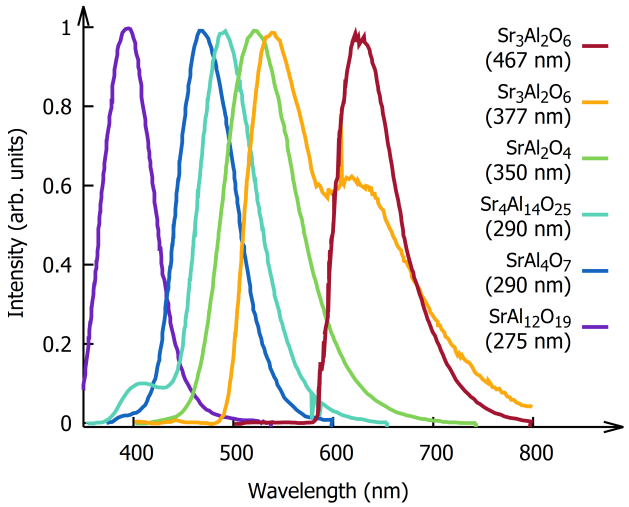

Figure 1: Emission spectra of Eu^{2+} in different strontium aluminates with a varying $SrO:Al_2O_3$ ratio. Spectra were recorded at 300 K except for $Sr_3Al_2O_6$:Eu which was recorded at 4 K. Excitation wavelengths are indicated between brackets. Republished with permission from the Royal Society of Chemistry, from Dutczak *et al.*. [4]

which is called persistent luminescence or long afterglow and which can last from seconds to hours after the excitation has stopped. [5] Phenomena such as persistent luminescence are often the result of a subtle balance between hard-to-assess microscopic properties such as bond lengths and vibrational frequencies or the presence of defects in the vicinity of the active centers. Hence, those additional functionalities are hard to predict via empirical rules or structure-property relationships, in stark contrast to the tuning of known electronic transitions of the activator. [6]

Many afterglow phosphors have been developed with emission ranging from the UV, usually relying on Pr, Gd or Bi luminescence, [7–11] to the infrared where Cr- and Mn-doped phosphors serve as the workhorse. [12–15] The most efficient afterglow phosphors that emit in the visible spectrum are aluminates, silicates or sulfides which are doped with europium and a suitable trivalent lanthanide. [16–20] Many of these phosphors are commercially available but the most encountered afterglow phosphor is still $SrAl_2O_4$:Eu^{2+},Dy^{3+}. It was first reported over two decades ago, in 1996, by Matsuzawa *et al.* [21], and really kickstarted persistent phosphor research. Thanks to the addition of Dy^{3+} the phosphor's initial brightness and afterglow time increased spectacularly and the intense bright green afterglow resulted in a steady increase in the number of possible applications of the phosphor.

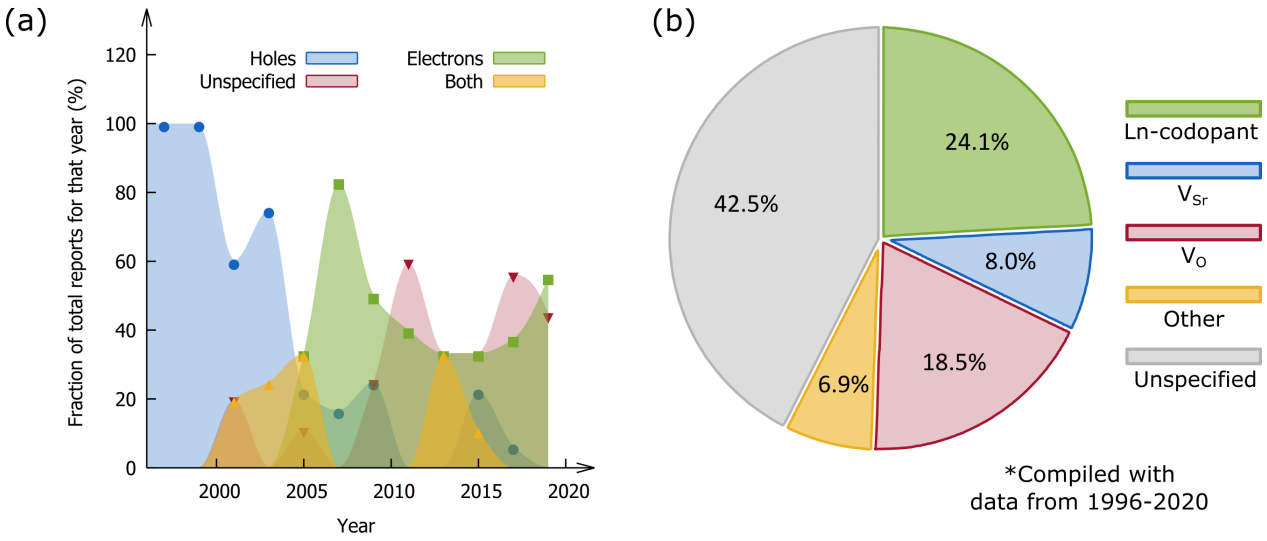

Figure 2: Overview of the proposed mobile charge carriers (a) and trapping defects (b) involved in the afterglow mechanism in strontium aluminates. Both graphs have been constructed using the data presented in all cited references published between 1996 and 2020. Although this reference list is limited in size (78 publications), the results are representative for the general trends in the field of persistent luminescence.

Afterglow phosphors, such as $SrAl_2O_4$:Eu^{2+},Dy^{3+}, have now steadily grown beyond their use in safety signage and the list of proposed applications includes their use in road markings, [22–24] fingerprint identification [25], dye-sensitized solar cells, [26, 27] dosimeters, [28, 29] light sensors, [30] photocatalysis [31] or alternating current driven solid state lighting. [32, 33] In case of $SrAl_2O_4$:Eu^{2+},Dy^{3+}, the material's mechanoluminescent properties make it perfectly suited for structural health testing and the visualization of stress and crack propagation. [34–41] Moreover, nanosized $SrAl_2O_4$:Eu^{2+},Dy^{3+} has the potential to be used in bioimaging and diagnostic applications. [42–44] With these applications in mind, Terraschke *et al.* [45] recently coated magnetite (Fe_3O_4) nanoparticles with $SrAl_2O_4$:Eu^{2+},Dy^{3+} to allow for a combination of magnetic and optical imaging and *in situ* manipulation of relevant biomolecules. Moreover, persistent emission (10 minutes) in the near infrared (NIR) was reported the first time in 2009 for $SrAl_2O_4$ codoped with Eu^{2+},Dy^{3+} and Er^{3+}. The NIR emission is obtained from the energy transfer from Eu^{2+} to Er^{3+}. [46] Nanoparticles of $SrAl_2O_4$ do not appear to be cytotoxic, [47] which is an important condition for potential biological applications.

Regardless of the long list of promising applications and interesting proofs-of-concept, the per-

formance of the state-of-the-art materials appears to be lagging behind the ambitions and the performance of $SrAl_2O_4$:Eu^{2+},Dy^{3+} has only moderately improved since 1996. Huge leaps forward are needed to meet the afterglow intensities and durations required for most proposed applications. Except for some coarse mechanistic insights, the hidden variables that drive the persistent luminescence are still largely unknown as is apparent from literature. To illustrate this, the physical models proposed in the cited references from 1996 to 2020 have been examined more closely. Figure 2(a) shows the time evolution of the proposed charge carriers involved in the trapping, while Figure 2(b) summarizes which trapping defects are supposedly involved. It is clear from the multitude of options, together with the large fraction attributed to an unspecified defect, that the details of the microscopic model are still poorly understood. This can partly be attributed to a poor reproducibility in material synthesis and seemingly conflicting experimental results, but is also a consequence of drawing too far-going conclusions from experiments that can be explained in multiple ways.

This review aspires to present a critical overview of the state-of-the-art, linking different experimental results together. We will also suggest unconventional lines of thought with the goal to further our insight into persistent luminescence in aluminates and steer future experimental and theoretical research. As such, we approach the topic from another angle compared to existing related overview articles on synthesis [48], the relation between host stoichiometry and Eu^{2+} emission characteristics [4] and applications of persistent phosphors [18, 49, 50]

We start by briefly discussing those aspects of the host's crystallography that are important for the luminescence in $SrAl_2O_4$. Subsequently we describe dopant incorporation in the host, not only considering the europium activator and trivalent lanthanide codopants, but also the widely used boron flux. [51] Within this context the effect of these dopants on the photoluminescence in $SrAl_2O_4$ will be discussed as well. Next an overview of the thermoluminescence, optically stimulated luminescence and mechanoluminescence in singly doped and codoped $SrAl_2O_4$ will be given and some of the key findings concerning the trapping mechanism will be discussed. Finally, based on these experimental findings, requirements for an adequate model for the persistent luminescence mechanism are drafted. Different microscopic models and the underlying physics are discussed, focussing on which phenomena can be explained by which models. Finally, objective measures to unambiguously quantify persistent luminescence performance are listed and applied to a benchmarking study where

the commercial state-of-the-art afterglow phosphors are compared.

2 The strontium aluminate host

2.1 The SrO - Al_2O_3 phase diagram

The crystal chemistry of the SrO - Al_2O_3 system has been thoroughly investigated by Massazza [52] and Ganits *et al.* [53] who found five stable compounds: $Sr_4Al_2O_7$ (S_4A), $Sr_3Al_2O_6$ (S_3A), $SrAl_2O_4$ (SA), $SrAl_4O_7$ (SA_2) and $SrAl_{12}O_{19}$ (SA_6). The notation used to refer to every compound corresponds to the amount of SrO (S) or Al_2O_3 (A) constituents. The reported phase diagrams are similar but differ in melting temperatures. Later, Capron *et al.* [54] proposed a modification of the phase diagram to address the findings that SA_2 becomes metastable at temperatures above 1100 °C forming the closely related orthorhombic $Sr_4Al_{14}O_{25}$ (S_4A_7) which was included as a sixth compound. The resulting SrO - Al_2O_3 phase diagram, including the two phase transitions [55,56] of $SrAl_2O_4$, is shown in Figure 3. Other compositions have been reported but their stability remains uncertain at this point. Of these compounds only $SrAl_2O_4$ and $Sr_4Al_{14}O_{25}$ exhibit excellent afterglow properties in the green and blue ranges upon doping with Eu^{2+} and Dy^{3+}. Because of the vast amount of research already performed on $SrAl_2O_4$ and its high applicability, largely owing to a good overlap between the emission phosphor's emission and the human eye sensitivity, the remainder of this review will focus on this composition. However, given the large similarity between these hosts, it is plausible that many conclusions drawn for $SrAl_2O_4$ are transferable to other phases.

2.2 Crystallography

At room temperature $SrAl_2O_4$ is made up of monoclinic crystals (space group $P2_1$) resembling a distorted stuffed tridymite structure. The structure was first described in detail by Schulze and Buschbaum [57] and is built from rings consisting of six corner-sharing [AlO_4] tetrahedra stacked on top of each other and forming large channels. Strontium ions occupy two nonequivalent sites with low symmetry (C_1 point group) inside these channels. As pointed out by Joos *et al.* [58] and as shown in Figure 4 the large variations in Sr-O distances make it difficult to unambiguously define a coordination shell for Sr and accordingly reported coordination numbers vary between 6

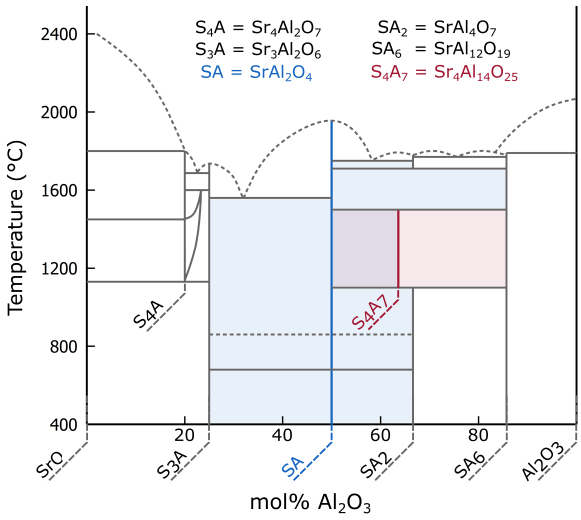

Figure 3: Binary phase diagram of the SrO-Al_2O_3 system compiled according to the work of Massazza, [52] Ganits *et al.* [53] and Capron *et al.* [54]. The two phase transitions of $SrAl_2O_4$ have been added as well. [55, 56]

and 9. [57, 59, 60] The effective coordination number, in which a weighing of the different bond lengths is carried out, is slightly larger than 6 for both sites. [58, 61]

At 650-680°C, $SrAl_2O_4$ undergoes a phase transition from the monoclinic to a hexagonal phase. [55, 62,63] It was originally reported that the hexagonal phase had $P6_322$ symmetry but recently Avdeev *et al.* [56] identified an additional, second order phase transition at 860 °C. Their results indicate that the $P6_322$ symmetry is only achieved above 860°C and that the symmetry following the first phase transition at 650°C is lower than originally suggested and corresponds to a $P6_3$ space group. The phase transitions are reversible and attempts to stabilize the hexagonal phase by quenching the phosphor using liquid nitrogen were unsuccessful. [55]

Stabilization of the hexagonal phase at room temperature can however be achieved in other ways. $BaAl_2O_4$ crystallizes in a hexagonal phase (space group $P6_322$) and incorporation of barium into $SrAl_2O_4$ has been proven to lower the monoclinic to hexagonal phase transition temperature already at low Ba concentrations. In effect, the hexagonal phase can be stabilized at room temperature for Ba:(Sr+Ba) ratios approaching 50%. [64] The addition of SiO_2 results in the formation of $Sr_{1-x/2}Al_{2-x}Si_xO_4$:$Eu^{2+}$$Dy^{3+}$which crystallizes in a purely hexagonal form for $x \geq 0.1$ while maintaining the green emission color at low silica concentrations. [65] Other reports indicate that

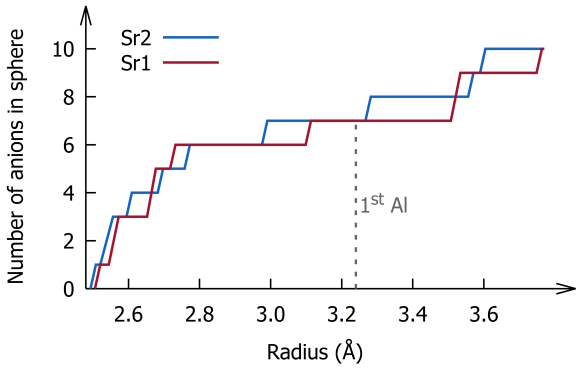

Figure 4: Illustration of the number of oxygen anions contained inside a sphere centered at the strontium sites as a function of the radius of the sphere for $SrAl_2O_4$. Reprinted from Joos *et al.* [58] with permission from Elsevier.

the hexagonal phase can be stabilized in nanoparticles, even without addition of Ba or Si, showing that the size of the particles is an important parameter for the resulting crystallography. [66–68] Nevertheless hexagonal $SrAl_2O_4$:Eu^{2+},Dy^{3+} remains quite rare and most commercial applications and research deal with powders which are mostly monoclinic. Therefore we will mainly be concerned with the monoclinic phase of $SrAl_2O_4$ for the remainder of this work.

3 Dopant incorporation in strontium aluminate

The undoped strontium aluminate host displays some radio- and thermoluminescence following X-ray irradiation. This luminescence is attributed to intrinsic defects such as F-centers and F_2-centers and trace metal impurities such as Mn^{4+} and Cr^{3+}. [69] The signals are largely quenched at room temperature and their intensity remains far below what is achieved in $SrAl_2O_4$:Eu^{2+},Dy^{3+} whose spectral properties are the result of purposely introduced lanthanide dopant ions. Because the spectral characteristics are to a large extent determined by the interplay between the dopants and the host, the incorporation of the dopants in the host matrix will now be discussed in detail.

3.1 The europium activator

Given the identical oxidation state and the nearly identical effective ionic radii of Sr^{2+} and Eu^{2+} (1.31 Å vs. 1.30 Å, both for 9-fold coordination) [70] it is reasonable to assume that Eu^{2+} will substitute for Sr^{2+} when incorporated in $SrAl_2O_4$. There are two nonequivalent alkaline earth

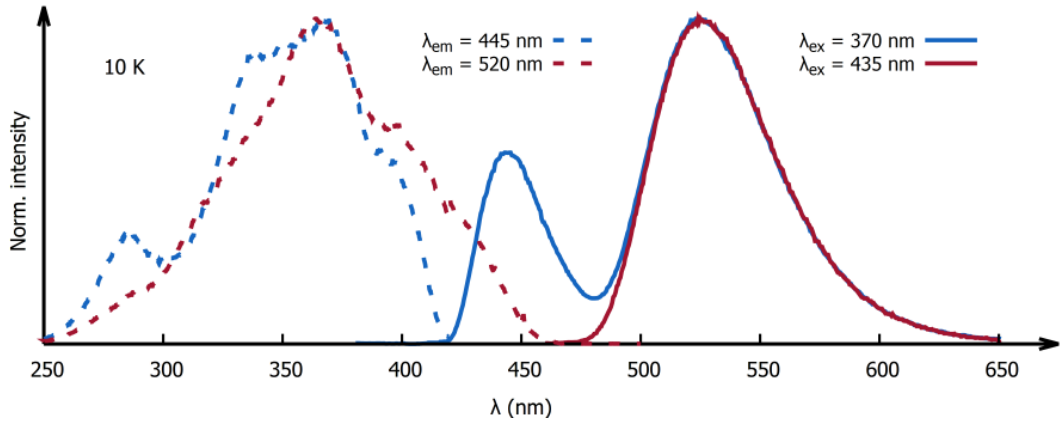

Figure 5: Excitation and emission spectra of $SrAl_2O_4$:Eu^{2+},Dy^{3+} recorded at 10K. Reproduced with permission from Botterman *et al.*. [59] Copyright 2014 by the American Physical Society.

sites in the crystal (see Figure 4) and electron paramagnetic resonance spectroscopy (EPR) results confirm the incorporation of Eu^{2+} on two highly asymmetric sites in the host. [71–73] It can thus be expected that the incorporation of Eu^{2+} will lead to an emission spectrum consisting of at least two contributions. First evidence for this was found by Poort *et al.* [74] who measured the emission spectrum of $SrAl_2O_4$:Eu^{2+} at 4.2 K and found that in addition to the characteristic green emission band, which peaks at around 520 nm and manifests itself at room temperature, a blue emission band appears when the temperature is sufficiently lowered, as shown in Figure 5. This blue emission band peaks around 445 nm and quenches around 200 K so that it is not visible at room temperature. [4, 59, 74, 75] Part of this thermal quenching can be accounted for by energy transfer between the two nonequivalent luminescent centers. [74, 76] This energy transfer is concentration dependent and the critical radius has been estimated to be around 20 Å. [74, 76, 77]

The green emission is characterized by a much higher quenching temperature of 440 K [4] and concentration quenching only sets in at Eu concentrations around 6% . [77–79] At low temperature, both emission bands have a comparable intensity in samples with a low activator concentration from which Poort *et al.* [74] concluded that Eu^{2+} is equally likely incorporated on both Sr sites. However, one should be careful when interpreting this statement as the intensity ratio of both emission bands is highly temperature, concentration and excitation wavelength dependent. [76]

As some authors noted, there is the apparent inconsistency that the spectroscopic properties such as the Stokes shift and bandwidth of the two emission bands are very different while it is

evident from Figure 4 that the oxygen coordination of the Sr1 and Sr2 sites is nearly identical with only small variations in the Sr-O distances. [58] Poort *et al.* [74] tried to explain this by assuming a preferential orientation of the $5d$-orbitals on one of the two Sr sites, effectively lowering the energy of the green emission. [74] However, several authors disproved this theory and showed that the changes in crystal field, due to the small variations in the Sr-O bond lengths on both sites, can in fact account for the large differences in spectroscopic properties between the two emission bands. [59, 80–83] Botterman *et al.* [59] concluded this by means of simple empirical relations that connect the $4f^7 - 4f^6 5d^1$ energy gap with bond lengths in the pristine crystal. [84, 85] While these rules allow to appreciate the magnitude of the effect, they fail to make the correct assignment and more advanced theoretical methods are desirable. By combining hybrid density functional theory for ground-state structure relaxation and multiconfigurational *ab initio* calculations to assess the excited states of embedded $(CeO_9Al_4)^{3-}$ clusters, Shi *et al.* [81] derived that the $4f^1 - 5d^1$ gap is larger for Ce_{Sr1} than for Ce_{Sr2}, suggesting the same energy order for the associated Eu^{2+} centers relying on another empirical rule between the Eu^{2+} $4f^7 - 4f^6 5d^1$ and Ce^{3+} $4f^1 - 5d^1$ excitation energies. [86] More recently, Ning *et al.* [80] performed similar calculations directly on embedded EuO_9^{16-} clusters, confirming the findings of Shi *et al.* leading to the final assignment of the green emission to a Eu_{Sr2} center and the (at room temperature thermally quenched) blue emission to a Eu_{Sr1} center.

An alternative explanation for the origin of the blue emission is due to Clabau *et al.* [87] who proposed that the high energy emission can be attributed to a charge transfer from oxygen to Eu^{3+}. Considering the importance of a correct interpretation of the emission spectrum of $SrAl_2O_4$:Eu^{2+} we will briefly discuss some of the observations that led them to propose this alternative explanation:

1/ It was noticed that the emission spectrum of $SrAl_2O_4$:Eu^{2+} prepared under oxidizing conditions shows no trace of green emission while the blue emission band can still be observed at low temperature. [87] These oxidizing conditions favor the formation of Eu^{3+} and it was argued that it is improbable that partial reduction of europium takes place on only one of the two Sr sites. Hence the authors postulated that the absence of the green emission can be seen as proof that europium is only incorporated in its trivalent form. From this it was deduced that the blue emission must be related to Eu^{3+} instead of Eu^{2+}. However, this argument tacitly assumes that there is no preferential

occupation of the dopants in the crystal which is not necessarily the case. More recent work on the incorporation of Eu in $S_4Al_{14}O_{25}$ has for example shown that Eu^{2+} is preferentially incorporated on the most symmetric Sr-site. [88] Additionally it was suggested that another lanthanide, Ce^{3+}, is preferentially incorporated on the smaller Sr2 site. [81] These results indicate that the two sites are sufficiently different to plausibly explain these observed differences between the green and blue emission bands.

2/ Clabau *et al.* noticed that the intensity of the green emission decreases more than the intensity of the blue emission upon incorporation of Dy^{3+} while the incorporation of Y^{3+} has the opposite effect. [87] Based on the fact that these two dopants act differently on the two emission bands it was again postulated that the origin of the emissions must be different as well. This observation can however be attributed to two physically different mechanisms. Considering the radically different quenching temperatures of the two emission bands it can be expected that the blue emission, which quenches around 200 K, will be more sensitive to the changes in the local environment than the green emission that quenches only at 440 K. This is supported by wavelength-dependent quantum efficiency measurements by Delgado *et al.* [89] showing that the effect of Dy^{3+} incorporation on the quantum efficiency is more pronounced for shorter excitation wavelengths which also excite the blue emission. Consequently the blue band's intensity will show larger variations upon trivalent lanthanide incorporation than the green band. This effect is expected to be rather independent of the codopant and explains why the blue band quenches more than the green band upon Y^{3+} incorporation. To understand why Dy^{3+} incorporation has the opposite effect we need to take a closer look at the trapping mechanism in the material. The big difference between Y^{3+} and Dy^{3+} is that the former is not directly involved in trapping whereas the latter likely is (see §5.4). The large differences in trapping characteristics between the two different europium centers [59] in combination with the decrease in quantum efficiency due to optically stimulated luminescence by excitation light and the charging effects related to trapping, can account for the stronger decrease in emission intensity of the green band upon Dy^{3+} incorporation. [90]

3/ At 4.2 K Clabau *et al.* [87] found decay times of 0.7 µs and 1.7 µs for the blue and green emission respectively and concluded that this difference is large enough to claim that the origin of the blue and green emission must be a different type of electronic transition. [87] However, Bierwagen

et al. [76] found different values for the decay times: 0.8 µs and 1.2 µs for the blue and green emissions respectively. These decay times are more in line with the findings in other works. [4, 59] Moreover, the difference between 0.8 µs and 1.2 µs can be explained by the wavelength-dependency of the decay time. [91, 92] Additionally Bierwagen *et al.* found that energy transfer considerably shortens the decay time of the blue emission, even at low temperature, while the decay time of the green emission remains constant as a function of the Eu concentration. [76] The relatively high Eu concentration (2%) used by Clabau *et al.* facilitates this energy transfer and allows to explain the large difference between the two decay times. [87]

In general, the hypothesis that the blue emission is completely unrelated to Eu^{2+} fails to account for the excitation spectrum of the blue emission which has all the characteristics of a Eu^{2+} spectrum (Figure 5). [93] Based on this observation, it was also suggested to attribute the blue band to emission from a higher $4f^6 5d^1$ level of the same Eu^{2+} center [94] but given the high density of states in the $4f^6 5d^1$ manifold and the associated rapid non-radiative relaxation it seems very unlikely that emission from any level but the lowest can arise. [93]

Given the above discussion we can rather confidently conclude that Eu^{2+} is incorporated on both Sr sites and that the green emission can be assigned to a Eu_{Sr2} center while the blue emission can be assigned to a Eu_{Sr1} center.

3.2 Trivalent lanthanide codopants

Since Matsuzawa *et al.* [21] discovered that codoping $SrAl_2O_4$:Eu^{2+} with Dy^{3+} spectacularly enhances the afterglow properties it has become common practice to add trivalent lanthanides as a codopant to $SrAl_2O_4$:Eu^{2+}. [95–97] Based on charge-neutrality arguments it was initially postulated that these trivalent lanthanides occupy Al^{3+} sites. [98] However, the incorporation of trivalent lanthanides on a 4-fold coordinated site has not been reported in inorganic hosts and based on the size-matching criterion it seems improbable that the trivalent lanthanides, with ionic radii varying from 1.01 Å to 0.868 Å (from Ce^{3+} to Yb^{3+}, for 6-fold coordination), would substitute for Al^{3+} that has an ionic radius of only 0.39 Å (4-fold coordinated). [70] It is therefore generally assumed that trivalent lanthanides occupy the larger Sr sites. Literature on the subject is limited but given the similar chemical behavior of the lanthanides, chemical information extracted for one codopant

can to some extent be generalized to other Ln^{3+} ions.

Nakamura *et al.* [99] investigated the incorporation of Gd^{3+} in $SrAl_2O_4$ using W-band EPR. They found two overlapping signals which could be identified as coming from Gd^{3+} on two nonequivalent sites. Given that there are four nonequivalent aluminum sites in the material as opposed to only two alkaline earth sites it can be postulated that Gd^{3+} does not substitute for Al^{3+} but rather occupies both possible Sr sites. This is further supported by the relatively large zero-field splitting which evidences the incorporation of Gd^{3+} on low-symmetry sites.

Similar conclusions were drawn by Delgado *et al.* [100] who investigated the photoluminescence of $SrAl_2O_4$:Dy^{3+} and found that the $^4F_{9/2}$ - $^6H_{13/2}$ transition, corresponding to the most intense emission peak of Dy^{3+} centered around 568 nm, is split into at least nine lines while a maximum of seven lines would be expected if Dy^{3+} was occupying a single crystallographic site. From these results it can be concluded that Dy^{3+} is incorporated on at least two nonequivalent sites but the experimental limitations together with the high dopant concentration of 5 mol% which might favor dopant clustering, make it difficult to unambiguously determine the exact number of crystallographic sites that Dy^{3+} is occupying.

Finally, analysis of Ce^{3+} luminescence in $SrAl_2O_4$ showed the existence of two distinct Ce^{3+} centers, exhibiting different emission and excitation spectra. [81, 101]

Based on the experimental evidence indicating that Gd^{3+}, Dy^{3+} and Ce^{3+} are incorporated on the alkaline earth sites, it seems reasonable to assume that all trivalent lanthanides are incorporated in a similar manner. However, solubility of trivalent lanthanides (Ln) in $SrAl_2O_4$ is small and segregation into secondary phases such as $LnAlO_3$, has been reported at concentrations as low as 1 mol%. [102, 103] Dy-clustering has also been observed near grain boundaries (Figure 6) where it forms an aluminum poor phase. [103] Moreover, extended X-ray absorption fine structure (EXAFS) measurements on rare-earth-doped $CaAl_2O_4$ indicate that dopant aggregation at the microscopic scale can even take place at relatively low dopant concentrations of 1 mol%. [104] Especially for non-isovalent substitutions, i.e. when charge-compensating defects are generated, a stochastic distribution of dopants is an unjustified assumption [105–107].

The effect of codoping with trivalent lanthanides on the Eu^{2+} photoluminescence spectra is limited. [96] Some authors mention a redshift of 10 nm of the blue luminescence upon Dy^{3+} incor-

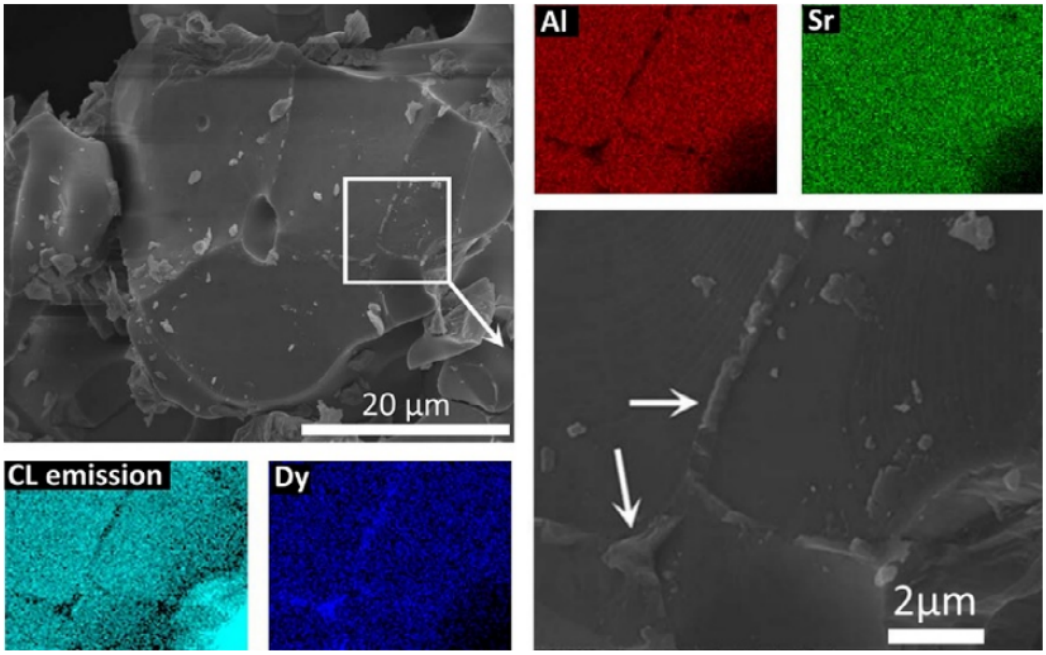

Figure 6: SEM cross section of a $SrAl_2O_4$:Eu^{2+},Dy^{3+} phosphor grain, with elemental maps obtained by EDX for Dy, Al and Sr. The precipitation of Dy at the grain boundaries is clearly visible. The cathodoluminescence (CL) intensity at the grain boundaries is also much weaker. Reprinted from Smet *et al.* [103] with permission from Elsevier.

poration in single crystals [89,108] but as Delgado *et al.* [89] pointed out, no measurable shift occurs in powder samples. This effect is most likely related to a change in absorption characteristics of the phosphor in combination with the comparably high optical path length in single crystals compared to powders. In contrast, the green emission band shows no shift upon trivalent lanthanide incorporation.

3.3 The role of boron: inert flux or active dopant?

Boron trioxide (B_2O_3) and boric acid (H_3BO_3) are widely used as fluxes during the synthesis of inorganic compounds such as aluminates, [109,110] silicates, [111] titanates, [112] thioaluminates [113] and oxysulfides. [114] The addition of the flux enhances the crystallinity of the phosphors, helps to stabilize certain crystallographic phases and lowers the overall reaction temperature, ultimately leading to enhanced luminescent properties. [115, 116] Matsuzawa *et al.* [21] already used B_2O_3 as a flux for $SrAl_2O_4$:Eu^{2+},Dy^{3+} in 1996 but Chen and Chen [117] were the first to systematically investigate the effect of boron addition on the luminescent properties of $SrAl_2O_4$:Eu^{2+},Dy^{3+} in 2001.

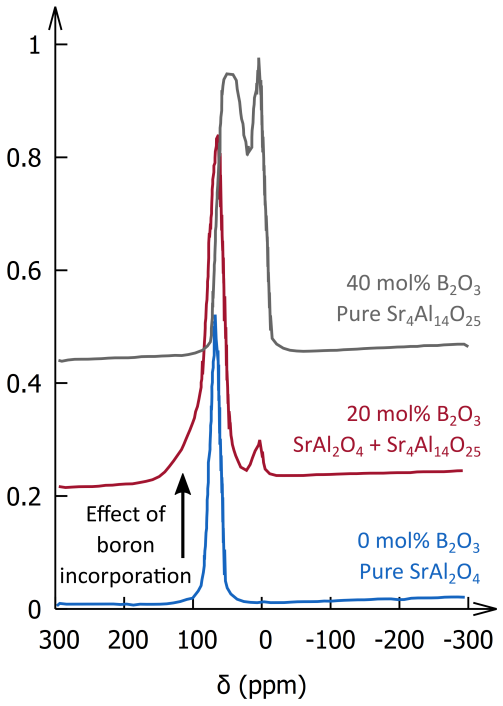

Figure 7: ^{27}Al MAS NMR spectra of three samples prepared with different amounts of B_2O_3 Reprinted from Nag and Kutty [51] with permission from Elsevier.

This was followed by the work of Nag and Kutty [51,118] who presented evidence that B_2O_3 does not just act as an inert high temperature flux but that boron is incorporated in $SrAl_2O_4$:Eu^{2+},Dy^{3+} and plays an importantrole in the persistent luminescence mechanism. Based on infrared absorption measurements they were able to identify the presence of tetrahedral BO_4 groups in samples that were prepared with 5 at% of B_2O_3. Additionally, they performed solid-state ^{27}Al magical angle spinning nuclear magnetic resonance (MAS NMR) and noticed that the signal significantly changes upon addition of B_2O_3. Their results have been reproduced in Figure 7 from which it is evident that addition of B_2O_3 has two effects on the MAS NMR spectra. First, two new peaks arise at lower δ which can be attributed to Al in $Sr_4Al_{14}O_{25}$:Eu^{2+},Dy^{3+} which is formed as a minor impurity phase after addition of 20 mol% of B_2O_3. Secondly, the signal attributed to Al in $SrAl_2O_4$ considerably broadens towards higher δ which indicates an increased disorder in the Al surrounding upon B_2O_3 addition. Based on this information they concluded that the BO_4 groups substitute for AlO_4 groups. The incorporation of boron into the host is further evidenced by the observed decrease in unit cell volume of $SrAl_2O_4$:Eu^{2+},B^{3+} with respect to $SrAl_2O_4$:Eu^{2+} which agrees well with the smaller ionic radius of B^{3+} (0.25Å, 4-fold coordinated) [70] with respect to Al^{3+} (0.39 Å, 4-fold coordinated). [119,120]

Several authors noticed that adding large amounts of H_3BO_3 or B_2O_3, typically more than 10-15%, leads to the stabilization of the $Sr_4Al_{14}O_{25}$ phase and the creation of an amorphous strontium borate glass at the expense of the formation of the $SrAl_2O_4$ phase. [51,100,120,121] The formation of $Sr_4Al_{14}O_{25}$ can be understood when taking into account that boron substitutes for Al^{3+}, thereby effectively moving towards a more Al-rich phase in the phase diagram (Figure 3). Results by Niittykoski *et al.* [115] indicate that if the incorporation of boron on an Al site is accounted for in the initial stoichiometry, no $Sr_4Al_{14}O_{25}$ impurity phase is formed for boron concentrations up to 30 at%. This is in accordance with results by Shin *et al.* [122] confirming that an aluminium deficiency creates a driving force for boron incorporation in $SrAl_2O_4$.

The substitution of aluminum by boron also has an effect on the incorporation of Eu^{2+} and trivalent lanthanides in the host. Yoon *et al.* showed that samples prepared with B_2O_3 exhibit an increased resistance to thermal oxidation of Eu^{2+}. [120] In general, it is known that borates, most notably SrB_4O_7, successfully reduce trivalent dopants intrinsically [123–129], however the mecha-

nism is still under debate. [130] In $Sr_4Al_{14}O_{25}$ it was shown that boron improves the homogeneity of the Eu^{2+}-incorporation at the nanoscale. [88] It has also been reported that boron facilitates the incorporation of trivalent lanthanides on the alkaline earth sites because of its higher electronegativity with respect to aluminum which helps to stabilize the codopants on a Sr site, despite of the charge mismatch. [51, 122]

In general, codoping with boron [115, 120] is believed to have no effect on the spectral shape and position of the green emission of $SrAl_2O_4$:Eu^{2+} and a shift of the emission band to shorter wavelength with increasing boron content can be attributed to the formation of a europium doped $Sr_4Al_{14}O_{25}$ impurity phase of which the most prominent emission band is centered around 490 nm. [4] Delgado *et al.* [100] investigated the effect of boron incorporation on the luminescence of Dy^{3+} in $SrAl_2O_4$ and found that codoping with boron significantly changes the luminescence and absorption characteristics of Dy^{3+}. The magnitude of this effect, compared to the negligible effect of boron incorporation on the Eu^{2+} luminescence, can be understood by considering the aforementioned model by Nag and Kutty [51] who postulated that the more negative effective charge on the BO_4 group with respect to the AlO_4 group will lead to a preferential incorporation of Dy^{3+} on Sr sites where at least one of the closest Al^{3+} has been replaced by B^{3+}.

3.4 Synthesis

The properties of persistent phosphors are not only dependent on the composition of the phosphor but, as indicated in the previous section, also strongly depend on the synthesis conditions. Together with the growing number of potential applications, a wide range of synthesis techniques have been developed to improve the material's efficiency. In general a suitable synthesis should ensure a good incorporation of the dopants and yield phase-pure crystallites, preferably with a narrow particle size distribution. An efficient reduction of Eu is required to maximize the phosphor's efficiency by avoiding luminescence quenching due to intervalence charge transfer (IVCT) between Eu^{2+}-Eu^{3+} pairs [131] or an undesired excess of charge compensating defects. A range of chemical techniques exist to reduce trivalent lanthanide ions as recently reviewed by Suta and Wickleder. [132] It should also be stressed that transition metal impurities, typically originating even from high-purity precursor materials, can affect the trapping mechanism and should thus be carefully taken into account.

The presence of such impurities has been confirmed by an EPR study by Boutinaud *et al.* [68] and it has been suggested that small variations in the concentration of these impurities in precursor materials are responsible for the relatively poor reproducibility of the afterglow performance of $SrAl_2O_4$:Eu^{2+},Dy^{3+}.

Solid state synthesis methods are the most-reported preparation techniques. The ions in SrO, Al_2O_3 and rare earth oxides precursors interdiffuse during calcination at high temperature. The required high temperatures are usually achieved in a tube furnace by conductive and radiative heating. Hydrogen (H_2) or sometimes carbon monoxide (CO) gas is then added to the, respectively, nitrogen (N_2) or air atmosphere, as a reducing agent. This results in powders with good afterglow properties but has the drawback of not being energy-efficient and irregular grains with micrometer sizes are usually obtained. Alternatively, microwave-assisted solid state synthesis has been proposed as a more energy-efficient alternative to create micrometer-sized powders and results in phosphors with higher photoluminescence quantum efficiencies. [133–135] This implies the presence of fewer detrimental crystal defects compared to powders obtained via the conventional solid state synthesis. [134] Unfortunately, $SrAl_2O_4$:Eu^{2+} suffers from degradation when exposed to water with the luminescence intensity decreasing over time. [136] To counter this effect, post-synthesis, atomic layer deposition of a thin Al_2O_3 or TiO_2 coating has been applied to increase the moisture resistance of the phosphor as required for outdoor applications. [137]

For some applications such as medical imaging, nano-sized particles are required. [43–45, 138] Solution-based synthesis techniques such as combustion, [138–142] reverse micelle, [143] hydrothermal, [144] molten salt [145] and sol-gel [146] techniques have been developed and have proven to be useful to synthesize nanosized particles. Also laser synthesis techniques yield nanosized particles but the annealing at high temperature, required for the reduction of europium, results in the formation of larger micron-sized agglomerates. [147, 148] A decrease in particle size is however often detrimental for a phosphor's performance and both bottom-up [141] as well as top-down [149–151] synthesis techniques have resulted in inferior afterglow properties for $SrAl_2O_4$:Eu^{2+},Dy^{3+} nanocrystals compared to bulk. Recent results indicate that the decrease in intensity after intensive milling (top-down) is a consequence of the oxidation of Eu^{2+}. [151] Annealing the milled samples under a reducing atmosphere leads to partial regeneration of the photoluminescence intensity but does

not yield a full recovery of the afterglow intensities. Even though the shallow traps responsible for the afterglow seem to be affected by the milling, Kandpal *et al.* [149] reported an increase of the optically stimulated luminescence intensity for the milled samples. [151] Overall these results highlight the lack of knowledge concerning the chemical nature of the trapping defects, inhibiting the creation of efficient $SrAl_2O_4$:Eu^{2+},Dy^{3+} with dimensions in the nanometer range.

4 Phenomena related to trapping and energy storage

Until now the discussion has mainly focused on the spectral characteristics of $SrAl_2O_4$:Eu^{2+},Dy^{3+}. However, the existence of persistent luminescence in Eu^{2+} activated $SrAl_2O_4$ was known even several decades before Matsuzawa *et al.* [21] discovered the long afterglow performance of the codoped $SrAl_2O_4$:Eu^{2+},Dy^{3+},B^{3+}. Both Palilla *et al.* [73] and Abbruscato [152] prepared $SrAl_2O_4$:Eu^{2+} with an excess of aluminum and noticed that the samples exhibited low levels of persistence lasting up to a few seconds. As in all persistent phosphors, there is a multitude of luminescent phenomena related to the charge carrier trapping in these materials. The trapped charges can be released provided that enough energy is delivered to them and this energy can take the form of heat (afterglow or thermoluminescence, with the former actually being isothermal thermoluminescence), light (optically stimulated luminescence) or pressure (mechanoluminescence). The following paragraphs contain an overview of the luminescence properties of $SrAl_2O_4$ under application of these different stimuli.

4.1 Thermoluminescence

Thermoluminescence is an often-applied and seemingly simple technique to study the trap structure in luminescent materials. During these experiments the phosphor is first exposed to excitation light or ionizing radiation at a relatively low temperature. Next, the temperature of the phosphor is usually linearly increased while the intensity of the emitted light is recorded. The shape and height of the resulting glow curve depend on several experimental parameters such as the applied heating rate (β) and the excitation conditions (wavelength, intensity, illumination time and temperature) and on some sample-specific effective parameters such as the trap depth (ΔE_d) and the so-called frequency factor (s). [153] The results are often interpreted within the framework of a one-trapping/one-

recombination center model which provides an analytical prescription for the TL intensity as a function of temperature. [154] Materials in which the effect of retrapping can be neglected are said to follow first-order kinetics and their thermoluminescence glow peaks are well-described by the Randall-Wilkins equation [155, 156]

$$I(T) = n_0 \frac{s}{\beta} \exp\left(-\frac{\Delta E_d}{kT}\right) \times \exp\left(-\frac{s}{\beta}\int_{T_0}^{T} \exp\left[-\frac{\Delta E_d}{kT'}\right] \mathrm{d}T'\right) \tag{1}$$

The resulting TL glow peak is slightly asymmetric when using a constant heating rate and the temperature (T_m) at which the glow curve peaks, is independent of the dose (n_0) to which the phosphor was exposed. Garlick and Gibson [157] also explored the possibility that retrapping plays a dominant role in which case the phosphor is said to follow second-order kinetics. In turn May and Partridge [158] constructed an expression for so-called general-order kinetics for the cases in which the TL glow curve cannot be described by first or second-order kinetics. The expression is a purely mathematical prescription without any underlying physics and with an additional fitting parameter which is called the general-order parameter (b). This mathematical prescription reduces to the expression for first- and second-order kinetics upon choosing the correct value for b. However, in practice most materials exhibit first-order kinetics and if deviating behaviour is observed it can usually be attributed to the presence of multiple trapping defects, each with a specific trap depth or even a continuous trap depth distribution. Quite often the persistent luminescence and thermoluminescence of these materials can be adequately modelled using a set of discrete trap depths obeying first-order kinetics. [159–161] Additionally there is also a lack of physical grounds behind the use of higher-order kinetics to fit TL glow curves that result from an underlying trap distribution and hence this should be avoided. [162, 163]

Multiple measurement and analysis protocols have been developed over the years to extract trap depths and frequency factors of the corresponding traps in the material. [153, 164]. One approach is due to Hoogenstraaten [165, 166] who proposed the variable heating rate method which relies on the shift of the glow peak maximum to a higher temperature with increasing heating rates. For a trapping defect that is characterized by a specific trap depth ΔE_d and frequency factor s, one can derive the following expression from Equation 1:

$$\frac{\beta \Delta E_d}{kT_m^2} = s \exp\left(-\frac{\Delta E_d}{kT_m}\right) \tag{2}$$

If TL glow curves are recorded at different heating rates and a $\ln(\beta/kT_m^2)$ *vs.* $1/T_m$ plot is constructed it becomes possible to determine ΔE_d from the slope of the resulting curve.

Another accessible method to determine trap depths relies on the fact that at the low temperature side of the glow curve, during the initial rise, the temperature dependence of the TL intensity is mainly determined by the first exponential term in Equation 1, i.e.

$$I(T) \sim \exp\left(-\frac{\Delta E_d}{kT}\right) \tag{3}$$

The trap depth can easily be determined by constructing a $\ln(I)$ vs. $1/T$ plot and fitting a straight line to the linear part. [159, 167] As a rule of thumb only the part with an intensity lower than 10% of the maximum intensity is used.

As mentioned before, in most persistent phosphors the situation is more complex due to the presence of multiple, slightly different trapping centers resulting in a continuous trap depth distribution. The broad and highly overlapping glow curves are then difficult to analyse, especially since thermally stimulated detrapping can only be induced in a fixed order, going from shallow to deep traps. Nevertheless, also for this case, several measurement procedures have been developed to uncover the underlying trap depth distribution. [159, 167–170] Quite often these procedures consist of a combination of the initial rise or variable heating rate method with a stepwise thermal annealing or a gradual change in charging temperatures. When adopting the latter approach the effect of thermal barriers for trapping should be carefully considered. [163]

Spectrally resolved measurements are of special interest for phosphors such as $SrAl_2O_4$:Eu^{2+} that are characterized by multiple emissions, each with a different thermal behaviour (section 3.1) or to identify contributions from impurity phases such as $Sr_4Al_{14}O_{25}$:Eu,Dy. However, quite often the detection is achieved using photomultiplier tubes or photodiodes and only some rudimentary spectral information is obtained through the use of bandpass filters.

In general, thermoluminescence measurements are easy to perform but the quantitative analysis and accompanying extraction of trap depths and frequency factors (two highly-correlated parame-

ters) is less straightforward and is often performed with little regard to the underlying physics (see also Section 6). A notable example is the persistent (mis)use of computerized glow curve deconvolution software to extract trapping parameters by fitting a certain number of first- or general-order kinetics curves to a single broad and rather featureless glow curve. In contrast it would be good practice to simultaneously fit a mathematical model to a complete set of independent thermoluminescence, afterglow and fading measurements obtained under different conditions to obtain a consistent set of trapping parameters. [167]

TL in strontium aluminate phosphors

There are only a few reports dealing with deliberately non-codoped $SrAl_2O_4:Eu^{2+}$ and the reported thermoluminescence curves are displayed in Figure 8. A considerable part of the thermoluminescence intensity is located below room temperature which is in line with the short afterglow times for $SrAl_2O_4:Eu^{2+}$ at room temperature. [171] Although obscured by different heating rates, charging temperatures and dopant concentrations, some similarities can be identified by taking a closer look at Figure 8.

The main thermoluminescence peak of $SrAl_2O_4:Eu^{2+}$ is situated between 160 K and 230 K (Region II in Figure 8) and appears to have some substructure, the origin of which is not known. The thermoluminescence profile in Figure 8a has a prominent contribution at even lower temperatures, between 80 K and 140 K (Region I in Figure 8), which might be due to defects introduced by the excess SrO added during synthesis. [152] The same feature can be recognized in Figure 8d and the small shift in peak temperatures between the two curves can be explained by taking into account the difference in charging temperatures. [154] Finally at higher temperatures, between 240 K and 300 K (Region III in Figure 8), there is evidence of a contribution of slightly deeper traps. The thermoluminescence signal originating from these traps is most prominent in Figure 8e due to the comparably high charging temperature of 190 K that was employed. The lack of a notable signal above room temperature implies that the afterglow performance of the non-codoped $SrAl_2O_4:Eu^{2+}$ is not optimal, but the addition of codopants significantly changes the thermoluminescence curves.

A first considerable change of the thermoluminescence glow curves takes place upon the addition of boron. In Figure 9 a thermoluminescence curve of $SrAl_2O_4:Eu^{2+}$ (Figure 9f) is compared to those

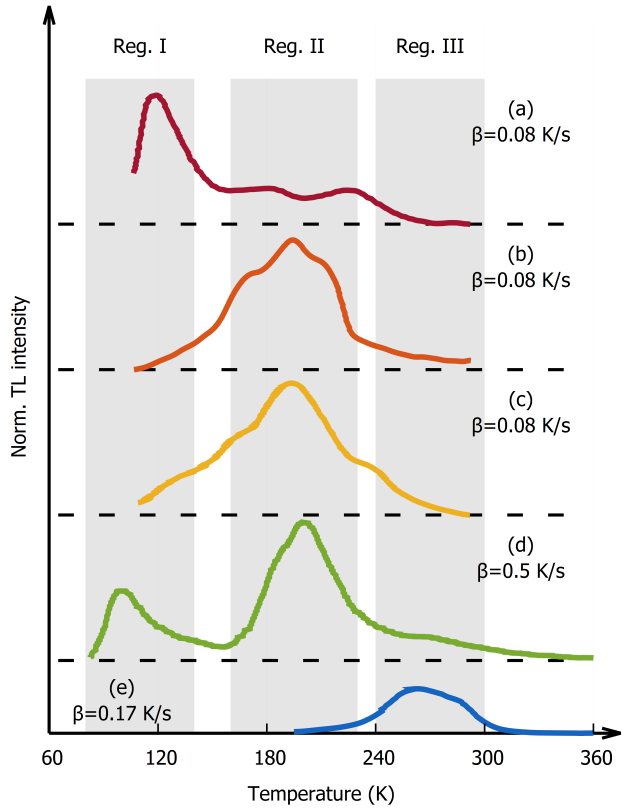

Figure 8: Thermoluminescence curves of $SrAl_2O_4$:Eu^{2+}. Curves (a-c) have been reproduced from Abbruscato, [152] curve (d) has been reproduced from Clabau *et al.* [172] and curve (e) has been reproduced from Yoon *et al.* [120]. The heating rate β is indicated for each curve. The lowest temperature at which the thermoluminescence is recorded is also the charging temperature. Full experimental details can be found in the cited references.

of $SrAl_2O_4$:Eu^{2+},B^{3+} (Figure 9a-e) but a straightforward interpretation is somewhat hindered by the large variations in heating rates used for these measurements. Firstly, it can be noted that the incorporation of boron in the material induces a small shift towards higher temperature in the peaks located in region II. Furthermore, the addition of boron significantly increases the intensity of the signal in region III. The most notable change is, however, the appearance of a thermoluminescence signal above room temperature between 340 K and 430 K (region IV in Figure 9). In general it appears that the addition of boron yields deeper traps, either through the modification of already existing shallow traps in $SrAl_2O_4$:Eu^{2+} or through the creation of new ones above room temperature. Additionally, Bierwagen *et al.* [173] observed that the incorporation of boron induces a broadening of the TL curves which is attributed to an increase in lattice disorder resulting in multiple inequivalent trapping centers.

The addition of dysprosium completely changes the thermoluminescence characteristics, as shown in Figure 10, and the result is a broad and featureless thermoluminescence peak centered around 310 K which is responsible for the material's bright afterglow. The shape of the thermoluminescence curves of $SrAl_2O_4$:Eu^{2+},Dy^{3+} remains unaffected by the addition of boron but as discussed in Section 3.3 the thermoluminescence intensity greatly benefits from the use of this flux. The thermoluminescence characteristics of $SrAl_2O_4$:Eu^{2+},Dy^{3+},B^{3+} have been extensively investigated during the past two decades. The shape and position of the thermoluminescence curve depend to some extent on the site on which Eu^{2+} is incorporated (Figure 10). Botterman *et al.* [59] and Hagemann *et al.* [177] independently found that excitation of the Eu_{Sr1} center with blue light ($\lambda_{ex} > 420$ nm) leads to the net filling of deeper traps with respect to excitation with UV light, which is effectively exciting Eu^{2+} on both Sr sites. More information about the wavelength dependency of the trap filling is contained in the thermoluminescence excitation spectrum shown in Figure 11. This spectrum represents the trap filling efficiency of each excitation wavelength and completely overlaps with the Eu^{2+} photoluminescence excitation spectrum, but nevertheless shows some distinct differences. Provided that the excitation intensity is kept constant over the complete wavelength interval (or if variations in intensity are corrected for) these subtle differences between the two types of excitation spectra can yield useful information on the optical properties of the trapping defects.

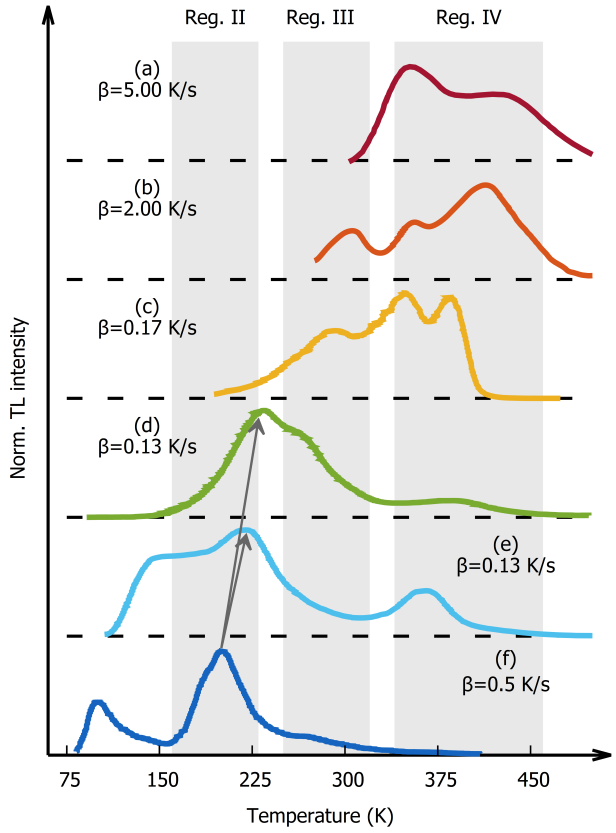

Figure 9: (a-e) Thermoluminescence curves of $SrAl_2O_4$:Eu^{2+},B^{3+}. Curve (a) has been reproduced from Aitasalo *et al.* [174], curve (b) has been reproduced from Matsuzawa *et al.* [21], curve (c) has been reproduced from Yoon *et al.* [120], curve (d) has been reproduced from Tsutai *et al.* [175], curve (e) has been reproduced from Kato *et al.* [176]. Curve (f) is used as a reference for a glow curve of $SrAl_2O_4$:Eu^{2+} and has been reproduced from Clabau *et al.* [172]. The lowest temperature at which the thermoluminescence is recorded is also the charging temperature. Full experimental details can be found in the cited references.

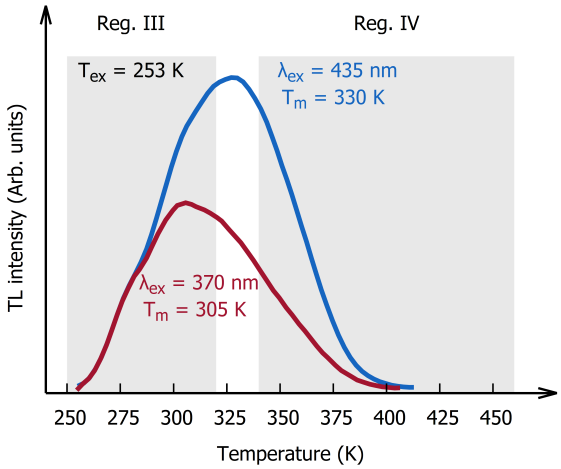

Figure 10: Thermoluminescence curves of $SrAl_2O_4$:Eu^{2+},Dy^{3+},B^{3+} excited by 370 and 435 nm light at 253 K and recorded at a heating rate of 0.2 K/s. The indicated regions are reproduced from Figures 8 and 9 to emphasize the different temperature scale. Reproduced with permission from Botterman *et al.*. [59] Copyright 2014 by the American Physical Society.

The broad thermoluminescence peak of $SrAl_2O_4$:Eu^{2+},Dy^{3+},B^{3+} can be modelled by a trap depth distribution extending from around 0.4 to 0.8 eV as substantiated by thermoluminescence measurements at different charging temperatures or after partial thermal cleaning. [59,174,177,178] This trap depth distribution ensures that the phosphor exhibits afterglow over a relatively large temperature range when compared to materials characterized by a single trap. This is especially important in view of some applications where the desired operating temperature range should be large. One example are luminescent road markings which should feature sufficient afterglow both during cold winter and hot summer nights. [22]

In addition to the well-studied thermoluminescence signals around and below room temperature there are also deeper, more stable traps in the material that give rise to a thermoluminescence signal above 600 K. [28,179–181] This thermoluminescence signal is largely affected by the thermal quenching of the emission that sets in at 440 K and has therefore hardly been studied. It was, however, recently shown that these traps, although thermally stable at room temperature, influence the filling rate of the shallow traps due to their high trapping cross section leading to a preferential filling. [182]

Recently, Bierwagen *et al.* [173] performed an extensive study of the effect of dopant concentrations, excitation wavelength and excitation temperature on the thermoluminescence properties

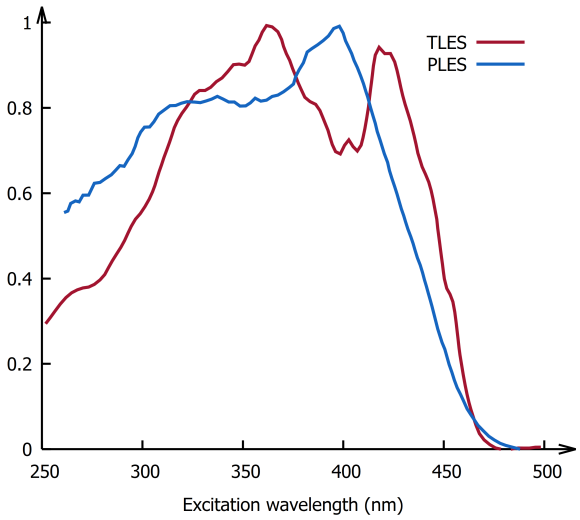

Figure 11: Thermoluminescence and photoluminescence excitation spectra of $SrAl_2O_4$:Eu^{2+},Dy^{3+},B^{3+}. The thermoluminescence excitation spectrum (TLES) is obtained by integration of the glow curves between 300 and 400 K. The photoluminescence excitation spectrum (PLES) is obtained by measuring the Eu^{2+} emission at 10 K. Reprinted from Bos *et al.* [153]) with permission from Elsevier.

above 200 K. Their results are largely in line with the overview presented here and further emphasize how difficult it is to compare thermoluminescence glow curves of $SrAl_2O_4$:Eu,(Dy,B) as their shape, peak position and intensity depend on many variables, which should all be taken into account.

4.2 Optically stimulated luminescence

Optical stimulation of the phosphor can provide an alternative to thermally stimulated detrapping and wavelength-dependent optically stimulated luminescence (OSL) measurements often deliver additional information about the optical fingerprint of the trapping defects. In these experiments, illumination of the charged phosphor with stimulation light provides the traps with additional energy and induces an additional and accelerated release of trapped charges. This manifests itself as an immediate increase in green luminescence which, like the afterglow, decays over time as the amount of trapped charges becomes depleted. In contrast to thermal stimulation, optical stimulation allows for a more selective emptying of traps provided that the different trapping defects have a specific spectral or optical response.

This optical stimulation is usually achieved using LEDs or lasers but if this stimulation of the

phosphor (usually with infrared light) is achieved using a grating spectrometer, a suitable longpass filter should be positioned between the monochromator and the sample to avoid unwanted re-excitation of the phosphor due to higher-order diffraction of UV or blue light. Moreover, when using lasers with high power densities for the stimulation it is possible that some local heating takes place. It is important to avoid or at least quantify this heating, as this will affect the shape of the OSL decay curve.

Optical stimulation is often limited to illumination with infrared light while there is no *a priori* reason to exclude higher energy light. One notable example is the finding that optically stimulated detrapping by UV and blue excitation light is responsible for the phosphor's limited storage capacity. [90] When moving towards higher energy stimulation light the overlap with the activator's excitation spectrum or the phosphors trap filling spectrum cannot always be avoided and extensive modelling is often required to distinguish between all the different luminescence processes taking place simultaneously. [90, 183]

OSL in strontium aluminate phosphors

For $SrAl_2O_4$:Eu^{2+},Dy^{3+} it has been shown that OSL can be induced using infrared light covering a broad wavelength range from 800 nm to 980 nm. [28,178,181,184] However, Jia *et al.* [185] expanded the OSL measurements from the more conventional infrared wavelengths to visible and ultraviolet wavelengths. This task is obviously complicated by the fact that this wavelength range overlaps with the excitation spectrum of the Eu^{2+} and hence with the thermoluminescence excitation spectrum (see Figure 11). [153] They performed pulsed OSL measurements and investigated the transients of the green Eu^{2+} luminescence after a short pulse with 355 nm light. The luminescence decay of the phosphor is shown in Figure 12 upon constant UV illumination, compared to the same experiment without UV illumination. The latter consists of a slow decay with a characteristic time of several hundred nanoseconds, which is in the typical range of Eu^{2+} decay times, as discussed in Section 3.1. However an additional fast component with a decay time of $\approx$ 100 ns is found if the phosphor is exposed to UV radiation during the experiment. These results were confirmed by Pellé *et al.* [186] and in both works the fast component was tentatively ascribed to an OSL process induced by the UV light. This interpretation agrees well with the finding by Botterman *et*

al. [59] that the contribution of this short decay to the total intensity exhibits a similar temperature dependence as the trap filling. The large difference in decay times for the photoluminescence and OSL processes are explained by Jia *et al.* by considering that the presence of a local trap induces additional non-radiative pathways. [185]

The idea of OSL induced by excitation light regained attention lately as it has been suggested by Hagemann *et al.* [177] to explain the wavelength and temperature dependency of the steady state luminescence intensities of $SrAl_2O_4$:Eu^{2+},Dy^{3+},B^{3+}. Van der Heggen *et al.* [90] also found that the internal quantum efficiency of $SrAl_2O_4$:Eu^{2+},Dy^{3+},B^{3+} is strongly intensity-dependent, dropping from 71% to 54% with increasing excitation intensity. This was linked to a remarkably high absorption cross-section of the filled traps which was found to be $(2.16 \pm 0.36) \times 10^{-17}$ cm^2 and $(1.22 \pm 0.17) \times 10^{-17}$ cm^2 at 375 nm and 445 nm, respectively. This absorption of the filled traps in the UV or blue introduces an additional optical detrapping mechanism during the charging of the phosphor and actively limits the storage capacity of $SrAl_2O_4$:Eu^{2+},Dy^{3+}. Moreover, this effect has a large impact on the phosphor's performance because the absorption cross-section of the filled traps is considerably higher than that of Eu^{2+}, which was found to be 3.60×10^{-18} cm^2 and 4.4×10^{-19} cm^2 by Van der Heggen *et al.* [90] and 9.8×10^{-19} cm^2 and 1.3×10^{-19} cm^2 by Delgado *et al.* [89], for 375 and 445 nm, respectively. Despite the factor of three difference between these values, which illustrates the difficulty to measure these quantities accurately, it shows that optically stimulated detrapping can play a major and competitive role during charging.

Optical stimulation of the phosphor does not exclusively lead to emptying of traps but can also be used to induce a redistribution of trap occupation, a process that is sometimes referred to as photo-transfered thermoluminescence. Such an optically induced redistribution has already been identified in chromium doped lithium and zinc gallates [187,188] and yttrium aluminum gallium garnets [189] and also in $SrAl_2O_4$:Eu^{2+},Dy^{3+}, but only under green illumination. [182] This phenomenon could potentially be used to increase the luminescence output of persistent phosphors by transferring charges from deep traps to more shallow, thermally accessible traps.

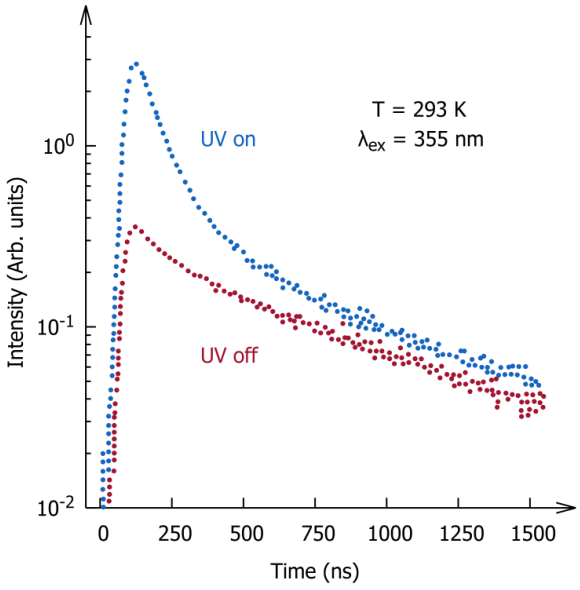

Figure 12: Photoluminescence decay of $SrAl_2O_4$:Eu^{2+},Dy^{3+} monitored at 520 nm and measured under 355 nm pulsed excitation with and without continuous illumination by a 4W UV lamp. Reprinted from Jia *et al.* [185]) with permission from Elsevier.

4.3 Mechanoluminescence

Mechanoluminescence (ML) refers to light emission from solids upon any kind of mechanical stimulus. [190–195] The phosphors are usually embedded in transparent binders, such as resins or glasses to facilitate stress transfer to the phosphor microparticles. While it is known that external stress can generate charge carriers at the surface of the binder or at the binder-phosphor interfaces which can ultimately result in luminescence, [196–198] in the following we will only focus on recoverable mechanoluminescence upon elastic deformation (sometimes called elasticoluminescence), a process that is directly related to the charge trapping in some persistent phosphors. [192,199] This process is quite similar to TL or OSL as the application of a mechanical stimulus can induce detrapping which leads to luminescence but only when the phosphor is exposed to excitation light first. Due to its unique nature, ML can serve as a probe to reveal the subtle interactions among traps, luminescent centers, and the host crystal of the ML phosphor.

ML in strontium aluminate phosphors

In 1999, Xu *et al.* [200] found that $SrAl_2O_4$:Eu^{2+} shows strong ML upon application of a linear compressive stress profile. [200, 201] It was later found that monoclinic $SrAl_2O_4$ is the only phase in the Al_2O_3-SrO phase diagram that demonstrates ML upon doping with Eu^{2+}. [202] It was also observed that the ML intensity is proportional to the magnitude of the effective stress during loading. The ML emission spectrum is the same as that of photoluminescence spectrum implying that Eu^{2+} is the emitting center. The temporal resolution, which is limited by the photoluminescence decay time of Eu^{2+}, can reach the sub-millisecond regime according to several time-resolved experiments. [203–205] Apart from Eu^{2+}, Ce^{3+} ions can induce ultraviolet ML in monoclinic $SrAl_2O_4$, and the sensitivity can be quadrupled by co-doping with Ho^{3+}. [206] Infrared ML can be achieved in $SrAl_2O_4$:Eu^{2+} by co-doping with Er^{3+} [207] or Nd^{3+} [208] ions.

The sensitivity of $SrAl_2O_4$:Eu^{2+} is evidently dependent on the properties of the traps that are responsible for ML. Hence, synthesis procedures can, in principle, be carefully designed to tailor the desired properties. Tu *et al.* [209] reported that H_3BO_3, which is often used as a flux in $SrAl_2O_4$:Eu^{2+} preparation (Section 3.3), can almost triple the sensitivity by increasing the trap density and altering the trap depth distribution. The codopant Dy^{3+} also leads to a higher sensitivity and a higher saturation threshold. [37] Co-doping with Zr^{4+} was found to increase the sensitivity of $SrAl_2O_4$:Eu^{2+} in the small strain range ($\sim 10^{-4}$). [210, 211] Zhan *et al.* [212] found that swift heavy ion irradiation enhances the persistent luminescence and ML by increasing the trap density. [212, 213] At the device level, the sensitivity of a ML sensor can be improved by optimizing the load transfer from the binder to ML particles. This can be achieved by utilizing stiffer binders [214, 215] or by enhancing the bonding at the binder-phosphor particle interfaces. [216, 217]

The ML intensity under a given stress profile is presumably linked to the kinetics of trapped electrons that are also responsible for persistent luminescence, thermoluminescence or optically stimulated luminescence. A linearly increasing stress (i.e., a ramp) or a sinusoidal stress is often applied to reveal the characteristics of the ML intensity. Xu *et al.* [201] identified a linear relationship between ML intensity and stress during a ramp. Kim *et al.* [218] confirmed this relation but showed that only the effective stress (namely von Mises stress) contributes to ML, while Dubernet *et al.* [219] argues that hydrostatic stress also causes ML from $SrAl_2O_4$:Eu^{2+} particles embedded

in a glass matrix. In contrast, Rahimi *et al.* [220] found a quadratic relationship between ML intensity and stress. Recently, Azad *et al.* [221] demonstrated the possibility to visualize full-field strain by ML intensity (as illustrated in Figure 13(a)). Once again, they observed a quadratic relationship between the ML intensity and the effective strain for ramps with various loading rates (Figure 13(b)). [221] These findings indicate a nonlinear nature of ML intensity as a response to stress profiles. To clearly observe this feature, it is beneficial to adopt a constant stress profile after the ramp reaches its maximum. Under such a stress profile, the ML intensity was found to decay with time yet at a rate which is faster than that of the stress-free persistent luminescence under same charging conditions. [215, 219, 220, 222, 223] This decaying trend of ML under constant load has been detected in ML phosphors other than $SrAl_2O_4$:Eu^{2+} as well, such as (Ba,Ca)TiO_3:Pr^{3+}, [224] $BaSi_2O_2N_2$:Eu^{2+}, [225] (Ca,Sr)$Al_2Si_2O_8$:Eu^{2+},Pr^{3+}, etc. [226] Furthermore, for a repetitive triangular stress profile, the ML intensity at the maximum stress decreases with increasing cycling number N but can restore to the initial value ($N = 1$) after sufficient optical charging. [227] The implication from these findings is at least two-fold. The ML intensity seems to be a nonlinear function of the stress profile and it depends on the stress history as well. This poses intrinsic difficulties to infer stress/strain from the measured ML intensity. Moreover, the ML intensity is obviously related to the same trapping and detrapping processes as the persistent luminescence.

The nonlinear behavior is directly associated with the detrapping process. This is illustrated by the ML intensity resulting from a sinusoidal stress which follows a decaying trend and a sinusoidal response with decreasing magnitude (Figure 14(a), for frequency $f = 1$ Hz). [228] The magnitude of the Fourier transform of the ML intensity exhibits higher-order harmonics (Figure 14(b)). A slight phase lag and hence a hysteresis were found between the ML intensity and the stress input, suggesting a non-instantaneous input-output relation. This reveals the intrinsic feature of the kinetics of trapped electrons since no phase lag was found for the stress-strain curve of the sensor. Using strong UV charging during loading, Sohn *et al.* [229] managed to remove the decaying trend and the decay of the magnitude of the harmonics in the ML intensity. The phase lag disappeared and the ML intensity was then proportional to the maximum stress for a trapezoid stress profile. It is therefore plausible that the stress empties the same pool of trapped electrons, and the subsequent recombination at the luminescent centers produces ML. Hence, a constant ML response magnitudes

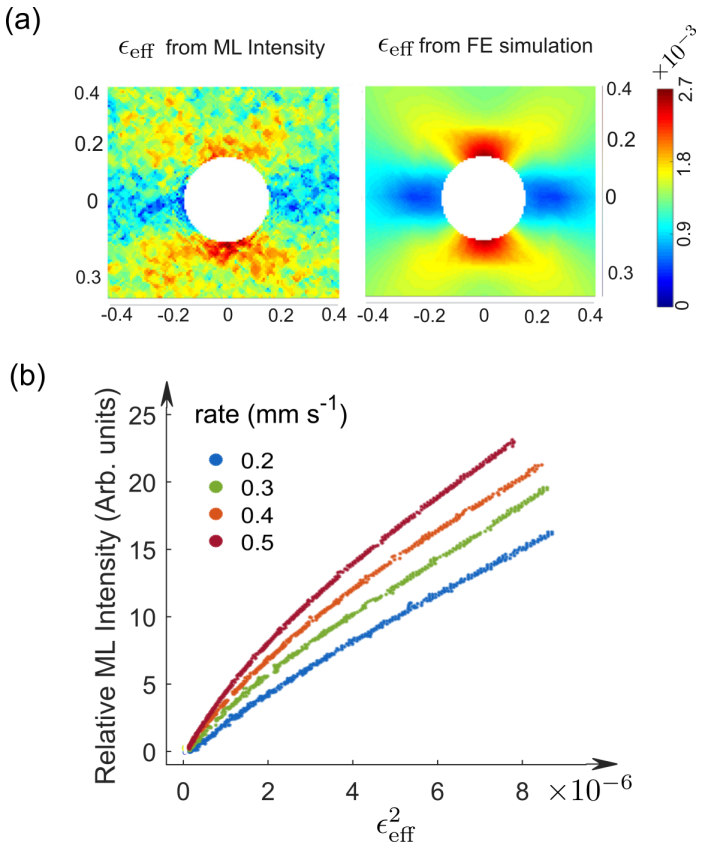

Figure 13: ML intensity under a ramp load. (a) For a ML intensity map corresponding to loading level of 5350 N during a ramp, the effective strain ϵ_{eff}^2 estimated from the ML image agrees with the one obtained from finite element (FE) simulation. (b) The instantaneous ML intensity is proportional to effective strain square ϵ_{eff}^2 during ramps with various load rates. Reproduced from Azad *et al.* [221] with permission.

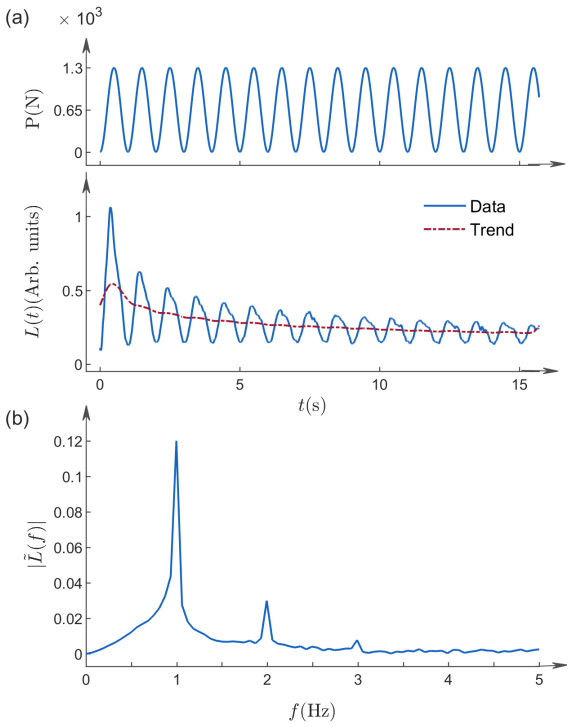

Figure 14: ML intensity under a sinusoid stress. (a) Under a sinusoid stress (1 Hz, top panel), the ML intensity (bottom panel) is characterized by a decaying trend (depicted as dotted line) and oscillations with decaying magnitudes. (b) The Fourier transform spectrum shows high-order harmonics. Reproduced from Sohn*et al.* [228] with permission.

can be expected when the density of trapped electrons remains constant because of strong charging. One obvious drawback of this approach is the small signal-to-background ratio as the photoluminescence intensity is much stronger than that of ML. It is noteworthy that this approach is of great interest to investigate intrinsic ML responsivity of phosphors.

Several luminescence mechanisms, accompanied by mathematical models, have been proposed to account for ML intensity as a response to stress loading. Unfortunately, a convincing quantitative model, capable of explaining and predicting all the ML features, is still lacking. Initially, Xu *et al.* [230, 231] proposed that ML originates from the recombination between holes and electrons which are detrapped due to internal electric fields upon deformation. They found large spontaneous strains [230] and also twin-boundaries [231] in $SrAl_2O_4$:Eu^{2+} and argued that these structural features favor (local) piezoelectricity. Similarly an increase in dislocation density appears to favour the ML intensity at the expense of the stress-free afterglow. [232] This suggests a close connection between the occurrence of efficient ML and the non-centrosymmetric (i.e. piezoelectric) symmetry of the crystalline host. For example, Hara *et al.* [233] recently found a positive correlation between ML intensity and the piezoelectricity coefficient in the $Li_{1-x}Na_xNbO_3$:Pr^{3+} phosphor. With this in mind it is interesting to note that of all the phases in the SrO-Al_2O_3 phase diagram, only the monoclinic $SrAl_2O_4$ is non-centrosymmetric and as stated before, the other phases do not exhibit efficient ML. Chandra *et al.* [234, 235] proposed that piezoelectricity facilitates detrapping by reducing the trap depth and that ML intensity should be proportional to the mechanical power (i.e. the product of stress and stress rate). This model fails to predict a decaying ML intensity under a constant stress. Dubernet *et al.* [223] modeled the luminescence output by first-order detrapping kinetics with a time-dependent rate coefficient. Aiming to account for mechanical detrapping, this rate coefficient was modeled as the convolution between the absolute mechanical power (i.e. the product of stress and stress rate). and a stretched exponential creep function. The parameters of this model were fit to an initial loading experiment. Subsequently, the model was able the predict the ML response under a more complicated stress profile, including a plateau of constant stress. Under the same theoretical framework, Dubernet *et al.* [219] found that another creep function, borrowed from the Zener model for viscoelasticity, can account for ML intensity under their loading conditions as well. Kim *et al.* [236] simulated the ML from a set of differential equations for electron kinetics among

traps and luminescent centers, assuming that the detrapping rate coefficient was proportional to the stress rate. This model predicts a quadratic-like, non-linear function of the ML intensity under a ramp but no prediction of ML response under constant stress was given.

Key ingredients are still missing in these models. Firstly, the model should fully account for the persistent luminescence decay profile under stress-free conditions. This requires a correct treatment of the detrapping kinetics, which could be within a local or global model (Section 5.3), and of the trap depth distributions as well. Secondly, the role of mechanical detrapping remains vague. It is debatable whether it increases the detrapping rate coefficient or reduces the trap depth. In any case it is important to verify that no other mechanisms are wrongly interpreted as ML. One notable example is the recent discovery that the light emitted by a persistent phosphor under exposure to an ultrasound beam is in fact not due to mechanical stimulation as was first conjectured, [212] but is essentially due to local ultrasonic heating and is hence a special form of thermoluminescence. [160]

5 Identifying the requirements for a correct model from experiments

Over the past twenty years several models have been proposed to explain the persistent luminescence and the related phenomena in various compounds. The most popular models are due to Matsuzawa *et al.* [21], Aitasalo *et al.* [237, 238], Dorenbos [239] and Clabau *et al.* [87]. These models differ in many ways but the most important differences concern the type of charge carrier involved in the trapping (holes or electrons), the nature of the trapping (local or global) and the chemical nature of the traps (intrinsic or extrinsic defects). We will not describe these models in detail as this has already been done by e.g. Van den Eeckhout *et al.* [16] or Vitola *et al.* [60] but we will rather try to identify the requirements to which a model describing the afterglow process in $SrAl_2O_4$:Eu^{2+},Dy^{3+},B^{3+} should adhere. In Section 6 the theoretical considerations behind the different models found in literature will be discussed in detail.

5.1 The role of europium

The first thing to consider is the wavelength-dependence of the trapping process. Several persistent and thermoluminescence excitation spectra [29,177,179,240] have been measured (see e.g. Figure 11) and it was found that these excitation spectra closely match the photoluminescence excitation spectrum of Eu^{2+} in $SrAl_2O_4$, irrespective of the codopants and irrespective of the crystallographic site on which the activator is incorporated. The small difference between the onset of the persistent luminescence and the photoluminescence excitation spectrum described by some authors is sometimes attributed to the inability of light of longer wavelengths to induce photoionization of the Eu^{2+} but it should be considered that this discrepancy might simply be the result of the limited sensitivity of the detection systems that were used to measure the afterglow or thermoluminescence. Additionally, also a thermal barrier for trapping might introduce a temperature and wavelength dependent behaviour. [163] A detailed study on the wavelength and temperature dependence of the trap filling by Hagemann *et al.* [177] and Botterman *et al.* [59] showed that trapping is to a large extent thermally activated. [171] The size of this effect depends, however, on which site Eu^{2+} is incorporated: excitation with wavelengths higher than 420 nm, exclusively exciting Eu_{Sr2}, only induces trapping above 170 K whereas excitation with wavelengths lower than 420 nm, exciting both Eu_{Sr1} and Eu_{Sr2}, induces trapping at lower temperatures as well.

EPR measurements further indicate that the concentration of Eu^{2+} decreases upon UV exposure and increases again when the excitation is stopped. [87] Similar results were also found in SrS:Eu. [241] We therefore conclude that excitation of Eu^{2+}, incorporated on either of the two crystallographic sites, is necessary to induce trapping in case light with sub-bandgap energy is used. Models such as the one by Aitasalo *et al.* [237] that conjecture an energy transfer from trapping defects (other than Eu^{2+}) to Eu^{2+} are unable to explain the similarity between persistent luminescence and photoluminescence excitation spectra.

The situation is different upon exposure to ionizing radiation (with an energy larger than the band gap energy E_G), directly producing electron-hole pairs, removing the need of direct Eu^{2+} excitation. In this case, more possibilities for energy storage are generated compared to the direct excitation of Eu^{2+}. However, X-ray Absorption Near Edge Structure (XANES) experiments indicate that also upon X-ray excitation, Eu^{2+} will act as a hole trap and subsequently as a recombination

center. [242, 243]

5.2 Electron or hole trapping?

There is a general consensus that the trapping process is accompanied by the release or uptake of an electron by the luminescence activator, which undergoes oxidation or reduction. From the viewpoint of the transferred charge carrier, this is termed electron or hole trapping, respectively. In the case at hand, Eu^{2+} is the activator, so electron (hole) trapping would correspond to the formation of a metastable Eu^{3+} (Eu^{+}) center, respectively.

Abbruscato [152] performed Hall-effect measurements and suggested that excitation of Eu^{2+} is followed by the delocalization of a hole which is then successively trapped at a defect. Matsuzawa *et al.* [21] added more experimental indications to this theory using photoconductivity measurements under non-uniform illumination. These two independent measurements constitute the only evidence in favor of a trapping mechanism based on the transfer of holes. However, a model based on hole trapping would imply the formation of Eu^{+} when the phosphor is exposed to UV light and both Clabau *et al.* [87, 172] and Dorenbos [239] correctly noted that the resulting valence states of the dopants after hole trapping (i.e. Eu^{+} and Dy^{4+}, assuming that Dy^{3+} is the redox partner of Eu^{2+}) are chemically unstable. Following this reasoning, the hole trapping model quickly lost its initial popularity in favor of an electron trapping model (see Figure 2(a)). Later on, XANES measurements indeed indicated that no Eu^{+} is formed under X-ray exposure but confirmed that Eu^{2+} is oxidized to Eu^{3+}. [242, 243]

This implies that the effect observed during the photoconductivity experiments by Matsuzawa *et al.* [21] and the Hall-effect measurements by Abbruscato [152] are of a different physical origin. The results by Matsuzawa *et al.* [21] are reproduced in Figure 15 and it is clear that the photoconductivity signal gradually increases with temperature and no abrupt characteristics related to thermoluminescence peaks are observed. [21] Quite the contrary, the signal levels off when room temperature is reached, i.e. when the afterglow gets stronger. The thermal quenching profile of the blue Eu^{2+} emission, which is reproduced in Figure 15 as well, does however exhibit a similar temperature dependency as the photoconductivity. This suggests that the photoconductivity signal measured by Matsuzawa *et al.* might be related to the thermal quenching of the blue emission

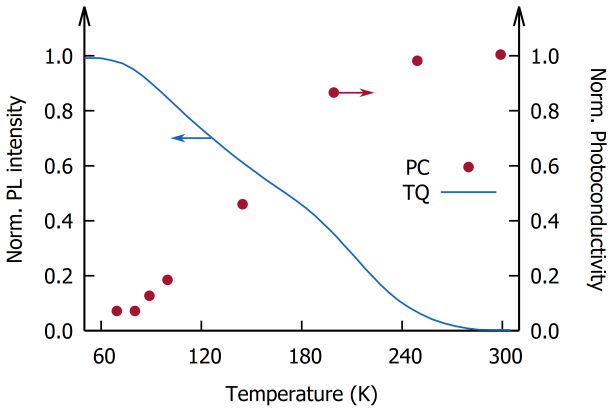

Figure 15: Thermal quenching (TQ) of the blue emission band under 370 nm excitation (data reproduced from Botterman *et al.* [59]) and the temperature dependence of the photoconductivity (PC) under continuous UV illumination (data reproduced from Matsuzawa *et al.* [21]).

from the Eu_{Sr1} center. The slowly decaying photoconductivity signal after excitation has stopped, can then be attributed to the population and simultaneous quenching of the excited states of the Eu_{Sr1} center following detrapping. This interpretation is in line with the results from a detailed wavelength and temperature dependent investigation of the photoconductivity by Ueda *et al.* [75] and indicates that trapping and detrapping in $SrAl_2O_4$:Eu^{2+},Dy^{3+} can to some extent be regarded independently from photoconductivity and thermal quenching of Eu^{2+}.

5.3 Local or global model?

The question remains whether the charge transfer from Eu^{2+} to the trapping defect and back happens via a localized transition or whether an intermediate electron delocalization, i.e. the involvement of the conduction band of the host, is required. In the former case, sometimes called the local model, the activator and trap have to be in close proximity because there is a distance-dependency in trapping and detrapping probability. In the latter case, called the global model, the electron can freely move through the conduction band to a remote trapping defect with a vanishing distance-dependency (see Section 6.1.2). The main argument in favor of the so-called global model is the existence of photoconductivity during the afterglow of the phosphor. As explained above, however, it seems that both phenomena do not necessarily share a common origin. The most important argument in favor of a global model is hence not supported by experiment.

The finding that excitation of Eu_{Sr1} or Eu_{Sr2} leads to the filling of different traps (see Figure 10) favors a local model because in a global model all trapping defects are shared between both types of Eu^{2+} centers. It should however be stressed that some caution should be exercised when interpreting the results in Figure 10, as optically stimulated detrapping by excitation light might also contribute to the wavelength dependence of the thermoluminescence signal. More arguments in favor of a local model have been proposed. Charging curves have, for example, been succesfully fitted with a mathematical prescription that is derived from a local model [183, 244] and a small time-dependent redshift in the afterglow spectrum has been reported that can be attributed to a correlation between the local crystal field of Eu^{2+} and the trap depth, suggesting the presence of the trapping defect in close proximity to the Eu^{2+} ion. [87][1]

Despite the above arguments, no direct and unambiguous measurements of the interaction range between activators and traps exist, illustrating the difficulty to access this information experimentally.

Ab initio theoretical methods carry the potential to help answering this issue even if the computational challenges are enormous. Some first steps towards the understanding of trapping phenomena have recently been taken by *ab initio* multiconfigurational calculations on the structurally more symmetric cases of CaF_2:Eu^{2+},Ln^{3+}. [246, 247] Systematic calculations of metal-to-metal charge transfer states (MMCT) involving Eu^{2+} as electron donor and the trivalent lanthanide codopant as electron acceptor revealed that trapping can be expected for Eu^{2+}, Sm^{3+}pairs in this host. [246] Interestingly, no intermediate electronic state is required and the initial (Eu^{2+}-Sm^{3+}) and final (Eu^{3+}-Sm^{2+}) states are bridged directly. Moreover, it was shown that the energy cost to further excite the $5d$ electron to the conduction band amounted to 7.60 eV, which is too high for photoionization. [247] These calculations were able to explain all experiments related to trapping and detrapping in this model system. Furthermore, the picture that emerges from it is simpler than the conventional picture involving the conduction band as less steps are required during trapping and detrapping. It remains an open question to what extent these conclusions can be transferred to conventional persistent phosphors such as the aluminates discussed here.

[1] In contrast, a blueshift of up to 10 nm has been reported by Hölsä *et al.* [245] in $CaAl_2O_4$:Eu,Dy but it seems that this was the result of a slow scanning speed during the recording of the afterglow spectrum without correction for the decaying afterglow intensity as more recent reports do not mention the existence of such a shift. [174, 237, 238]

5.4 Nature of the trapping defects

It has been shown by combined X-ray spectroscopy and radioluminescence spectroscopy that Dy^{3+} is reduced to Dy^{2+} during the charging of persistent luminescent aluminates, [243]

$$Eu^{2+} + Dy^{3+} \underset{\text{IR}}{\overset{\text{violet, X-rays}}{\rightleftharpoons}} Eu^{3+} + Dy^{2+}. \quad (4)$$

As discussed slightly further in this section, this confirms the often conjectured, direct involvement of the trivalent lanthanide dopant in the trapping process. However, this does not completely resolve the puzzle as a remarkable persistent luminescence is also found in non-codoped $SrAl_2O_4$:Eu^{2+} when prepared under the correct conditions, [73,120,152] suggesting the involvement of native defects in trapping. The most important requirement for a defect to qualify as a trap is that it can adopt at least two charge states, i.e. that it can undergo a (photo)redox reaction with the Eu^{2+} activator. In the following, some insightful works on the nature of the trapping defects are elaborated.

Intrinsic and charge-compensating defects

Many reports on the chemical nature of the traps are based on charge-compensation arguments concerning the trivalent codopants or on conclusions drawn from slight variations in afterglow performances upon deviation from the ideal 1:2:4 stoichiometry in $SrAl_2O_4$. Although the reasoning behind these arguments seems plausible, it is known that synthesis-property relations in this class of luminescent materials exhibiting trapping suffer from a poor reproducibility, making these findings inaccurate. More direct evidence on the nature of the traps is unfortunately mostly lacking.

A promising technique to tackle the identification of these intrinsic electron trapping defects is EPR spectroscopy. Hölsa *et al.* [248] performed EPR measurements on undoped and europium doped $CaAl_2O_4$ and found evidence for electron trapping, supposedly by anion vacancies. Takeyama *et al.* [249] performed similar measurements on undoped and dysprosium doped $SrAl_2O_4$ in combination with *in situ* illumination with UV light. They found three different paramagnetic defect centers in $SrAl_2O_4$: an anistropic hole trapping center ($g = 2.007$), an electron trapping center ($g = 1.999$) and, based on the hyperfine splitting of the third signal, a hole trapped on $[AlO_4]^-$

($g = 2.0075$). Slight variations in stoichiometry of undoped $SrAl_2O_4$ indicate that the electron trapping defect is an oxygen vacancy while the hole trap is a Sr-vacancy. These two signals exhibit a transient behavior in $SrAl_2O_4$:Dy^{3+} lasting up to several hours after illumination with UV light has stopped, indicating that these defects might be involved in the afterglow process. In addition, changes in decay times of the EPR signals upon Dy^{3+} addition suggest that the codopant is needed to stabilize the trapped charges. Unfortunately, no time profiles of the persistent luminescence were provided to allow for a one-on-one comparison of the decay kinetics.

Thermoluminescence measurements on $SrAl_2O_4$:Eu^{2+} by Bierwagen *et al.* [173] suggest that boron stabilizes additional F-centers and leads to the creation of deep oxygen related trapping centers. Furthermore they found that the $^5D_0$-$^7F_1$ emission band of Eu^{3+} is strongly inhomogeneously broadened, suggesting that charge-compensating defects are most probably in the first coordination sphere of Eu^{3+}. Based on classical (i.e. non-quantum), semi-empirical Mott-Littleton calculations of dos Santos *et al.* [250] it was postulated that this charge compensating defect corresponds to an oxygen interstitial in one of the voids in the structure of $SrAl_2O_4$. [251]

Density functional theory (DFT) calculations on defective supercells, subject to periodic boundary conditions, are increasingly popular to describe native, charge-compensating or substitutional defects. [107, 131, 252–254] Due to the nature of DFT, its scope is limited to (single-reference) ground-state properties such as equilibrium geometries, elastic constants, vibrational modes, but also defect formation enthalpies and hence charge-state transition levels. [255] This technique was recently applied to obtain charge-state transition levels of a selection of native point defects in $SrAl_2O_4$ and $Sr_4Al_{14}O_{25}$:Eu^{2+},Dy^{3+} crystals. [256, 257]

Finley *et al.* [256] focused on isolated anion and cation vacancies in $SrAl_2O_4$ and they pointed out that oxygen vacancies induce charge-state transition levels in the range of 0.5-0.6 eV below the conduction band, which agrees with typical trap depths extracted from thermoluminescence experiments. For both aluminate hosts, it was established that oxygen vacancies form negative-U defects, meaning that electrons will be trapped and released in pairs, indicating that one vacancy can, and must, accommodate the electrons of two Eu^{2+} donors. [258] Interestingly, these calculations indicate that a rich variety of native defects, covering different chemical natures, but also multiple non-equivalent crystallographic sites, give rise to charge-state transition levels in the band gap and

hence are potential traps. This conclusion can be generalized to virtually any crystal, especially featuring a low symmetry, indicating that there is more to a suitable host for persistent luminescence than one or several point defects with their charge-state transition levels at a suitable depth with respect to the valence or conduction bands. Additionally, it should be remarked that a discrete trap depth energy, as obtained from this type of DFT calculations is hard to compare to experimental observables such as afterglow or TL profiles. A significant parameter correlation exists between trap depth energies (ΔE_{tr}) and frequency factors (s) in curve fitting (see Equation 1), obscuring the meaning of their exact values. Calculating frequency factors from DFT is less straightforward, it is even not clear whether single-barrier-model-derived expressions are suitable to achieve a microscopic understanding of temperature-dependent processes. Nonetheless, promising results have been recently achieved in understanding non-radiative dynamics by detailed vibrational analysis of DFT calculations. [259, 260]

Apart from isolated point defects such as V_{O}, V_{Sr}, Sr_i, which are the obvious suspects, extrinsic defects and defect clusters related to the boron flux have been proposed as trap as well. [51, 118] In addition to these, other extrinsic defects can be incorporated during the high-temperature synthesis. Particularly, hydrogen (H) is a notorious impurity in semiconductor physics where its amphoteric character is known to strongly impact charge carrier dynamics. [261,262] In many cases H_2 gas is used as reducing agent during solid state synthesis (see Section 3.4), making it plausible that H impurities are incorporated, presumably interstitially (H_i) as in the case of the well-studied semiconductors. [261,262] The difficulty to identify H with standard structural and analytical techniques makes this a hitherto overlooked possibility.

Ln^{3+} codopant

The direct involvement of trivalent lanthanides in the electron trapping mechanism of several Eu^{2+} doped phosphors had already been suggested by Matsuzawa *et al.*. [21] Initial attempts to prove this using X-ray absorption techniques provided no convincing evidence for valence changes of the trivalent codopants [104,242,263–265] which incorrectly led to the suggestion that electron trapping either takes place on intrinsic defects or via the creation of $Ln^{3+} + e^-$ pairs. These hypothetical states are reminiscent of impurity trapped exciton (ITE) states, originally hypothesized by McClure

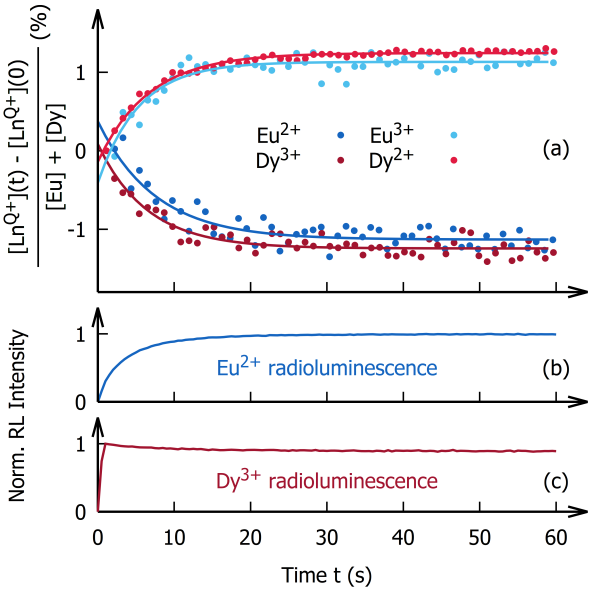

Figure 16: Time evolution of the lanthanide oxidation states, relative to the total [Eu]+[Dy] content from high energy resolution fluorescence detected X-ray absorption near edge structure (HERFD-XANES) on $Sr_4Al_{14}O_{25}$:Eu^{2+},Dy^{3+} (a). The X-ray beam is switched on at time $t = 0$. Simultaneously, the luminescence intensity is probed for Eu^{2+} (broadband emission in 450–550 nm range) (b) and Dy^{3+} (line emission in 550–600 nm range). Reproduced from Joos *et al.* [243] with permission.

and Pedrini in a different context [266], i.e. excited states of Ln^{2+} ions where one valence electron occupies a more diffuse orbital, leading to a shorter equilibrium bond length, comparable to the Ln^{3+} species. [267] ITE's have been studied for several lanthanide ions [93,267–269], however no evidence has been found that these states can be metastable, as required to induce persistent luminescence.

The involvement of the trivalent codopant was also hypothesized by the electron trapping models by Clabau and Dorenbos (see Section 5.2) in 2005-2007. [87,172,239] This model rapidly gained importance in literature (see Figure 2(b)), however the hypothesis could not be proven for a long time due to a lack of direct experimental evidence. Only recently, Joos *et al.* [243] performed X-ray spectroscopy experiments on $Sr_4Al_{14}O_{25}$:Eu^{2+},Dy^{3+} and direct evidence for Eu^{2+}/Eu^{3+} and simultaneous Dy^{3+}/Dy^{2+} valence changes was collected (see Equation 4 and Figure 16). During these experiments, the dynamic equilibrium in Equation 4 could be shifted to the right (stimulating trapping by $4f^7 \rightarrow 4f^6 5d^1$ excitation of Eu^{2+}) or left (stimulating detrapping by $4f^{10} \rightarrow 4f^9 5d^1$ excitation of Dy^{2+}) by illumination with violet and infrared lasers, respectively. Importantly, the identified photoredox process showed the same time-evolution as the charging of the radiolumines-

cence of Eu^{2+} (Figure 16(b)) and a small decrease in the radioluminescence of Dy^{3+} (Figure 16(c)), evidencing that this process indeed underlies the trapping and detrapping. Further analysis showed that a large fraction of the electrons coming from europium are trapped by dysprosium suggesting that, at least in the codoped materials, the contribution of intrinsic or charge-compensating defects to the trapping process in $Sr_4Al_{14}O_{25}$:Eu^{2+},Dy^{3+} is limited.

It is generally assumed that only two species are involved in the trapping and detrapping processes, i.e. the activator and the trap. This assumption has not been verified and it cannot be excluded *a priori* that an intermediate state is formed where the transferred electron is temporarily localized at an auxiliary defect that bridges between the Eu activator and the (Dy) trap. This auxiliary defect can be fixed in the crystal structure or be mobile in the vicinity of the activator and the trap. This hypothetical mechanism corresponds to local trapping as the electron is never delocalized. A notable example of a charge-compensating defect which is known to participate in electron transfer processes and which is mobile at the same time is a fluoride interstitial, F_i, in fluorite-type crystals. [269, 270] Unless LnF_3 precursors are used for synthesis, fluorine-related defects are not expected in aluminate phosphors, however it is thinkable that interstitial hydrogen, H_i (see Section 5.4), can play a similar role. In any case, dedicated experiments are required to clarify whether these kinds of mechanisms are at play.

6 Energy level models for persistent luminescence

Numerical models that describe the dynamics of trapping and detrapping phenomena such as the Randall-Wilkins model [155] for first order kinetics (see Section 4.1) make no explicit assumptions on the underlying energy level structure and consider a generic few-level system which is strongly simplified compared to a real electronic structure. As a consequence, these models make no assumptions on the chemical details provoking trapping and detrapping and their usefulness to optimize existing or engineer new persistent phosphors is therefore limited.

As such, there is a strong demand for an adequate atomistic model that explains trapping and detrapping phenomena and takes the full chemical detail of the crystal with its relevant defects and impurities into account. As argued in a previous paragraph, there is no direct experimental evidence that indicates whether trapping/detrapping occurs either locally or globally. Nonetheless, models

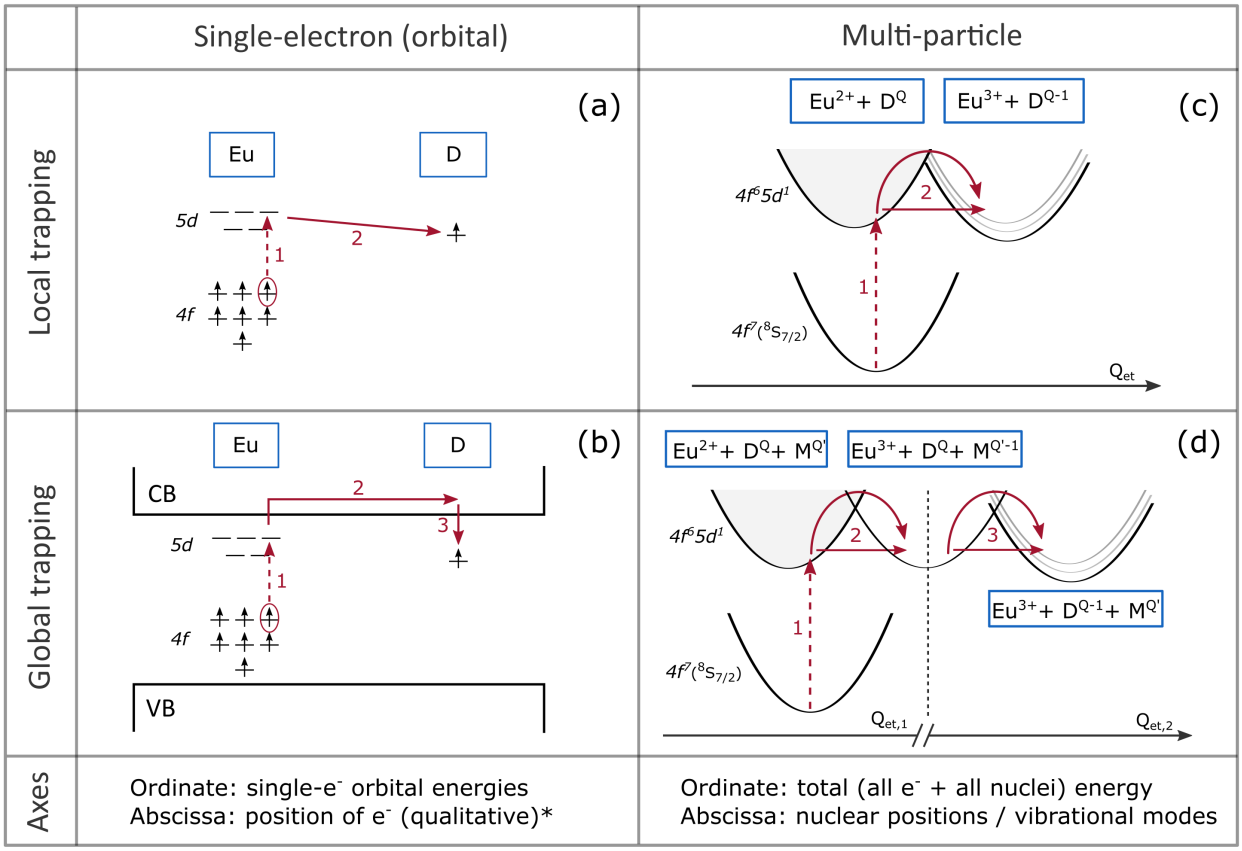

*Band structures, calculated under periodic boundary conditions, show the orbital energies of the particles as a function of their wave vector (k_x, k_y, k_z) in the first Brillouin zone.

Figure 17: Qualitative overview of how global and local trapping models can be represented in orbital (single-electron) and multi-particle energy level schemes for electron trapping from Eu^{2+} to a trap D^Q (see Eq. 5). In all cases, electron trapping at a defect D is represented. In a local model, the transfer is direct, without intermediate states, while in a global (i.e. non-local) model, the electron is delocalized on the cationic sublattice (represented by the metal-to-metal charge transfer (MMCT) with host cation M, i.e. the CB in single-electron language). The relative energies in these energy level schemes were arbitrarily chosen to clearly visualize the possible mechanisms and it should be noted that these do not necessarily correspond to physical reality.

involving delocalized conduction band (CB) electrons or valence band (VB) holes are ubiquitous in literature, and delocalized (i.e. global) models beat local models in terms of popularity by far. In the following, both perspectives are discussed and the possible theoretical frameworks that can be used to describe them are elaborated. Finally, two popular examples from literature are discussed in detail and their successes and shortcomings are highlighted.

6.1 General theoretical considerations

6.1.1 Orbital vs. multi-particle energy level schemes

Before resorting to the more detailed discussion below, it is useful to briefly elaborate on the quantum mechanical origin of energy level models. Regardless of the local or non-local character of the trapping, two distinct and mutually incompatible types of energy level schemes exist, orbital (i.e. single-electron) and multi-particle diagrams. [271] Figure 17 gives a qualitative picture of orbital and multi-particle energy level schemes, applied to a local and global model for electron transfer from Eu^{2+} to a trap of unspecified chemical nature, given by following redox process:

$$Eu^{2+} + D^{Q} \underset{\text{detrapping}}{\overset{\text{trapping}}{\rightleftharpoons}} Eu^{3+} + D^{Q-1}, \tag{5}$$

where electron trapping is assumed (i.e. Eu^{2+} is oxidized to Eu^{3+} during trapping) in accordance with the experimental evidence (see Section 5.2) and a generic trapping defect D with equilibrium charge Q is used. If D = Dy and $Q = 3$, the experimentally verified process from Equation 4 is retrieved.

Orbital or single-electron diagrams follow from a mean-field description of an electronic system. [272, 273] This means that complex electron-electron repulsion interactions are approximated by a mean field that affects every electron individually. Orbital states are displayed on an energy scale, indicating the binding energy of the individual electrons and every orbital can either be occupied by an electron (or two electrons with anti-parallel spins if no magnetic or spin-orbit effects are considered) or be empty. Atomic and molecular orbital diagrams [274], e.g. in ligand field theory [275], as well as band diagrams in solid state physics [276,277] are prototypical examples. Given a number of electrons, the lowest-energy orbitals are filled according to Fermi-Dirac statistics up to

the Fermi level which coincides with the $4f$ orbitals in case of a lanthanide-doped insulator (7 out of 14 are filled in the Eu^{2+} ground state). [278] Excited states can be represented as particle-hole excitations, where an electron is moved from below the Fermi level to an empty orbital above the Fermi level. This is illustrated for a local and global trapping model in Figure 17(a,b). Due to the mean-field approximation which is inseparably connected to their notion, orbital diagrams are fundamentally unable to represent a quantitatively correct picture of a compound and its excited states. Firstly, electron correlation effects lead to a breakdown of the mean field approximation and physical eigenstates cannot be represented by a single electron configuration, requiring considerable contributions from multiple configurations. [279, 280] This is especially the case for lanthanide and transition metal systems [281–284], notably the systems of interest. Secondly, even if every excited state could be represented by an orbital diagram, which is not true for the first reason, different orbital energies are required for every distinct state because the particle-hole excitation affects the mean field itself. [285] These reasons indicate why an orbital diagram is not expected to lead to quantitatively correct explanations, e.g. the energy of spectroscopic transitions such as an Eu^{2+} $4f^7 - 4f^6 5d^1$ transition do not correspond to the orbital energy difference between the $4f$ and $5d$ orbitals. [93] As such, also qualitative models based on orbital diagrams should be treated with the highest caution.

Due to the ambiguity that arises from the use of orbital states for excited state of correlated electrons and electron transfer processes, the concept of charge-state transition levels is often used to visualize the redox chemistry of dopants in a single-electron picture, i.e. with valence and conduction bands. These levels were introduced by Shockley and Last in 1957 as a generalization of the orbital impurity levels (like they occur in the Luttinger-Kohn [286] or Slater-Koster [287, 288] models for defects) to circumvent the above-mentioned problems for defects that adopt multiple charge states. [289] They are pragmatically defined as the Fermi level location at which the impurity changes its charge state to minimize the total free energy of the system. As such every charge-state transition level is labeled by two charge states (e.g. Ln^{2+}/Ln^{3+}, or briefly 2+/3+ in Figure 18(a)). One should keep in mind that these impurity levels cannot be identified with energy levels in the sense that they are no solutions of an eigenvalue equation. Rather, they are thermodynamic (ground-state) concepts, indicating the relative stability of the different charge states of the impurity,

as verified by various experiments. [290] Under the assumption that a charge carrier is completely detached from the center from which it originates, charge-state transition levels are assessed in deep level transient spectroscopy (DLTS) and charge transfer absorption / luminescence. [255, 291] As explained before, the validity of this assumption is however questionable in case of light-induced charge-transfer processes in inorganic phosphors.

Multi-particle diagrams display the total energy of the electronic+nuclear system. In contrast to orbital diagrams where a mean-field approximation is adopted, no implicit assumptions on the level of theory are made in multi-particle diagrams and experimental accuracy can be achieved in principle. Configuration coordinate diagrams are often-encountered examples, displaying the total electronic+nuclear energy of the various electronic and/or electron-vibrational states along a one-dimensional cross-section of the space which is spanned by all possible nuclear coordinates (or equivalently, all vibrational modes). The selected coordinate, Q, represents a local vibrational mode at an active center, typically the breathing mode [292–294], or a suitable reaction coordinate in cases where multiple centers are involved, e.g. during electron transfer. [295] The energy eigenvalues in a crystal field theory (CFT, e.g. the Dieke or Tanabe-Sugano diagrams for lanthanide or transition metal ions, respectively [296–300]) approach represent a vertical cross-section at a fixed nuclear geometry. [301,302] The major advantage of multi-particle diagrams, next to their ability to unambiguously display electronic excited states, is that non-radiative transitions, possibly involving energy barriers that are crossed or tunneled through, can be visualized as well. [303] Furthermore, electron transfer processes can be displayed by adding the relevant electron-transfer excited states. In this case, the energy scale represents the total energy of all participating centers, i.e. the number of electrons is the same for all displayed energy levels. As an example in a local trapping model (see Figure 17(c)), both electron configurations (non-trapped and trapped), indicated by the left and right-hand-side of Eq. 5 give rise to energy levels with the same number of particles, however with strongly different equilibrium geometries associated with the oxidation/reduction of the involved centers. If a charge carrier is exchanged with the host crystal itself, i.e. in case of a global model (see Figure 17(d)), the associated multi-particle levels correspond locally to ligand-to-metal charge-transfer (LMCT, where the ligand corresponds to the host anions, i.e. the species forming the VB in orbital language) states or metal-to-metal charge-transfer (MMCT, where the receiving

metal corresponds to the host cations, i.e. the species forming the CB in orbital language, $M^{Q'}$ in Figure 17(d)) states in case of hole or electron trapping, respectively.

6.1.2 Trap depths and transition probabilities in global and local models

Relating trap depths and electron transfer probabilities to underlying chemical details is one of the greatest remaining challenges in the field of persistent phosphors. In this paragraph, we give some considerations on the differences and similarities of these quantities for global and local trapping mechanisms.

For global trapping/detrapping, the electron is completely delocalized and it occupies a conduction band state during its transfer. As shown in Fig. 17(d), energy barriers for detrapping (i.e. the trap depth, E_d) consist of an electronic and a vibrational contribution. Note that the latter is not represented in the orbital picture of Fig. 17(b). The electronic contribution depends only on the ionization potential of the acceptor (i.e. trap, D^{Q-1}/D^{Q}) and on the electron affinity of the host metal ions ($M^{Q'}/M^{Q-1}$). This shows that the trap depth for a given defect (or codopant) is independent of the activator (i.e. donor). The same rule holds for the energy barrier for trapping (E_t): the electronic contribution to this barrier depends only on the ionization potential of the donor (here Eu^{2+}/Eu^{3+}) and the electron affinity of the host cations, not on the chemical nature of the trap. In summary, as activators and traps are not directly interacting and electron transfer occurs via the conduction band, energy barriers and also transition rates show no distance dependence in a global trapping/detrapping process.

For local trapping, the charge carrier is directly transferred between donor and acceptor. This implies that the electronic contribution to the energy barriers for trapping and detrapping are determined from both the ionization potential of the donor (here Eu^{2+}/Eu^{3+}) and the electron affinity of the acceptor (D^{Q-1}/D^{Q}). Changing either activator or trap will in general have an effect on all associated energy barriers in contrast to the global trapping model. Additionally, a donor-acceptor distance dependence on the energy barriers can exist for a local trapping mechanism which is another difference with respect to a global trapping mechanism. At lowest level and for long ranges, this interaction can be approximated by its electric monopole-monopole contribution,

similar to the recombination energy in the context of donor-acceptor pair luminescence [304–306]:

$$\Delta E(d_{\mathrm{DA}}) = \Delta E_0 + \frac{e^2(q_{\mathrm{A}} - q_{\mathrm{D}} - 1)}{4\pi\epsilon d_{\mathrm{DA}}}, \tag{6}$$

with d_{DA} the donor-acceptor distance, ϵ the dielectric constant of the host and q the Kröger-Vink charges [307] of donor (D) and acceptor (A). ΔE_0 is the distance-independent contribution. This leading-order contribution is zero for the case of Eu^{2+}-Dy^{3+} pairs in strontium aluminates (i.e. $q_{\mathrm{A}} = 1$ and $q_{\mathrm{D}} = 0$ hence $q_{\mathrm{A}} - q_{\mathrm{D}} - 1 = 0$). For many other scenarios, e.g. when a native defect plays the role of trap, it is thinkable that this monopolar contribution dominates the distance dependency.

Also the electron transfer rates are expected to show a distance dependence in a local model as they are expected to scale with the overlap of the initial and final state wave functions. Very often, an exponentially damped transition probability has been assumed, suggesting that electron transfer can only occur on a very short range. However, it should be remarked that the exponential damping of wave functions, or more exactly of the electron-electron coupling, is a hallmark for atoms or molecules in free space. In matter, i.e. within a molecule or in a crystal, it has been shown that the electron-electron coupling decreases much slower, according to an inverse power law [308], facilitating electron transfer processes across much larger distances, even for a local, i.e. direct trapping and detrapping mechanism. Experimentally, it has indeed been shown that direct electron transfer between transition metal ions in (non-aromatic, fully saturated) hydrocarbon chains of variable length can range up to 25 Å, which indeed suggests that local (or direct) trapping and detrapping is not necessarily restricted to a short range [309].

Up to now, we focused on the electronic contribution to energy barriers, given by the vertical offsets between the parabolic potential energy curves in Figs. 17(c,d). However, the height of barriers is to a large extent also determined by a vibrational contribution, which is often ignored when models for persistent luminescence or any other phenomenon for trapping and detrapping are given [271, 310]. As can be seen in Figs. 17(c,d), the magnitude of the vibrational contribution to energy barriers is determined by the curvature of the potential energy curves as well as their horizontal offset. The former follows directly from the local vibrational frequencies, especially the vibrational frequency of the relevant electron transfer mode (Q_{et} in Fig. 17). The latter follows

from the differences in atomic geometry (e.g. bond length differences) before and after the electron transfer, which increases with an increasing ionic radius of the cation for which the lanthanide dopants substitute [311, 312].

Empirically, trap depths are mostly obtained by computerized glow curve fitting using mathematical expressions that are typically based on a single-barrier model [154,313] such as the Randall-Wilkins expression (Equation 1). This model assumes a one-dimensional, infinitely long potential step, compatible with flat band-diagrammatic pictures as in Figure 17(a,b). This is however a fundamentally different picture than the one of an electron-vibrational model as illustrated in Figure 17(c,d). The latter features more realistic double-well potentials that also allow tunneling due to their finite width. This process can also show a temperature-dependence due to the curvature of the barrier in addition to a non-thermal contribution originating from the zero-point vibrations whose importance depends on the details of the potentials wells. [314, 315] For this reason it is hence questionable whether empirically obtained trap depths can be directly related to a realistic electronic structure. The obtained parameters should rather be regarded as effective parameters that can capture the emergent dynamics of an underlying physical reality which is much more complex. [316–318] Similar conclusions have been drawn for thermal quenching through outside crossover. [319–321] These considerations give a more subtle and less ambiguous picture on tunneling processes compared to its popular use in persistent luminescence where local processes which are not thermally activated are considered as 'tunneling' (Figure 17(a)), as opposed to delocalization (Figure 17(b)).

Experimental validation whether or not a distance-dependence on trap depths and transition rates exists, verifying or falsifying a local (de)trapping, is not straightforward. However, in a recent study Murayama *et al.* [322] investigated the differences between a synthesis under reducing atmosphere or a synthesis in air, followed by a reduction step at lower temperature. They observed a higher persistent luminescence intensity for the sample prepared under the latter conditions. This might be tentatively attributed to the fact that under these conditions the Eu and the Dy are both incorporated in a trivalent state (before reduction) and tend to cluster. However, this hypothesis has not been experimentally verified yet.

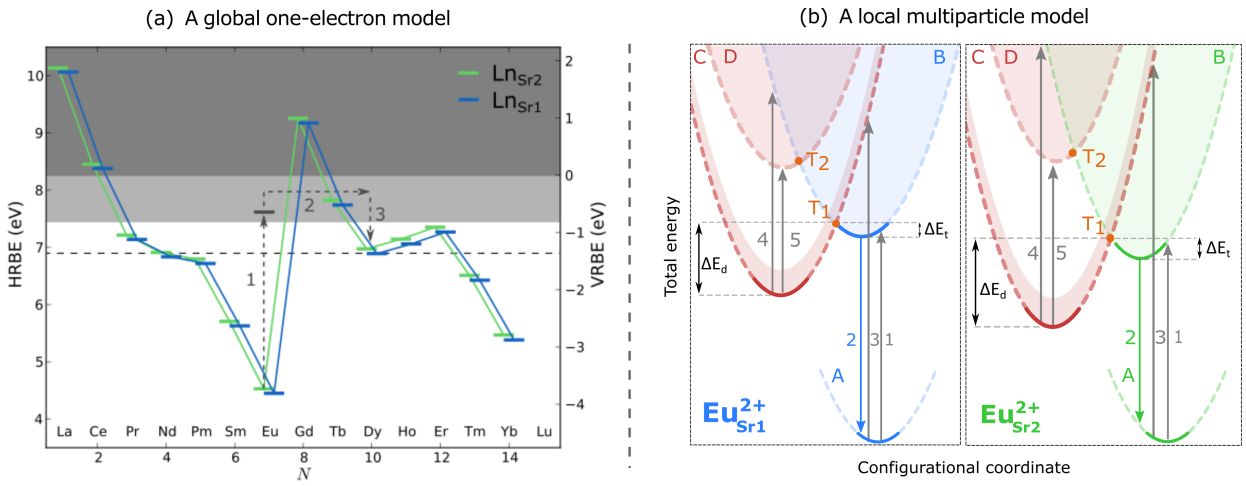

Figure 18: (a) Band diagram showing the 2+/3+ charge-state transition levels for all lanthanides on both nonequivalent Sr sites in $SrAl_2O_4$:Eu^{2+},Dy^{3+}. The binding energy is referred with respect to the VB top (host-referred binding energy, HRBE) or to the vacuum level (vacuum-referred binding energy, VRBE). The dashed lines indicate how this diagram is used as a global model for the persistent luminescence in this phosphor regardless of the questionable physical grounds of hybrid single-electron / multi-electron energy level schemes (see text). Reproduced with permission from Botterman *et al.*. [59] Copyright 2014 by the American Physical Society. (b) A local model to describe the persistent luminescence mechanism in $SrAl_2O_4$:Eu^{2+},Dy^{3+} for Eu_{Sr1} (left) and Eu_{Sr2} (right).

6.2 Examples

Below, two models are discussed in more detail. These are obviously not the only possible models to describe trapping/detrapping, but were selected based on its popular use (6.2.1) or because of its elegance in explaining various observations not explained by other models (6.2.2).

6.2.1 A global single-electron model

The majority of the models for persistent luminescence that can be found in literature somehow involve the creation of VB holes or CB electrons, displayed via single-electron band diagrams. Most popular is the model that assumes electron trapping where a CB electron is created as an intermediate step (see Figure 17(b)). As this electron is delocalized in a CB orbital, it can move through the entire crystal until it is trapped at the defect D. This model is adopted from early work of S. P. Keller and coworkers on electron transfer between lanthanide pairs in infrared photostimulable phosphors [323, 324] and is currently attributed to Dorenbos [239], who devised methods to draft empirical band diagrams for lanthanide-doped solids from limited experimental input based on

inter- and extrapolation of previously collected data and systematic trends, e.g. on the ionization potentials across the $4f$ series. [6] The typical band diagram, including charge-state transition levels (2+/3+) of the 14 lanthanide (Ln) ions, is shown in Figure 18(a).

Explaining persistent luminescence on the basis of Figure 18(a) is done by adding the $4f^7 - 4f^6 5d^1$ transition energies of the Eu^{2+} ion to the location of the charge-state transition level as one would do in a multi-particle diagram (arrow 1). Consequently, one arrives somewhere resonant with the CB orbitals or still in the forbidden gap, but close to the CB bottom. This is then used as an argument for the delocalization of the electron in a CB orbital (photoionization, arrow 2). Next, the CB electron can be trapped at a defect that has a charge-state transition level somewhere in the forbidden gap (arrow 3). Detrapping follows the opposite path and can occur thermally, by bridging the energy difference between the CB bottom and the charge-state transition level of the trap, or optically in a similar way as the Eu^{2+} ion was originally photoionized. If a trivalent codopant acts as the trapping defect, the 2+/3+ charge-state transition levels in Figure 18(a) is used as energy level for the trap and an associated zig-zag trend is expected in e.g. the TL glow curve positions for different codopants. In fact, this correspondence has been found in several lanthanide co-doped compounds, notably Ce^{3+},Ln^{3+} co-doped crystals such as $NaLaF_4$ [325], YPO_4 [153,326], $LuPO_4$ [326], Sr_3AlSiO_5 [327] and $GdAlO_3$ [328] and is often used to justify the global trapping model, represented in Figure 18(a). However, this characteristic zig-zag shape originates from the systematics in ionization potentials of the lanthanide ions. As a consequence, the establishment of a zig-zag trend for the TL glow curves only indicates that a removal of an electron from the $4f$ shell of the codopant is involved, regardless of the local/global character of the trapping, which was already correctly concluded by Nakazawa *et al.* in 1997. [95] Recently, it was shown, via *ab initio* quantum chemical calculations, that local, direct electron transfer between lanthanide ions (as in Figure 17(c)) gives rise to the same systematics. [246] The observation of zig-zag trends as a function of $4f$ shell occupation can hence not be used to distinct a global from a local trapping mechanism.

As charge-state transition levels are no electronic eigenstates and excited states cannot be represented in the same orbital diagram as the ground state, physical grounds for this model are lacking on the most fundamental level. This criticism pertains to the energy level diagrams themselves

and is independent of the local or global character of trapping. In fact, global trapping can be unambiguously described in a multi-electron picture (see Figure 17).

6.2.2 A local multiparticle model

As reviewed in §5.3, the interpretation of several independent experiments suggests that the trapping and detrapping processes after visible or near-UV photon absorption are local phenomena, in contrast to the most popular, global, model summarized above. In this paragraph, a local model is proposed as an alternative. Rather than having the pretentiousness to come up with a final model that explains all properties of the given class of persistent phosphors, it aspires to open up the discussion and move away from the beaten track.

The electronic states of activator-trap complexes are described by means of a multi-particle configurational coordinate diagram, as originally proposed by Piepho *et al.* as a theoretical framework for electron transfer. [295] Figure 18(b) shows how the Eu_{Sr1} and Eu_{Sr2} centers are coupled to a trapping defect of unspecified chemical nature, denoted as D^Q, able to undergo the general (photo)redox process of Eq. 5.

The lowest curves (curves A) represent the ground state of the Eu^{2+}-D^Q pair. The excited states of this complex are represented by curves B and are build up from all pair states, constructed by combining the excited states of Eu^{2+} (essentially the dense $4f^6 5d^1$ manifold, see e.g. [80, 93]) with the excited states of D^Q. During trapping an electron is transferred from Eu^{2+} to D^Q, forming the Eu^{3+}-D^{Q-1} configuration by intersystem crossing. This configuration contains the same number of electrons and its states can be straightforwardly displayed on the same energy scale (in red in Figure 18(b)). The lowest curves (curves C) correspond to the lowest state of the Eu^{3+}-D^{Q-1} configuration, which is metastable as required for trapping, while the higher curves (curves D) represent all the possible combinations of excited states of Eu^{3+} and D^{Q-1}. This electron transfer goes along with a shrinking of the Eu-O polyhedron, following the oxidation from Eu^{2+} to Eu^{3+}, and a simultaneous expansion of the environment around the trapping defect due to its reduction. This reorganization of nuclear positions is represented by the electron transfer coordinate, Q_{et}, which signifies the path through the saddle point (transition state) between both potential energy minima.

The trapping process starts with the excitation of Eu^{2+} from the $4f^7$ ground state to a $4f^6 5d^1$ excited state (arrow 1). Immediate de-excitation is possible and gives rise to the emission of a blue or green photon (arrow 2) but if the thermal energy is sufficient to reach the first crossing point (T_1) an electron transfer from Eu^{2+} to the trap can take place and the system will relax to the lowest state of the Eu^{3+}-D^{Q-1} configuration (curve C). It is evident from Figure 18(b) that the energy barrier for trapping, ΔE_t, is larger for Eu_{Sr2} than for Eu_{Sr1} which is in line with the site-dependent thermally activated trapping as found by Botterman *et al.* [59] and Hagemann *et al.* [177] Moreover, trapping can also be induced directly through excitation to the charge transfer band (arrow 3) which is located at higher energy. The latter transition is however expected to have a significantly lower transition probability due to the distance between the involved $4f$ orbitals (see also §6.1.2). [131]

Detrapping of the electron can take place through two physically different pathways. Firstly, thermally activated detrapping occurs when the thermal energy is sufficient to cross or tunnel the barrier (T_1) between the Eu^{3+}-D^{Q-1} ground state (curve C) and the Eu^{2+}-D^{Q} excited state (curve B). The former process gives rise to afterglow or thermoluminescence and is characterized by a thermal trap depth ΔE_d.

Secondly, optical excitation from the lowest state of the Eu^{3+}-D^{Q-1} configuration (arrow 5) can also result in detrapping, but this time through crossing point T_2. This transition leads to optically stimulated luminescence which might be subject to a smaller or even negligible energy barrier (see Figure 18(b)). In both cases the electron transfer from the trap to europium occurs via a crossing of the energy surfaces but the electron back-transfer can also be induced through direct excitation to the charge transfer band (arrow 4). As for arrow 3, this transition is also expected to have a low transition probability. [131]

The energy diagram in Figure 18(b) protrudes an observation of general importance: details of the potential energy curves/surfaces are critical to understand trapping and detrapping processes, both qualitatively as quantitatively. Specifically, curvatures (i.e. local phonon energies) and horizontal offsets (i.e. rearrangements in equilibrium nuclear positions) have an important effect on potential energy barriers and hence trap depths: more rigid compounds (higher phonon energies) will automatically lead to higher barriers, so will compounds that feature larger structural differ-

ences between non-trapped and trapped states. Furthermore, this figure indicates an asymmetry between the barriers for trapping and detrapping caused by the curvatures of the potential energy surfaces, which corresponds to experiments for various phosphors. [59, 329] These essential effects are not grasped by 'flat' atomic-like energy level schemes and band diagrams. This observation strongly suggests that persistent luminescence can only be understood if these details of the atomic geometry are properly taken into account, regardless of the local or global character of the trapping.

7 Benchmarking: where do we stand?

The report by Matsuzawa *et al.* in 1996 represented a spectacular increase in both initial intensity (around 1 cd/m^2) and afterglow duration (> 30h) with respect to non-codoped $SrAl_2O_4$:Eu^{2+} (initially around 20 mcd/m^2) or ZnS:Cu sensitized by radioactive promethium or tritium (initially around 90 mcd/m^2). [21] Since then many efforts have been directed at further improving the afterglow intensity and duration by slightly changing the synthesis conditions or phosphor compositions. Nevertheless, it appears that there is still a large margin for improvement. In 2011, only a 4% increase in the Eu^{3+}-signal was detected during time-dependent Eu L_{III}-edge XANES measurements, where charging was performed with X-rays. Using optical charging, the storage capacity of 1 gram of commercial $SrAl_2O_4$:Eu^{2+},Dy^{3+},B^{3+} was measured and it was found that only about 1.6% of the europium ions are ionized when the phosphor is charged to its maximal capacity using blue light. [330]

Large differences in sample morphology, spectrum and intensity of the excitation source make it difficult to identify where we stand in terms of the performance of the state-of-the-art of $SrAl_2O_4$ phosphors. An example of a seemingly spectacular improvement can be found in glass ceramics, which often yield high luminances because they possess a considerably larger optical penetration depth compared to powder samples. [331–333] After 25 years of research, it is time to draw up the balance by comparing several commercial powders from five different manufacturers (A-E) and single crystals of $SrAl_2O_4$:Eu^{2+},Dy^{3+} from one manufacturer (F) in a benchmarking study. The evaluation of these commercial phosphors was performed using two complementary approaches.

First, a conventional evaluation of the afterglow intensity of a flat powder surface or single crystal after exposure to 1000 lux of white light from a Xe-arc source during 5 minutes was performed to

Table 1: Storage capacities (measured after excitation with blue light) and afterglow times and relative initial intensities (measured after illumination with 1000 lux of white light from a Xe arc source for 5 minutes) of the $SrAl_2O_4$:Eu^{2+},Dy^{3+} powders and single crystals (diameter 5.3 mm, height 0.95/2.40/5.40 mm) used in the benchmarking study. The storage capacity of sample B1 has been taken from Van der Heggen *et al.* [330] Particle sizes correspond to d_{10}-d_{90} or d_{50}, depending on whether one or two values are given.

Sample ID	**Type** (size)	**Eu** (mol%)	**Dy** (mol%)	**Storage capacity** (photons/gram)	**Afterglow** Time (h)	I_0
A1	Powder (15-40 µm)	1.00	0.25	$(1.35 \pm 0.07) \cdot 10^{17}$	98.6	23%
A2	Powder (15-40 µm)	1.00	0.50	$(1.22 \pm 0.06) \cdot 10^{17}$	71.1	17%
B1	Powder (5-10 µm)	0.90	1.60	$(1.57 \pm 0.03) \cdot 10^{17}$	55.8	21%
B2	Powder (15-45 µm)	0.90	1.20	$(8.75 \pm 0.44) \cdot 10^{16}$	51.7	21%
C1	Powder (95 ± 15 µm)	-	-	$(2.03 \pm 0.11) \cdot 10^{17}$	83.9	29%
D1	Powder (55-75 µm)	< 1.20	< 1.10	$(1.01 \pm 0.05) \cdot 10^{17}$	87.7	24%
D2	Powder (65-85 µm)	< 1.20	< 1.10	$(1.43 \pm 0.08) \cdot 10^{17}$	89.6	30%
E1	Powder (15-35 µm)	~ 0.8	~ 0.3	$(2.00 \pm 0.10) \cdot 10^{17}$	37.2	24%
E2	Powder (20-40 µm)	~ 0.8	~ 0.3	$(1.81 \pm 0.10) \cdot 10^{17}$	64.1	19%
F1	Single crystal (0.95 mm)	-	-	$(4.04 \pm 0.41) \cdot 10^{16}$	28.0	31%
F2	Single crystal (2.40 mm)	-	-	$(3.56 \pm 0.36) \cdot 10^{16}$	46.2	63%
F3	Single crystal (5.40 mm)	-	-	$(3.71 \pm 0.38) \cdot 10^{16}$	77.8	100%

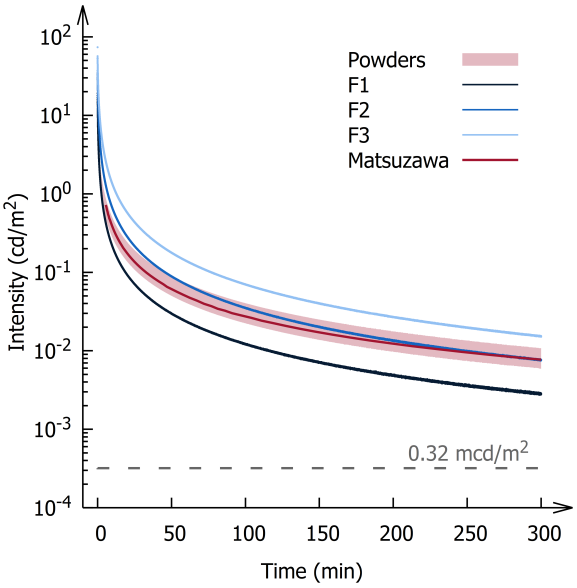

Figure 19: Afterglow decay curves measured after illumination with 1000 lux of white light from a Xe-arc source during five minutes. The shaded red area illustrates the range containing the best performing sample of each manufacturer. The red curve serves as a reference and was reproduced from Matsuzawa *et al.* [21] and was recorded after exposure to 200 lux of light with a D65 spectrum during 5 minutes. See Table 1 for the corresponding afterglow times and relative intensities and further details of the samples.

evaluate the performances of the materials under standardized conditions that are representative for operating conditions in most applications. The resulting afterglow times (i.e. the time until the threshold intensity of 0.32 mcd/m^2 is reached) and relative initial intensities (averaged over the first 10 seconds after excitation has stopped) are summarized in Table 1. Two conclusions can readily be drawn. First, the single crystals largely benefit from their increased optical transparency and yield considerably higher initial intensities (up to 45.1 cd/m^2 for the largest crystal) when compared to the powders. The initial intensity does not increase linearly with the size of the crystals but more research is needed to explain this behaviour. In Figure 19 the best performing powder of each manufacturer and the single crystals are compared to the performance of the sample created and reported by Matsuzawa *et al.* in 1996. It is clear that the state-of-the-art is not performing spectacularly better despite the different illumination conditions used by Matsuzawa *et al.* (200 lux D65, 5 minutes).

While the previous approach is valuable for the assessment of the material's application potential,

it provides little insight into the physical limits on the maximum amount of energy storage in these state-of-the-art samples. Hence, it is also insightful to measure the storage capacity [330] which is independent of the physical dimensions of the single crystals or powders and represents the number of photons that are emitted per gram of phosphor. In this approach the powder is incorporated in a transparent polymer according to the procedure described in [330] and is not exposed to white light but rather to blue light (455 nm, 23.4 mW/cm^2) as it has already been demonstrated multiple times that the storage capacity is much higher after exposure to more monochromatic blue light when compared to UV or white light. [90,334] The storage capacity can be calculated by integrating the photon emission rate during the full afterglow of this phosphor inside the polymer layer. This can be calculated according to the following prescription: [330]

$$N_\gamma = \int \int \frac{L(t,\theta)A}{\eta \overline{E}_\gamma} \mathrm{d}\Omega \mathrm{d}t \tag{7}$$

Here $L(t,\theta)$ is the recorded luminance as a function of time and solid angle in cd/m^2, A is the surface area of the polymer layer, η is the luminous efficacy of radiation in lm/W which can be calculated from the emission spectrum and $\overline{E}_\gamma$ is the average photon energy. More details on the practical aspects to determine the storage capacity, such as the phosphor loading in the polymer layer, can be found in ref. [330]. The storage capacities are summarized in Table 1 together with some details on the grain sizes and dopant concentrations when available. The results of the single crystal samples (F1-F3) emphasize the usefulness of this parameter as it takes into account the mass of the sample at hand and is hence independent on the size of the crystal. It appears that the storage capacity is largely independent of the Dy-concentration which might indicate that all samples are close to the solubility level of Dy (Section 3.2). Alternatively, optically stimulated detrapping by excitation light (see Section 4.2) will limit the storage capacity and the magnitude of this effect depends only on the amount of filled traps and not on the amount of empty traps (i.e. Dy^{3+} available. It is interesting to note that despite the differences in grain sizes and concentrations, all samples have similar storage capacities, i.e. integrated intensities, and only the initial brightness and decay rate vary between powder samples further emphasizing the poorly understood microscopic characteristics at play.

8 Conclusions and perspective

Without any doubt it can be said that $SrAl_2O_4$:Eu^{2+},Dy^{3+} has had a disruptive effect on (persistent) luminescence research. Its discovery did not only represent a great technological advancement at the time but also started a whole new discipline in luminescence research. Based on the initial concept described by Matsuzawa *et al.* [21] hundreds of persistent luminescent compounds have been developed. Careful tuning of the properties has resulted in a variety of phosphors emitting from the UV to the infrared and each operating at a specific optimal working temperature, [171] thereby paving the way towards a broader applicability of persistent luminescent materials beyond emergency signage and watch dials.

The intensive research performed over the last two decades has already resulted in some major insights into the details of the charge transfer processes that facilitate the persistent luminescence in phosphors. Even though $SrAl_2O_4$:Eu^{2+},Dy^{3+} has proven to be a tough nut to crack, its comparably large storage capacity has made it the prime model system whenever new and more challenging experimental approaches are being tested. The discoveries made on this benchmark material can undoubtedly be transferred to many other persistent luminescent compounds which are operating on a very similar principle. However, some of the details of the microscopic mechanism are still unknown and, as the benchmarking study suggests, this stands in the way of further improvements of the overall performance. Hence there is still ample work left to be done. From the overview presented here it becomes clear that the field of persistent luminescence is subjected to some often-encountered pitfalls that complicate the uncovering of this microscopic mechanism.

Some of these pitfalls are encountered when performing experiments on persistent phosphors. It is clear that most properties of persistent phosphors are highly dependent on the experimental conditions and sometimes even the experimental history of the phosphor. A detailed description of the performed experiments is hence indispensable. Without information about the excitation intensity, wavelength, sample temperature or sample composition it becomes nearly impossible to compare results and build upon previous work. Microscopic-structural changes can only be unambiguously related to trapping and detrapping processes if it is verified whether both exhibit the same time-dependency under identical conditions. Caution is however needed as shown by the discussion on photoconductivity in Section 5.2. Moreover, it is recommended to perform multiple

independent thermoluminescence, afterglow and fading experiments that are fitted simultaneously to the same set of parameters such as trap depths to ensure maximal predictability of the resulting fitted model.

Other pitfalls concern the interpretation of the experimental results. There appears to be a tendency to include a microscopic model (i.e. identification of trapping defects, intermediate states, energy level schemes etc.) in most articles about persistent luminescence. Unfortunately, these models rarely follow from the experimental results presented in the associated manuscript but are instead of a more speculative nature and often an alternative, equally (in)valid explanation exists. Instead, microscopic models should be based on direct, unambiguous experimental evidence, leaving little room for interpretation. The sheer multitude of models that are being proposed quite paradoxically impedes any meaningful advancement towards understanding persistent luminescence.

Remaining knowledge gaps were identified, posing challenges that will be encountered in the coming years. Firstly, a thorough investigation of the optical properties of the trapping defects, both empty and filled, is becoming unavoidable given that OSL by excitation light was found to drastically limit the phosphor's efficiency. Specifically, the identification of optically active trapping defects is needed to further improve the phosphor's storage capacity but more generally, knowledge about the absorption spectra of the trapping defects should enable a more straightforward identification of the involved trapping defects. Transient absorption spectroscopy (pump-push-probe) on short time scales could offer insights into the involvement of intermediate states (between activator and trap) and the dynamics of the trapping processes. For these optical experiments, the enhanced optical path length in the emerging single crystals might offer a crucial advantage to detect even the smallest absorption features of trapping defects.

Secondly, most investigations currently focus on the electronic structure of codopants as a way to explain why one lanthanide performs better than the other. The interplay between the electronic energy levels and the structural characteristics such as codopant size or activator-trap distances remain largely unexplored. A better understanding might however deliver insights into the origin of, for example, trap depth distributions. It has for example already been shown that these characteristics are important in the case of LaF_3 [335] and $BaTiO_3$ where the size of the dopant greatly influenced the trap depth of the defects. [336] This structural investigation is also closely related to

the way dopants are incorporated into the material and to what degree dopants cluster or aggregate near grain boundaries. Activator-trap distances are expected to have an important impact on the trapping and detrapping processes for direct (i.e. local) electron transfer while they do not matter when the electron transfer is mediated by the conduction band (i.e. global trapping). It is clear that, irrespective of the local or global character of the electron transfer, the often overlooked or ignored vibrational contribution to energy barriers for trapping and detrapping is of major importance to understand systematic behavior.

In general the design of dedicated experiments is needed, as well as a critical analysis and interpretation of their outcome. Combined optical and thermally stimulated luminescence measurements have already proven to be a very powerful tool to disentangle the contributions of different defects to a materials trap depth distribution. However, phosphor research could benefit from some cross-pollination with the field focusing on geological dating where other approaches are used on similar materials exhibiting the same trap-related luminescence phenomena. Linearly-modulated OSL [337] is, for example, applied as a way to differentiate different trapping defects based on their absorption cross-section by linearly increasing the stimulation intensity but also exo-electron measurements [338] hold potential as an alternative to photoconductivity measurements which are notoriously difficult on powder phosphors. This technique might provide a means to decouple the investigation of trapping and recombination centers; something that is not possible with OSL or TL, where information on the traps or detrapping routes is obtained indirectly through the luminescence of the recombination centers. More advanced techniques can provide direct insights into the chemical nature of the trapping defects. Electron paramagnetic resonance spectroscopy is gaining popularity to investigate the chemical nature of the paramagnetic defects in persistent phosphors. As an alternative, positron annihilation lifetime spectroscopy (PALS) allows to identify so-called open volume defects (e.g. vacancies) and can provide complementary information. [339]

Finally, the supportive role of quantum mechanical calculations, whose scope and accuracy keep on increasing, is highly desired. Currently, thermodynamic stabilities and charge states of defects, how they cluster and their ground-state atomic geometries are accessible via periodic-boundary DFT, whereas a wide range of excited states, including their atomic geometries and derived electronic spectra are obtainable from *ab initio* wave-function-theoretical methods. The

most important challenges that lie ahead require an expansion to more complex problems and to enlarge the list of properties that can be calculated. It is highly desirable to be able to tackle active centers with more than one lanthanide or multiple defects with incompletely filled shells. Combining electronic structure calculations with multi-state nuclear dynamics is a major challenge [340], but bears the promise to obtain vibronic couplings, leading to transition probabilities for radiative and non-radiative transitions in general and electron and energy transfer in particular. This is essential to determine the electron-vibrational origin of persistent luminescence.

The field of persistent luminescence is growing every year, which is appropriate because ample work is left to be done. The importance of future discoveries will transcend the field of luminescence and be of relevance for fields such as (personal) dosimetry, biomedicine, structural health testing and geological dating.

Acknowledgements

This work was supported by the French ANR PERSIST [18-CE08-0012]; the Research Foundation of Flanders (FWO) [G0F9322N, SB 1S48322N]; the UGent Special Research Fund (BOF) [BOF/PDO/2017/002101].

References

[1] E. F. Schubert, J. K. Kim, H. Luo, and J. Q. Xi. Solid-state lighting - a benevolent technology. *Reports on Progress in Physics*, 69(12):3069–3099, 2006.

[2] R.-J. Xie, N. Hirosaki, and T. Takeda. Wide color gamut backlight for liquid crystal displays using three-band phosphor-converted white light-emitting diodes. *Applied Physics Express*, 2(2):022401, 2009.

[3] H. A. Hoppe. Recent developments in the field of inorganic phosphors. *Angewandte Chemie-International Edition*, 48(20):3572–3582, 2009.

[4] D. Dutczak, T. Jüstel, C. Ronda, and A. Meijerink. Eu^{2+} Luminescence in Strontium Aluminates. *Physical Chemistry Chemical Physics*, 17:15236–15249, 2015.

[5] Y. Li, M. Gecevicius, and J. Qiu. Long persistent phosphors - from fundamentals to applications. *Chemical Society Reviews*, 45(8):2090–2136, 2016.

[6] P. Dorenbos. A Review on How Lanthanide Impurity Levels Change with Chemistry and Structure of Inorganic Compounds. *ECS Journal of Solid State Science and Technology*, 2(2):R3001–R3011, 2013.

[7] P. Xiong and M. Peng. Recent advances in ultraviolet persistent phosphors. *Optical Materials: X*, 2:100022, 2019.

[8] H. Shi and Z. An. Ultraviolet afterglow. *Nature Photonics*, 13(2):74–75, 2019.

[9] Y. M. Yang, Z. Y. Li, J. Y. Zhang, Y. Lu, S. Q. Guo, Q. Zhao, X. Wang, Z. J. Yong, H. Li, J. P. Ma, Y. Kuroiwa, C. Moriyoshi, L. L. Hu, L. Y. Zhang, L. R. Zheng, and H. T. Sun. X-ray-activated long persistent phosphors featuring strong UVC afterglow emissions. *Light: Science & Applications*, 7:88, 2018.

[10] X. Wang, Y. Chen, F. Liu, and Z. Pan. Solar-blind ultraviolet-C persistent luminescence phosphors. *Nature Communications*, 11:2040, 2020.

[11] X. Wang, Y. Chen, P. A. Kner, and Z. Pan. Gd^{3+}-activated narrowband ultraviolet-B persistent luminescence through persistent energy transfer. *Dalton Transactions*, 50(10):3499–3505, 2021.

[12] Y. Zhuang, Y. Katayama, J. Ueda, and S. Tanabe. A brief review on red to near-infrared persistent luminescence in transition-metal-activated phosphors. *Optical Materials*, 36(11):1907–1912, 2014.

[13] B. Viana, S. Sharma, D. Gourier, T. Maldiney, E. Teston, D. Scherman, and C. Richard. Long term in vivo imaging with Cr^{3+} doped spinel nanoparticles exhibiting persistent luminescence. *Journal of Luminescence*, 170:879 – 887, 2016.

[14] Z. Pan, Y. Y. Lu, and F. Liu. Sunlight-activated long-persistent luminescence in the near-infrared from Cr^{3+}-doped zinc gallogermanates. *Nature Materials*, 11(1):58–63, 2012.

[15] J. Xu, J. Ueda, Y. Zhuang, B. Viana, and S. Tanabe. $Y_3Al_{5-x}Ga_xO_{12}$:Cr^{3+}: A novel red persistent phosphor with high brightness. *Applied Physics Express*, 8(4):042602, 2015.

[16] K. Van den Eeckhout, P. F. Smet, and D. Poelman. Persistent Luminescence in Eu^{2+}-Doped Compounds: A Review. *Materials*, 3(4):2536–2566, 2010.

[17] K. Van den Eeckhout, D. Poelman, and P. Smet. Persistent Luminescence in Non-Eu^{2+}-Doped Compounds: A Review. *Materials*, 6(7):2789–2818, 2013.

[18] R. E. Rojas-Hernandez, F. Rubio-Marcos, M. Á. Rodriguez, and J. F. Fernandez. Long lasting phosphors: $SrAl_2O_4$:Eu, Dy as the most studied material. *Renewable and Sustainable Energy Reviews*, 81:2759–2770, 2018.

[19] J. Xu and S. Tanabe. Persistent luminescence instead of phosphorescence: History, mechanism, and perspective. *Journal of Luminescence*, 205:581–620, 2019.

[20] P. F. Smet, J. Botterman, K. Van Den Eeckhout, K. Korthout, and D. Poelman. Persistent luminescence in nitride and oxynitride phosphors: A review. *Optical Materials*, 36(11):1913–1919, 2014.

[21] T. Matsuzawa, Y. Aoki, N. Takeuchi, and Y. Murayama. A New Long Phosphorescent Phosphor with High Brightness, $SrAl_2O_4$:Eu^{2+},Dy^{3+}. *Journal of The Electrochemical Society*, 143(8):2670–2673, 1996.

[22] J. Botterman and P. F. Smet. Persistent phosphor $SrAl_2O_4$:Eu,Dy in outdoor conditions: saved by the trap distribution. *Optics Express*, 23(15):A868, 2015.

[23] L. Lyu, Y. Chen, L. Yu, R. Li, L. Zhang, and J. Pei. The Improvement of Moisture Resistance and Persistent Phosphors Coated with Silica - Polymer Hybrid Shell. *Materials*, 13:426, 2020.

[24] J. Nance and T. D. Sparks. Comparison of coatings for $SrAl_2O_4$:Eu^{2+},Dy^{3+} powder in waterborne road striping paint under wet conditions. *Progress in Organic Coatings*, 144:105637, 2020.

[25] V. Sharma, A. Das, and V. Kumar. Eu^{2+},Dy^{3+} codoped $SrAl_2O_4$ nanocrystalline phosphor for latent fingerprint detection in forensic applications. *Materials Research Express*, 3:015004, 2016.

[26] J. Zhang, J. Lin, J. Wu, S. Zhang, P. Zhou, X. Chen, and R. Xu. Preparation of long persistent phosphor $SrAl_2O_4$:Eu^{2+}, Dy^{3+} and its application in dye-sensitized solar cells. *Journal of Materials Science: Materials in Electronics*, 27:1350–1356, 2016.

[27] C. Wang, T. Xuan, J. Liu, H. Li, and Z. Sun. Long Afterglow $SrAl_2O_4$:Eu^{2+}, Dy^{3+} Phosphors as Luminescent Down-Shifting Layer for Crystalline Silicon Solar Cells. *International Journal of Applied Ceramic Technology*, 12(4):722–727, 2015.

[28] D. Nakauchi, G. Okada, M. Koshimizu, and T. Yanagida. Storage luminescence and scintillation properties of Eu-doped $SrAl_2O_4$ crystals. *Journal of Luminescence*, 176:342–346, 2016.

[29] O. Arellano-Tánori, R. Meléndrez, M. Pedroza-Montero, B. Castañeda, V. Chernov, W. Yen, and M. Barboza-Flores. Persistent luminescence dosimetric properties of UV-irradiated $SrAl_2O_4$:Eu^{2+}, Dy^{3+} phosphor. *Journal of Luminescence*, 128(1):173–184, 2008.

[30] D. Van der Heggen, R. Zilenaite, E. Ezerskyte, V. Fritz, K. Korthout, D. Vandenberghe, J. De Grave, J. Garrevoet, L. Vincze, D. Poelman, J. J. Joos, and P. F. Smet. A Standalone , Battery-Free Light Dosimeter for Ultraviolet to Infrared Light. *Advanced Functional Materials*, page 2109635, 2021.

[31] Y. Xiao, B. Luo, B. Cheng, Q. Huang, Y. Ye, L. Fang, L. Zhou, and S. Lei. Enhanced visible light catalysis activity of CdS-sheathed $SrAl_2O_4$:Eu^{2+},Dy^{3+} nanocomposites. *Dalton Transactions*, 47(24):7941–7948, 2018.

[32] L. Chen, Y. S. Zhang, C. Xue, X. R. Deng, A. Q. Luo, F. Y. Liu, and Y. Jiang. The green phosphor $SrAl_2O_4$:Eu^{2+}, R^{3+} (R=Y,Dy) and its application in alternating current light-emitting diodes. *Functional Materials Letters*, 06(04):1350047, 2013.

[33] B. Li, J. Zhang, M. Zhang, Y. Long, and X. He. Effects of $SrCl_2$ as a flux on the structural and luminescent properties of $SrAl_2O_4$:Eu^{2+}, Dy^{3+} phosphors for AC-LEDs. *Journal of Alloys and Compounds*, 651:497–502, 2015.

[34] C. N. Xu, X. G. Zheng, M. Akiyama, K. Nonaka, and T. Watanabe. Dynamic visualization of stress distribution by mechanoluminescence image. *Applied Physics Letters*, 76(2):179–181, 1999.

[35] C. N. Xu, H. Yamada, X. Wang, and X. G. Zheng. Strong elasticoluminescence from monoclinic-structure $SrAl_2O_4$. *Applied Physics Letters*, 84(16):3040–3042, 2004.

[36] C. S. Li, C. N. Xu, L. Zhang, H. Yamada, Y. Imai, and W. X. Wang. Dynamic Visualization of Stress Distribution by Mechanoluminescence Image. *Key Engineering Materials*, 388:265–268, 2009.

[37] G. J. Yun, M. R. Rahimi, A. H. Gandomi, G. C. Lim, and J. S. Choi. Stress sensing performance using mechanoluminescence of $SrAl_2O_4$:Eu (SAOE) and $SrAl_2O_4$:Eu, Dy (SAOED) under mechanical loadings. *Smart Materials and Structures*, 22(5):055006, 2013.

[38] S. Timilsina, K. H. Lee, Y. N. Kwon, and J. S. Kim. Optical Evaluation of In Situ Crack Propagation by Using Mechanoluminescence of $SrAl_2O_4$:Eu^{2+},Dy^{3+}. *Journal of the American Ceramic Society*, 98(7):2197–2204, 2015.

[39] Y. Fujio, C. N. Xu, Y. Terasawa, Y. Sakata, J. Yamabe, N. Ueno, N. Terasaki, A. Yoshida, S. Watanabe, and Y. Murakami. Sheet sensor using $SrAl_2O_4$:Eu^{2+} mechanoluminescent material for visualizing inner crack of high-pressure hydrogen vessel. *International Journal of Hydrogen Energy*, 41(2):1333–1340, 2016.

[40] J. S. Kim, Y. N. Kwon, and K. S. Sohn. Dynamic visualization of crack propagation and bridging stress using the mechano-luminescence of $SrAl_2O_4$: (Eu,Dy,Nd). *Acta Materialia*, 51(20):6437–6442, 2003.

[41] J. S. Kim. Application of Mechanoluminescence for the Dynamic Visualization of an Alumina Fracture. *Journal of Information Display*, 11(1):33–38, 2010.

[42] M. Sun, Z.-J. Li, C.-L. Liu, H.-X. Fu, J.-S. Shen, and H.-W. Zhang. Persistent luminescent nanoparticles for super-long time in vivo and in situ imaging with repeatable excitation. *Journal of Luminescence*, 145(145):838–842, 2014.

[43] A. S. Paterson, B. Raja, G. Garvey, A. Kolhatkar, A. E. V. Hagström, K. Kourentzi, T. R. Lee, and R. C. Willson. Persistent Luminescence Strontium Aluminate Nanoparticles as Reporters in Lateral Flow Assays. *Analytical Chemistry*, 86(19):9481–9488, 2014.

[44] T. Lécuyer, E. Teston, G. Ramirez-Garcia, T. Maldiney, B. Viana, J. Seguin, N. Mignet, D. Scherman, and C. Richard. Chemically engineered persistent luminescence nanoprobes for bioimaging. *Theranostics*, 6(13):2488–2524, 2016.

[45] H. Terraschke, M. Franzreb, and C. Wickleder. Magnetism and Afterglow United: Synthesis of Novel Double Core-Shell Eu^{2+}-doped Bifunctional Nanoparticles. *Chemistry - A European Journal*, 2020.

[46] N. Yu, F. Liu, X. Li, and Z. Pan. Near infrared long-persistent phosphorescence in SrAl2O4:Eu2+,Dy3+,Er3+ phosphors based on persistent energy transfer. *Applied Physics Letters*, 95(23):231110, 2009.

[47] J. B. Montes-Frausto, K. Juarez-Moreno, B. Can-Uc, and G. A. Hirata-Flores. Synthesis and cytotoxic effects of SrAl2O4 persistent luminescence nanoparticles co-doped with Eu2+/Dy3+ ions. *Optical Materials Express*, 6(5):1488–1499, 2016.

[48] D. S. Kshatri and A. Khare. Optical properties of rare earth doped strontium aluminate (SAO) phosphors: A review. *Optics and Spectroscopy (English translation of Optika i Spektroskopiya)*, 117(5):769–783, 2014.

[49] D. L. Fritzen, L. Giordano, L. C. V. Rodrigues, and J. H. S. K. Monteiro. Opportunities for Persistent Luminescent Nanoparticles in Luminescence Imaging of Biological Systems and Photodynamic Therapy. *Nanomaterials*, 10(10), 2020.

[50] D. Poelman, D. Van der Heggen, J. Du, E. Cosaert, and P. F. Smet. Persistent Phosphors for the Future: Fit for the Right Application. *Journal of Applied Physics*, 128(24):240903, 2020.

[51] A. Nag and T. R. Kutty. Role of B_2O_3 on the phase stability and long phosphorescence of $SrAl_2O_4$:Eu, Dy. *Journal of Alloys and Compounds*, 354(1-2):221–231, 2003.

[52] F. Massazza. The system SrO - Al_2O_3. *La Chimica e l'Industria*, 41:108–115, 1959.

[53] F. Ganits, T. Y. Chemekova, and Y. P. Udalov. The Al_2O_3 - SrO System. *Zhurnal Neorganischeskoi Khimii*, 24:471–475, 1979.

[54] M. Capron and A. Douy. Strontium dialuminate $SrAl_4O_7$: Synthesis and stability. *Journal of the American Ceramic Society*, 85(12):3036–3040, 2002.

[55] S. Ito, S. Banno, K. Suzuki, and M. Inagaki. Phase Transition in $SrAl_2O_4$. *Zeitschrift fur Physikalische Chemie*, 105(3-4):173–178, 1977.

[56] M. Avdeev, S. Yakovlev, A. A. Yaremchenko, and V. V. Kharton. Transitions between $P2_1$, $P6_3(\sqrt{3}A)$, and $P6_322$ modifications of $SrAl_2O_4$ by in situ high-temperature X-ray and neutron diffraction. *Journal of Solid State Chemistry*, 180(12):3535 – 3544, 2007.

[57] A.-R. Schulze and H. M. Buschbaum. Zur Verbindungsbildung von MeO: M_2O_3. IV. Zur Struktur von monoklinem $SrAl_2O_4$. *Zeitschrift für anorganische und allgemeine Chemie*, 475(4):205–210, 1981.

[58] J. J. Joos, D. Poelman, and P. F. Smet. Nonequivalent lanthanide defects: Energy level modeling. *Optical Materials*, 61:50–58, 2016.

[59] J. Botterman, J. J. Joos, and P. F. Smet. Trapping and detrapping in $SrAl_2O_4$:Eu,Dy persistent phosphors: Influence of excitation wavelength and temperature. *Physical Review B - Condensed Matter and Materials Physics*, 90(8):085147, 2014.

[60] V. Vitola, D. Millers, I. Bite, K. Smits, and A. Spustaka. Recent progress in understanding the persistent luminescence in $SrAl_2O_4$:Eu,Dy. *Materials Science and Technology*, 35(14):1661–1677, 2019.

[61] R. Hoppe. Effective Coordination Numbers (Econ) and Mean Fictive Ionic-Radii (Mefir). *Zeitschrift Fur Kristallographie*, 150(1-4):23–52, 1979.

[62] C. M. B. Henderson and D. Taylor. The structural behaviour of the nepheline family: (1) Sr and Ba aluminates (MAl_2O_4). *Mineralogical Magazine*, 45(337):111–127, 1982.

[63] K. Fukuda and K. Fukushima. Crystal structure of hexagonal $SrAl_2O_4$ at 1073K. *Journal of Solid State Chemistry*, 178(9):2709 – 2714, 2005.

[64] S. Ito, S. Banno, K. Suzuki, and M. Inagaki. Solid solubility in the $SrAl_20_4$-$BaAl_20_4$ system. *Zeitschrift fur Physikalische Chemie*, 107(1):53–56, 1977.

[65] V. Castaing, C. Monteiro, A. D. Sontakke, K. Asami, J. Xu, A. J. Fernández-Carrión, M. G. Brik, S. Tanabe, M. Allix, and B. Viana. Hexagonal $Sr_{1-x/2}Al_{2-x}Si_xO_4$:$Eu^{2+}$,$Dy^{3+}$ transparent ceramics with tuneable persistent luminescence properties. *Dalton Transactions*, 49(46):16849–16859, 2020.

[66] W. S. Shi, H. Yamada, K. Nishikubo, H. Kusaba, and C. N. Xu. Novel structural behavior of strontium aluminate doped with europium. *Journal of The Electrochemical Society*, 151(5):H97–H100, 2004.

[67] R. E. Rojas-Hernandez, F. Rubio-Marcos, A. Serrano, A. Rakhmatullin, C. Bessada, and J. F. Fernandez. Unveiling the role of the hexagonal polymorph on $SrAl_2O_4$-based phosphors. *RSC Advances*, 8:28918–28927, 2018.

[68] P. Boutinaud, D. Boyer, A. Perthue, R. Mahiou, E. Cavalli, and M. G. Brik. Spectroscopic investigations on $SrAl_2O_4$ polymorphs. *Journal of Luminescence*, 159:158–165, 2015.

[69] V. Vitola, D. Millers, K. Smits, I. Bite, and A. Zolotarjovs. The search for defects in undoped $SrAl_2O_4$ material. *Optical Materials*, 87:48–52, 2019.

[70] R. D. Shannon. Revised Effective Ionic Radii and Systematic Studies of Interatomic Distances in Halides and Chaleogenides. *Acta Crystalography*, A32:751, 1976.

[71] K. Kaiya, N. Takahashi, T. Nakamura, T. Matsuzawa, G. Smith, and P. Riedi. EPR studies of europium(II)-doped strontium aluminate phosphors. *Journal of Luminescence*, 87-89:1073–1075, 2000.

[72] T. Nakamura, K. Kaiya, N. Takahashi, T. Matsuzawa, C. C. Rowlands, V. Beltran-Lopez, G. M. Smith, and P. C. Riedi. High frequency EPR of europium(II)-doped strontium aluminate phosphors. *Journal of Materials Chemistry*, 10(11):2566–2569, 2000.

[73] F. C. Palilla, A. K. Levine, and M. R. Tomkus. Fluorescent Properties of Alkaline Earth Aluminates of the Type MAl_2O_4 Activated by Divalent Europium. *Journal of The Electrochemical Society*, 115(6):642, 1968.

[74] S. H. M. Poort, W. P. Blokpoel, and G. Blasse. Luminescence of Eu^{2+} in barium and strontium aluminate and gallate. *Chemistry of Materials*, 7(8):1547–1551, 1995.

[75] J. Ueda, T. Nakanishi, Y. Katayama, and S. Tanabe. Optical and optoelectronic analysis of persistent luminescence in Eu^{2+}-Dy^{3+} codoped $SrAl_2O_4$ ceramic phosphor. *physica status solidi (c)*, 9(12):2322–2325, 2012.

[76] J. Bierwagen, S. Yoon, N. Gartmann, B. Walfort, and H. Hagemann. Thermal and concentration dependent energy transfer of Eu^{2+} in $SrAl_2O_4$. *Optical Materials Express*, 6(3):793–803, 2016.

[77] D. Wang, Q. Yin, Y. Li, and M. Wang. Concentration quenching of Eu^{2+} in $SrO.Al_2O_3$:Eu^{2+} phosphor. *Journal of Luminescence*, 97(1):1–6, 2002.

[78] Z. Wu, J. Shi, J. Wang, H. Wu, Q. Su, and M. Gong. Synthesis and luminescent properties of $SrAl_2O_4$:Eu^{2+} green-emitting phosphor for white LEDs. *Materials Letters*, 60:3499–3501, 2006.

[79] B. Faridnia, M. M. Motlagh, and A. Maghsoudipour. Optimising synthesis conditions for long lasting $SrAl_2O_4$ phosphor. *Pigment and Resin Technology*, 36(4):216–223, 2007.

[80] L. Ning, X. Huang, Y. Huang, and P. A. Tanner. Origin of Green Persistent Luminescence of Eu-Doped $SrAl_2O_4$ from Multiconfigurational Ab Initio Study of $4f^7$-$4f^6 5d^1$ Transitions. *Journal of Materials Chemistry C*, 6:6637–6640, 2018.

[81] R. Shi, M. Qi, L. Ning, F. Pan, L. Zhou, W. Zhou, Y. Huang, and H. Liang. Combined Experimental and ab Initio Study of Site Preference of Ce^{3+} in $SrAl_2O_4$. *The Journal of Physical Chemistry C*, 119(33):19326–19332, 2015.

[82] M. Nazarov, M. Brik, D. Spassky, and B. Tsukerblat. Crystal field splitting of 5d states and luminescence mechanism in $SrAl_2O_4$:Eu^{2+} phosphor. *Journal of Luminescence*, 182:79–86, 2017.

[83] M. Nazarov, M. G. Brik, D. Spassky, B. Tsukerblat, A. Nor Nazida, and M. N. Ahmad-Fauzi. Structural and electronic properties of $SrAl_2O_4$:Eu^{2+} from density functional theory calculations. *Journal of Alloys and Compounds*, 573:6–10, 2013.

[84] P. Dorenbos. Relating the Energy of the [Xe]$5d^1$ Configuration of Ce^{3+} in Inorganic Compounds with Anion Polarizability and Cation Electronegativity. *Physical Review B*, 65(23):235110, 2002.

[85] P. Dorenbos. Crystal Field Splitting of Lanthanide $4f^{n-1}$5d-Levels in Inorganic Compounds. *Journal of Alloys and Compounds*, 341(1-2):156–159, 2002.

[86] P. Dorenbos. Relation between Eu^{2+} and Ce^{3+} f $\leftrightarrow$ d-Transition Energies in Inorganic Compounds. *Journal of Physics: Condensed Matter*, 15(27):4797–4807, 2003.

[87] F. Clabau, X. Rocquefelte, S. Jobic, P. Deniard, M.-H. Whangbo, A. Garcia, and T. Le Mercier. Mechanism of Phosphorescence Appropriate for the Long-Lasting Phosphors Eu^{2+}-Doped $SrAl_2O_4$ with Codopants Dy^{3+} and B^{3+}. *Chemistry of Materials*, 17(15):3904–3912, 2005.

[88] G. Inan Akmehmet, S. Šturm, L. Bocher, M. Kociak, B. Ambrožič, and C. W. Ow-Yang. Structure and Luminescence in Long Persistence Eu, Dy, and B Codoped Strontium Aluminate Phosphors: The Boron Effect. *Journal of the American Ceramic Society*, 99(6):2175–2180, 2016.

[89] T. Delgado, J. Afshani, and H. Hagemann. Spectroscopic Study of a Single Crystal of $SrAl_2O_4$:Eu^{2+}, Dy^{3+}. *The Journal of Physical Chemistry C*, 123(14):8607–8613, 2019.

[90] D. Van der Heggen, J. J. Joos, and P. F. Smet. Importance of Evaluating the Intensity Dependency of the Quantum Efficiency: Impact on LEDs and Persistent Phosphors. *ACS Photonics*, 5(11):4529–4537, 2018.

[91] T. Hoshina. 5d→4f Radiative Transition-Probabilities of Ce^{3+} and Eu^{2+} in Crystals. *Journal of the Physical Society of Japan*, 48(4):1261–1268, 1980.

[92] S. H. M. Poort, A. Meyerink, and G. Blasse. Lifetime measurements in Eu^{2+}-doped host lattices. *Journal of Physics and Chemistry of Solids*, 58(9):1451–1456, 1997.

[93] J. J. Joos, P. F. Smet, L. Seijo, and Z. Barandiarán. Insights into the Complexity of the Excited States of Eu-Doped Luminescent Materials. *Inorganic Chemistry Frontiers*, 2020.

[94] E. Nakazawa, Y. Murazaki, and S. Saito. Mechanism of the persistent phosphorescence in $Sr_4Al_{14}O_{25}$:Eu and $SrAl_2O_4$:Eu codoped with rare earth ions. *Journal of Applied Physics*, 100(11):113113, 2006.

[95] E. Nakazawa and T. Mochida. Traps in $SrAl_2O_4$:Eu^{2+} phosphors with rare-earth ion doping. *Journal of Luminescence*, 72-74:236–237, 1997.

[96] T. Katsumata, S. Toyomane, R. Sakai, S. Komuro, and T. Morikawa. Trap Levels in Eu-Doped $SrAl_2O_4$:Eu Phosphor Crystals Co-Doped with Rare-Earth Elements. *Journal of the American Ceramic Society*, 89(3):932–936, 2006.

[97] M. Ohta and M. Takami. Influence of Codoping Rare-Earth Ion on Lasting Phenomena of Eu-Doped Strontium Aluminate Phosphor. *Journal of The Electrochemical Society*, 151(3):G171–G174, 2004.

[98] T. Katsumata, T. Nabae, K. Sasajima, S. Komuro, and T. Morikawa. Effects of Composition on the Long Phosphorescent $SrAl_2O_4$:Eu^{2+}, Dy^{3+} Phosphor Crystals. *Journal of The Electrochemical Society*, 144(9):L243–L245, 1997.

[99] T. Nakamura, K. Kaiya, N. Takahashi, T. Matsuzawa, M. Ohta, C. C. Rowlands, G. M. Smithe, and P. C. Riedie. High frequency EPR investigations of gadolinium(III)-doped strontium aluminates. *Physical Chemistry Chemical Physics*, 3:1721–1723, 2001.

[100] T. Delgado, S. Ajoubipour, J. Afshani, S. Yoon, B. Walfort, and H. Hagemann. Spectroscopic properties of Dy^{3+} and Dy^{3+}, B^{3+}-doped $SrAl_2O_4$. *Optical Materials*, 89:268–275, 2019.

[101] D. D. Jia. Relocalization of Ce^{3+} 5d electrons from host conduction band. *Journal of Luminescence*, 117(2):170–178, 2006.

[102] P. J. Saines and B. J. Kennedy. Implications of the solubility of trivalent lanthanides in AAl_2O_4(A =Ca, Sr, and Ba) for their role in phosphors. *Powder Diffraction*, 21(4):285–288, 2006.

[103] P. F. Smet, K. Van den Eeckhout, O. De Clercq, and D. Poelman. Persistent phosphors. In J.-C. Bünzli and V. K. Pecharsky, editors, *Handbook on the physics and chemistry of rare earths, including actinides*, volume 48, pages 1–108. Elsevier, 2015.

[104] J. Hölsä, T. Laamanen, M. Lastusaari, M. Malkamäki, E. Welter, and D. A. Zajac. Valence and environment of rare earth ions in $CaAl_2O_4$:Eu^{2+},R^{3+} persistent luminescence materials. *Spectrochimica Acta - Part B Atomic Spectroscopy*, 65(4):301–305, 2010.

[105] A. B. Munoz-Garcia and L. Seijo. Ce and la single- and double-substitutional defects in yttrium aluminum garnet: First-principles study. *Journal of Physical Chemistry A*, 115(5):815–823, 2011.

[106] A. B. Munoz-Garcia, Z. Barandiaran, and L. Seijo. Antisite defects in ce-doped yag ($y_3al_5o_12$): first-principles study on structures and 4f-5d transitions. *Journal of Materials Chemistry*, 22(37):19888–19897, 2012.

[107] A. De Vos, K. Lejaeghere, D. E. P. Vanpoucke, J. J. Joos, P. F. Smet, and K. Hemelsoet. First-Principles Study of Antisite Defect Configurations in $ZnGa_2O_4$:Cr Persistent Phosphors. *Inorganic Chemistry*, 55(5):2402–2412, 2016.

[108] W. Jia, H. Yuan, L. Lu, H. Liu, and W. M. Yen. Phosphorescent dynamics in $SrAl_2O_4$:Eu^{2+},Dy^{3+} single crystal fibers. *Journal of Luminescence*, 76-77(97):424–428, 1998.

[109] A. Dulda, D. Jo, W. Park, T. Masaki, and D. Yoon. Photoluminescence and morphology of flux grown BAM phosphor using a novel synthesis method. *Journal of Ceramic Processing Research*, 10(6):811–816, 2009.

[110] D. Haranath, P. Sharma, H. Chander, A. Ali, N. Bhalla, and S. Halder. Role of boric acid in synthesis and tailoring the properties of calcium aluminate phosphor. *Materials Chemistry and Physics*, 101(1):163–169, 2007.

[111] Q. Wu, N. Zhang, Q. Yang, and H. Jiao. Effect of H_3BO_3 as flux on the properties of Zn_2SiO_4:Mn green phosphor. *Journal of the Chinese Ceramic Society*, 36(11):1660–1663, 2008.

[112] P. Liu, J. Yin, X. Mi, L. Zhang, and L. Bie. Enhanced photoluminescence of $CaTiO_3$:Eu^{3+} red phosphors prepared by H_3BO_3 assisted solid state synthesis. *Journal of Rare Earths*, 31(6):555–558, 2013.

[113] Y. H. Cho, R. B. V. Chalapathy, D. H. Park, and B. T. Ahn. Low Temperature Synthesis of Eu-Doped Cubic Phase $BaAl_2S_4$ Blue Phosphor Using H_3BO_3 or B_2O_3 Flux. *Journal of The Electrochemical Society*, 157(3):J45–J49, 2010.

[114] A. Strel'tsov, G. Torgashov, N. Sinitsyn, I. Torgashov, Y. Gulyaev, V. Dmitrienko, and A. Dmitrienko. Phase Composition and Luminescent Characteristics of Y_2O_3:Eu and Y_2O_2S:Eu Crystals Obtained using Borate Flux. In *2006 IEEE International Vacuum Electronics Conference held Jointly with 2006 IEEE International Vacuum Electron Sources*, pages 397–398, 2006.

[115] J. Niittykoski, T. Aitasalo, J. Hölsä, H. Jungner, M. Lastusaari, M. Parkkinen, and M. Tukia. Effect of boron substitution on the preparation and luminescence of Eu^{2+} doped strontium aluminates. *Journal of Alloys and Compounds*, 374:108–111, 2004.

[116] D. Wang, Q. Yin, Y. Li, and M. Wang. Influence of B_2O_3 on Matrix Forming Process and Luminescent Properties of $SrO.Al_2O_3$:Eu^{3+} Phosphor. *Journal of The Electrochemical Society*, 149(3):H65–H67, 2002.

[117] I.-C. Chen and T.-M. Chen. Sol-gel synthesis and the effect of boron addition on the phosphorescent properties of $SrAl_2O_4$:Eu^{2+},Dy^{3+} phosphors. *Journal of Materials Research*, 16(3):644–651, 2001.

[118] A. Nag and T. R. Kutty. The mechanism of long phosphorescence of $SrAl_{2-x}B_xO_4$ (0 ¡ x ¡ 0.2) and $Sr_4Al_{14-x}B_xO_{25}$ (0.1 ¡ x ¡ 0.4) co-doped with Eu^{2+} and Dy^{3+}. *Materials Research Bulletin*, 39(3):331–342, 2004.

[119] T.-P. Tang, C.-M. Lee, and F.-C. Yen. The photoluminescence of $SrAl_2O_4$:Sm phosphors. *Ceramics International*, 32(6):665–671, 2006.

[120] S. Yoon, J. Bierwagen, M. Trottmann, B. Walfort, N. Gartmann, A. Weidenkaff, H. Hagemann, and S. Pokrant. The influence of boric acid on improved persistent luminescence and thermal oxidation resistance of $SrAl_2O_4$:Eu^{2+}. *Journal of Luminescence*, 167:126–131, 2015.

[121] J. Chen, F. Gu, and C. Li. Influence of Precalcination and Boron-Doping on the Initial Photoluminescent Properties of $SrAl_2O_4$:Eu,Dy Phosphors. *Crystal Growth & Design*, 8(9):3175–3179, 2008.

[122] H. Shin, S. Ullah, and K. Chung. Effect of nominal substitution of Dy^{3+} for host cations in $SrAl_2O_4$:Eu^{2+} phosphor on phase evolution and long afterglow luminescence. *Journal of Alloys and Compounds*, 544:181–187, 2012.

[123] A. Meijerink, J. Nuyten, and G. Blasse. Luminescence and Energy Migration in (Sr,Eu)B_4O_7, a System with a $4f^7 - 4f^6 5d$ Crossover in the Excited-State. *Journal of Luminescence*, 44(1-2):19–31, 1989.

[124] G. Blasse, G. J. Dirksen, and A. Meijerink. The Luminescence of Ytterbium(II) in Strontium Tetraborate. *Chemical Physics Letters*, 167(1-2):41–44, 1990.

[125] P. Mikhail, J. Hulliger, M. Schnieper, and H. Bill. SrB_4O_7:Sm^{2+}: Crystal Chemistry, Czochralski Growth and Optical Hole Burning. *Journal of Materials Chemistry*, 10(4):987–991, 2000.

[126] W. J. Schipper, A. Meijerink, and G. Blasse. The Luminescence of Tm^{2+} in Strontium Tetraborate. *Journal of Luminescence*, 62(2):55–59, 1994.

[127] G. Blasse, A. Meijerink, M. Nomes, and J. Zuidema. Unusual Bismuth Luminescence in Strontium Tetraborate (SrB_4O_7:Bi). *Journal of Physics and Chemistry of Solids*, 55(2):171–174, 1994.

[128] W. Xu and J. R. Peterson. Stabilization of Divalent Neodymium (Nd^{2+}) in Strontium Tetraborate. *Journal of Alloys and Compounds*, 249(1):213–216, 1997.

[129] M. de Jong, A. Meijerink, R. A. Gordon, Z. Barandiarán, and L. Seijo. Is Bi^{2+} Responsible for the Red-Orange Emission of Bismuth-Doped SrB_4O_7? *Journal of Physical Chemistry C*, 118(18):9696–9705, 2014.

[130] M. Suta, F. Lavoie-Cardinal, and C. Wickleder. Underestimated Color Centers: Defects as Useful Reducing Agents in Lanthanide-Activated Luminescent Materials. *Angewandte Chemie, International Edition*, 59(27):10949–10954, 2020.

[131] J. J. Joos, L. Seijo, and Z. Barandiarán. Direct Evidence of Intervalence Charge-Transfer States of Eu-Doped Luminescent Materials. *The Journal of Physical Chemistry Letters*, 10(7):1581–1586, 2019.

[132] M. Suta and C. Wickleder. Synthesis, Spectroscopic Properties and Applications of Divalent Lanthanides Apart from Eu^{2+}. *Journal of Luminescence*, 210:210–238, 2019.

[133] J. Geng and Z. Wu. Synthesis of Long Afterglow $SrAl_2O_4$:Eu^{2+}, Dy^{3+} Phosphors through Microwave Route. *Journal of Materials Synthesis and Processing*, 10(5):245–248, 2002.

[134] T. Ishigaki, H. Mizushina, K. Uematsu, N. Matsushita, M. Yoshimura, K. Toda, and M. Sato. Microwave synthesis technique for long phosphorescence phosphor $SrAl_2O_4$:Eu^{2+}, Dy^{3+} using carbon reduction. *Materials Science and Engineering B*, 173:109–112, 2010.

[135] J. M. Carvalho, D. Van der Heggen, L. I. D. J. Martin, and P. F. Smet. Microwave-assisted synthesis followed by a reduction step: making persistent phosphors with a large storage capacity. *Dalton Transactions*, 49:4518–4527, 2020.

[136] C. Guo, L. Luan, D. Huang, Q. Su, and Y. Lv. Study on the stability of phosphor $SrAl_2O_4$:Eu^{2+}, Dy^{3+} in water and method to improve its moisture resistance. *Materials Chemistry and Physics*, 106(2-3):268–272, 2007.

[137] E. Karacaoglu, E. Öztürk, M. Uyaner, and M. D. Losego. Atomic layer deposition (ALD) of nanoscale coatings on $SrAl_2O_4$-based phosphor powders to prevent aqueous degradation. *Journal of the American Ceramic Society*, 2020.

[138] H. Terraschke and C. Wickleder. UV, Blue, Green, Yellow, Red, and Small: Newest Developments on Eu^{2+}-Doped Nanophosphors. *Chemical Reviews*, 115(20):11352–11378, 2015.

[139] X. Yu, C. Zhou, X. He, Z. Peng, and S. P. Yang. The influence of some processing conditions on luminescence of $SrAl_2O_4$:Eu^{2+} nanoparticles produced by combustion method. *Materials Letters*, 58(6):1087–1091, 2004.

[140] T. Peng, H. Yang, X. Pu, B. Hu, Z. Jiang, and C. Yan. Combustion synthesis and photoluminescence of $SrAl_2O_4$:Eu, Dy phosphor nanoparticles. *Materials Letters*, 58(3-4):352–356, 2004.

[141] R. Zhang, G. Han, L. Zhang, and B. Yang. Gel combustion synthesis and luminescence properties of nanoparticles of monoclinic $SrAl_2O_4$:Eu^{2+}, Dy^{3+}. *Materials Chemistry and Physics*, 113(1):255–259, 2009.

[142] R. Ianos, R. Istratie, C. Pacurariu, and R. Lazau. Solution combustion synthesis of strontium aluminate, $SrAl_2O_4$, powders: Single-fuel versus fuel-mixture approach. *Physical Chemistry Chemical Physics*, 18(2):1150–1157, 2015.

[143] E. Finley, A. S. Paterson, A. Cobb, R. C. Willson, and J. Brgoch. Reducing particle size of persistent luminescent $SrAl_2O_4$:Eu^{2+},Dy^{3+} via microwave-assisted, reverse micelle synthesis. *Optical Materials Express*, 7(7):2597, 2017.

[144] Q. Xiao, L. Xiao, Y. Liu, X. Chen, and Y. Li. Synthesis and luminescence properties of needle-like $SrAl_2O_4$:Eu, Dy phosphor via a hydrothermal co-precipitation method. *Journal of Physics and Chemistry of Solids*, 71(7):1026–1030, 2010.

[145] R. E. Rojas-Hernandez, F. Rubio-Marcos, R. H. Gonçalves, M. Á. Rodriguez, E. Véron, M. Allix, C. Bessada, and J. F. Fernandez. Original Synthetic Route To Obtain a $SrAl_2O_4$ Phosphor by the Molten Salt Method: Insights into the Reaction Mechanism and Enhancement of the Persistent Luminescence. *Inorganic Chemistry*, 54(20):9896–9907, 2015.

[146] T. Peng, L. Huajun, H. Yang, and C. Yan. Synthesis of $SrAl_2O_4$:Eu, Dy phosphor nanometer powders by sol-gel processes and its optical properties. *Materials Chemistry and Physics*, 85(1):68–72, 2004.

[147] R. Aroz, V. Lennikov, R. Cases, M. L. Sanjuán, G. F. de la Fuente, and E. Muñoz. Laser synthesis and luminescence properties of $SrAl_2O_4$:Eu^{2+},Dy^{3+} phosphors. *Journal of the European Ceramic Society*, 32(16):4363–4369, 2012.

[148] C. Zollfrank, S. Gruber, M. Batentschuk, A. Osvet, F. Goetz-Neunhoeffer, S. Dittrich, J. Grabow, H. D. Kurland, and F. A. Müller. Synthesis of Eu-doped $SrAl_2O_4$ nanophosphors by CO_2 laser vaporization. *Acta Materialia*, 61(19):7133–7141, 2013.

[149] S. K. Kandpal, B. Goundie, J. Wright, R. A. Pollock, M. D. Mason, and R. W. Meulenberg. Investigation of the Emission Mechanism in Milled $SrAl_2O_4$:Eu,Dy Using Optical and Synchrotron X-ray Spectroscopy. *ACS Applied Materials & Interfaces*, 3(9):3482–3486, 2011.

[150] R. E. Rojas-Hernandez, F. Rubio-Marcos, E. Enríquez, M. A. De La Rubia, and J. F. Fernandez. A low-energy milling approach to reduce particle size maintains the luminescence of strontium aluminates. *RSC Advances*, 5(53):42559–42567, 2015.

[151] V. Havasi, D. Tátrai, G. Szabó, E. Varga, A. Erdohelyi, G. Sipos, Z. Kónya, and Á. Kukovecz. On the effects of milling and thermal regeneration on the luminescence properties of Eu^{2+} and Dy^{3+} doped strontium aluminate phosphors. *Journal of Luminescence*, 219:116917, 2020.

[152] V. Abbruscato. Optical and Electrical Properties of $SrAl_2O_4$:Eu^{2+}. *Journal of The Electrochemical Society*, 118(6):930–933, 1971.

[153] A. J. J. Bos, P. Dorenbos, A. Bessière, A. Lecointre, M. Bedu, M. Bettinelli, and F. Piccinelli. Study of TL glow curves of YPO_4 double doped with lanthanide ions. *Radiation Measurements*, 46(12):1410–1416, 2011.

[154] A. J. J. Bos. Theory of thermoluminescence. *Radiation Measurements*, 41:S45–S56, 2007.

[155] J. T. Randall and M. H. F. Wilkins. Phopshorescence and Electron Traps: I The Study of Trap Distributions. *Proceedings of the Royal Society*, A84:366–389, 1945.

[156] J. T. Randall and M. H. F. Wilkins. Phosphorescence and electron traps ii. the interpretation of long-period phosphorescence. *Proceedings of the Royal Society of London. Series A. Mathematical and Physical Sciences*, 184(999):390–407, 1945.

[157] A. F. Garlick, G. F. J.; Gibson. The electron trap mechanism of luminescence in sulphide and silicate phosphors. *Proceedings of the Physical Society*, 60:574, 1948.

[158] C. E. May and J. A. Partridge. Thermoluminescent kinetics of alpha-irradiated alkali halides. *The Journal of Chemical Physics*, 40(5):1401–1409, 1964.

[159] K. Van den Eeckhout, A. J. J. Bos, D. Poelman, and P. F. Smet. Revealing trap depth distributions in persistent phosphors. *Physical Review B*, 87(4):045126, 2013.

[160] S. E. Michels, M. Kersemans, M. Versluis, G. Lajoinie, and P. F. Smet. Fast and High-Resolution Ultrasound Pressure Field Mapping Using Luminescent Membranes. *Advanced Optical Materials*, 9(12):2100085, 2021.

[161] S. E. Michels, G. Lajoinie, S. Hedayatrasa, M. Versluis, M. Kersemans, and P. F. Smet. A theoretical framework for acoustically produced luminescence: From thermometry to ultrasound pressure field mapping. *Journal of Luminescence*, 248:118940, 2022.

[162] E. G. Yukihara, A. J. J. Bos, P. Bilski, and S. W. S. McKeever. The quest for new thermoluminescence and optically stimulated luminescence materials: Needs, strategies and pitfalls. *Radiation Measurements*, 158:106846, 2022.

[163] A. Feng, J. J. Joos, J. R. Du, and P. F. Smet. Revealing trap depth distributions in persistent phosphors with a thermal barrier for charging. *Physical Review B*, 105(20), 2022.

[164] R. Chen and S. W. S. McKeever. *Theory of Thermoluminescence and Related Phenomena*. World Scientific, 1997.

[165] W. Hoogenstraaten and H. A. Klasens. Some Properties of Zinc Sulfide Activated with Copper and Cobalt. *Journal of the Electrochemical Society*, 100(8):366–375, 1953.

[166] W. Hoogenstraaten. Electron traps in zinc sulphide phosphors. *Philips Research Report*, 13:515–693, 1958.

[167] O. Q. De Clercq, J. Du, P. F. Smet, J. J. Joos, and D. Poelman. Predicting the afterglow duration in persistent phosphors: A validated approach to derive trap depth distributions. *Physical Chemistry Chemical Physics*, 20(48):30455–30465, 2018.

[168] G. Kitis and J. M. Gomez-Ros. Thermoluminescence glow-curve deconvolution functions for mixed order of kinetics and continuous trap distribution. *Nuclear Instruments and Methods in Physics Research Section A: Accelerators, Spectrometers, Detectors and Associated Equipment*, 440(1):224–231, 2000.

[169] G. Rudlof, J. Becherer, and H. Glaefeke. Behaviour of the fractional glow technique with first-order detrapping processes, traps distributed in energy or frequency factor. *physica status solidi (a)*, 49(2):K121–K124, 1978.

[170] W. F. Hornyak and R. Chen. Thermoluminescence and phosphorescence with a continuous distribution of activation energies. *Journal of Luminescence*, 44(1-2):73–81, 1989.

[171] J. Du, O. Q. De Clercq, and D. Poelman. Temperature dependent persistent luminescence: Evaluating the optimum working temperature. *Scientific Reports*, 9:10517, 2019.

[172] F. Clabau, X. Rocquefelte, S. Jobic, P. Deniard, M.-H. Whangbo, A. Garcia, and T. Le Mercier. On the phosphorescence mechanism in $SrAl_2O_4$:Eu^{2+} and its codoped derivatives. *Solid State Sciences*, 9(7):608–612, 2007.

[173] J. Bierwagen, T. Delgado, G. Jiranek, S. Yoon, N. Gartmann, B. Walfort, M. Pollnau, and H. Hagemann. Probing traps in the persistent phosphor $SrAl_2O_4$:Eu^{2+},Dy^{3+},B^{3+} - A wavelength, temperature and sample dependent thermoluminescence investigation. *Journal of Luminescence*, 222:117113, 2020.

[174] T. Aitasalo, J. Hölsä, H. Jungner, J. C. Krupa, M. Lastusaari, J. Legendziewicz, and J. Niittykoski. Effect of temperature on the luminescence processes of $SrAl_2O_4$:Eu^{2+}. *Radiation Measurements*, 38(4-6):727–730, 2004.

[175] I. Tsutai, T. Kamimura, K. Kato, F. Kaneko, K. Shinbo, M. Ohta, and T. Kawakami. Preparation of Sputtered $SrAl_2O_4$:Eu Films and Thermoluminescence Properties. *IEEJ Transactions on Fundamentals and Materials*, 132(1):1015–1020, 2000.

[176] K. Kato, Y. Ogura, M. Sengiku, K. Shinbo, F. Kaneko, Y. Oda, and Y. Kiyoshi. Luminescent Properties of $SrAl_2O_4$:Eu Thin Films Deposited by Intense Pulsed Ion-Beam Evaporation. *Japanese Journal of Applied Physics*, 40(2B):1038–1041, 2001.

[177] H. Hagemann, D. Lovy, S. Yoon, S. Pokrant, N. Gartmann, B. Walfort, and J. Bierwagen. Wavelength dependent loading of traps in the persistent phosphor $SrAl_2O_4$:Eu^{2+}, Dy^{3+}. *Journal of Luminescence*, 170:299–304, 2016.

[178] P. Zeng, X. Wei, M. Yin, and Y. Chen. Investigation of the long afterglow mechanism in $SrAl_2O_4$:Eu^{2+}/Dy^{3+} by optically stimulated luminescence and thermoluminescence. *Journal of Luminescence*, 199(11):400–406, 2018.

[179] H. Liu, B. Feng, L. Luo, C. Han, and P. A. Tanner. Near infrared photostimulated persistent luminescence and information storage of $SrAl_2O_4$:Eu^{2+},Dy^{3+} phosphor. *Optical Materials Express*, 6(11):3375, 2016.

[180] M. L. Chithambo, A. H. Wako, and A. A. Finch. Thermoluminescence of $SrAl_2O_4$:Eu^{2+}, Dy^{3+}: Kinetic analysis of a composite-peak. *Radiation Measurements*, 97:1–13, 2017.

[181] V. Chernov, P. Salas-Castillo, L. A. Díaz-Torres, N. J. Zúñiga-Rivera, R. Ruiz-Torres, R. Meléndrez, and M. Barboza-Flores. Thermoluminescence and infrared stimulated luminescence in long persistent monoclinic $SrAl_2O_4$:Eu^{2+}, Dy^{3+} and $SrAl_2O_4$:Eu^{2+}, Nd^{3+} phosphors. *Optical Materials*, 92:46–52, 2019.

[182] D. Van der Heggen, D. Vandenberghe, N. K. Moayed, J. D. Grave, P. F. Smet, and J. J. Joos. The almost hidden role of deep traps when measuring afterglow and thermoluminescence of persistent phosphors. *Journal of Luminescence*, 226:117496, 2020.

[183] C. Tydtgat, K. W. Meert, D. Poelman, and P. F. Smet. Optically stimulated detrapping during charging of persistent phosphors. *Optical Materials Express*, 6(3):844, 2016.

[184] N. Zúñiga-Rivera, R. García, R. Rodríguez-Mijangos, V. Chernov, R. Meléndrez, M. Pedroza-Montero, and M. Barboza-Flores. Persistent luminescence, TL and OSL characterization of beta irradiated $SrAl_2O_4$:Eu^{2+}, Dy^{3+} combustion synthesized phosphor. *Nuclear Instruments and Methods in Physics Research Section B: Beam Interactions with Materials and Atoms*, 326:99–102, 2014.

[185] W. Jia, H. Yuan, S. Holmstrom, H. Liu, and W. M. Yen. Photo-stimulated luminescence in $SrAl_2O_4$:Eu^{2+},Dy^{3+} single crystal fibers. *Journal of Luminescence*, 83-84:465–469, 1999.

[186] F. Pellé, T. Aitasalo, M. Lastusaari, J. Niittykoski, and J. Hölsä. Optically stimulated luminescence of persistent luminescence materials. *Journal of Luminescence*, 119-120(Fifteenth International Conference on Dynamical Processes in Excited States of Solids):64–68, 2006.

[187] F. Liu, W. Yan, Y. J. Chuang, Z. Zhen, J. Xie, and Z. Pan. Photostimulated near-infrared persistent luminescence as a new optical read-out from Cr^{3+}-doped $LiGa_5O_8$. *Scientific Reports*, 3:1554, 2013.

[188] S. K. Sharma, D. Gourier, E. Teston, D. Scherman, C. Richard, and B. Viana. Persistent luminescence induced by near infra-red photostimulation in chromium-doped zinc gallate for in-vivo optical imaging. *Optical Materials*, 63:51–58, 2017.

[189] J. Xu, D. Murata, J. Ueda, B. Viana, and S. Tanabe. Toward Rechargeable Persistent Luminescence for the First and Third Biological Windows via Persistent Energy Transfer and Electron Trap Redistribution. *Inorganic Chemistry*, 57(9):5194–5203, 2018.

[190] A. J. Walton. Triboluminescence. *Advances in Physics*, 26(6):887–948, 1977.

[191] J.-C. G. Bünzli and K.-L. Wong. Lanthanide mechanoluminescence. *Journal of Rare Earths*, 36(1):1–41, 2018.

[192] A. Feng and P. F. Smet. A Review of Mechanoluminescence in Inorganic Solids: Compounds, Mechanisms, Models and Applications. *Materials*, 11(4):484, 2018.

[193] J.-C. Zhang, X. Wang, G. Marriott, and C.-N. Xu. Trap-controlled mechanoluminescent materials. *Progress in Materials Science*, 103:678–742, 2019.

[194] B. Chen, X. Zhang, and F. Wang. Expanding the Toolbox of Inorganic Mechanoluminescence Materials. *Accounts of Materials Research*, 2(5):364–373, 2021.

[195] Y. Zhuang and R.-J. Xie. Mechanoluminescence Rebrightening the Prospects of Stress Sensing: A Review. *Advanced Materials*, 33(50):2005925, 2021.

[196] Y. Zhuang, D. Tu, C. Chen, L. Wang, H. Zhang, H. Xue, C. Yuan, G. Chen, C. Pan, L. Dai, and R.-J. Xie. Force-induced charge carrier storage: a new route for stress recording. *Light: Science & Applications*, 9(1):182, 2020.

[197] N. Wang, M. Pu, Z. Ma, Y. Feng, Y. Guo, W. Guo, Y. Zheng, L. Zhang, Z. Wang, M. Feng, X. Li, and D. Wang. Control of triboelectricity by mechanoluminescence in ZnS/Mn-containing polymer films. *Nano Energy*, 90:106646, 2021.

[198] W. Wang, Z. Wang, J. Zhang, J. Zhou, W. Dong, and Y. Wang. Contact electrification induced mechanoluminescence. *Nano Energy*, 94:106920, 2022.

[199] R. R. Petit, S. E. Michels, A. Feng, and P. F. Smet. Adding memory to pressure-sensitive phosphors. *Light: Science and Applications*, 8(1):124, 2019.

[200] C.-N. Xu, T. Watanabe, M. Akiyama, and X.-G. Zheng. Direct view of stress distribution in solid by mechanoluminescence. *Applied Physics Letters*, 74(17):2414–2416, 1999.

[201] C.-N. Xu, X.-G. Zheng, M. Akiyama, K. Nonaka, and T. Watanabe. Dynamic visualization of stress distribution by mechanoluminescence image. *Applied Physics Letters*, 76(2):179–181, 2000.

[202] C.-N. Xu, H. Yamada, X. Wang, and X.-G. Zheng. Strong elasticoluminescence from monoclinic-structure $SrAl_2O_4$. *Applied Physics Letters*, 84(16):3040–3042, 2004.

[203] J. Kim, Y. Kwon, N. Shin, and K. Sohn. Visualization of fractures in alumina ceramics by mechanoluminescence. *Acta Materialia*, 53(16):4337–4343, 2005.

[204] J. S. Kim, Y.-N. Kwon, N. Shin, and K.-S. Sohn. Mechanoluminescent $SrAl_2O_4$:Eu^{2+},Dy^{3+} phosphor for use in visualization of quasidynamic crack propagation. *Applied Physics Letters*, 90(24):241916, 2007.

[205] X. Fu, H. Yamada, and C.-N. Xu. Property of Highly Oriented $SrAl_2O_4$:Eu^{2+} Film on Quartz Glass Substrates and Its Potential Application in Stress Sensor. *Journal of The Electrochemical Society*, 156(9):J249, 2009.

[206] H. Zhang, H. Yamada, N. Terasaki, and C.-N. Xu. Ultraviolet mechanoluminescence from $SrAl_2O_4$:Ce and $SrAl_2O_4$:Ce,Ho. *Applied Physics Letters*, 91(8):081905, 2007.

[207] Y. Terasawa, C. N. Xu, H. Yamada, and M. Kubo. Near Infra-Red Mechanoluminescence from Strontium Aluminate Doped with Rare-Earth Ions. *IOP Conference Series: Materials Science and Engineering*, 18(21):212013, 2011.

[208] Y. Fujio, C.-N. Xu, and N. Terasaki. Synthesis of Near-Infrared Mechanoluminescence Material Via Organic Acid-Aided Process. *ECS Transactions*, 98(11):61, 2020.

[209] D. Tu, C.-N. Xu, R. Saito, L. Liu, and A. Yoshida. Influence of H_3BO_3 addition on mechanoluminescence property of $SrAl_2O_4$:Eu^{2+}. *J. Ceram. Soc. Japan*, 125(8):648–651, 2017.

[210] S.-N. Xu and D. Tu, US Patent, US11225603B2, Jan 18, 2022.

[211] L. Liu, C. N. Xu, A. Yoshida, D. Tu, N. Ueno, and S. Kainuma. Scalable Elasticoluminescent Strain Sensor for Precise Dynamic Stress Imaging and Onsite Infrastructure Diagnosis. *Advanced Materials Technologies*, 4(1):1800336, 2019.

[212] T. Zhan, C.-N. Xu, H. Yamada, Y. Terasawa, L. Zhang, H. Iwase, and M. Kawai. Enhancement of afterglow in $SrAl_2O_4$:Eu^{2+} long-lasting phosphor with swift heavy ion irradiation. *RSC Advances*, 2(1):328–332, 2011.

[213] T. Z. Zhan, C. N. Xu, H. Yamada, Y. Terasawa, L. Zhang, H. Iwase, and M. Kawai. Enhancement of impact-induced mechanoluminescence by swift heavy ion irradiation. *Applied Physics Letters*, 100(1):014101, 2012.

[214] X. Qian, Z. Cai, M. Su, F. Li, W. Fang, Y. Li, X. Zhou, Q. Li, X. Feng, W. Li, X. Hu, X. Wang, C. Pan, and Y. Song. Printable Skin-Driven Mechanoluminescence Devices via Nanodoped Matrix Modification. *Advanced Materials*, 30(25):1800291, 2018.

[215] S. Ishida and A. Narahara. Stress-rate effect on time response of mechanoluminescent-sensor luminescent intensity. *Optics Express*, 27(4):3935–3943, 2019.

[216] D. A. Ilatovskii, N. A. Tyutkov, V. V. Vinogradov, and A. V. Vinogradov. Stimuli-Responsive Mechanoluminescence in Different Matrices. *ACS Omega*, 3(12):18803–18810, 2018.

[217] T. W. Kerekes, H. You, T. Hemmatian, J. Kim, and G. J. Yun. Enhancement of mechanoluminescence sensitivity of $SrAl_2O_4$:Eu^{2+},Dy^{3+} /Epoxy composites by ultrasonic curing treatment method. *Composite Interfaces*, 28(1):77–99, 2021.

[218] S. Timilsina, K. H. Lee, I. Y. Jang, and J. S. Kim. Mechanoluminescent determination of the mode I stress intensity factor in $SrAl_2O_4$:Eu^{2+},Dy^{3+}. *Acta Materialia*, 61(19):7197–7206, 2013.

[219] M. Dubernet, E. Bruyer, Y. Gueguen, P. Houizot, J. C. Hameline, X. Rocquefelte, and T. Rouxel. Mechanics and physics of a glass/particles photonic sponge. *Scientific Reports*, 10(1):19495, 2020.

[220] M. R. Rahimi, G. J. Yun, and J.-S. Choi. A predictive mechanoluminescence transduction model for thin-film $SrAl_2O_4$:Eu^{2+},Dy^{3+} (SAOED) stress sensor. *Acta Materialia*, 77:200–211, 9 2014.

[221] A. I. Azad, M. R. Rahimi, and G. J. Yun. Quantitative full-field strain measurements by SAOED ($SrAl_2O_4$:Eu^{2+},Dy^{3+}) mechanoluminescent materials. *Smart Materials and Structures*, 25(9):095032, 2016.

[222] C. Li, C.-N. Xu, Y. Adachi, and N. Ueno. Real-time detection of axial force for reliable tightening control. volume 7522, pages 989–994. Fourth International Conference on Experimental Mechanics, SPIE, 2010.

[223] M. Dubernet, Y. Gueguen, P. Houizot, F. Célarié, J.-C. Sangleboeuf, H. Orain, and T. Rouxel. Evidence and modeling of mechanoluminescence in a transparent glass particulate composite. *Applied Physics Letters*, 107(15):151906, 2015.

[224] J.-C. Zhang, M. Tang, X. Wang, Y. Li, and X. Yao. Elastico-mechanoluminescence properties of Pr^{3+}-doped $BaTiO_3$–$CaTiO_3$ diphase ceramics with water resistance behavior. *Ceramics International*, 38:S581–S584, 2012.

[225] J. Botterman, d. K. V. Eeckhout, I. D. Baere, D. Poelman, and P. F. Smet. Mechanoluminescence in $BaSi_2O_2N_2$:Eu. *Acta Materialia*, 60(15):5494–5500, 2012.

[226] A. Feng, S. Michels, A. Lamberti, W. Van Paepegem, and P. F. Smet. Relating structural phase transitions to mechanoluminescence: The case of the $Ca_{1-x}Sr_xAl_2Si_2O_8$:1% Eu^{2+}, 1% Pr^{3+} anorthite. *Acta Materialia*, 183:493–503, 2020.

[227] M. Akiyama, C.-N. Xu, Y. Liu, K. Nonaka, and T. Watanabe. Influence of Eu, Dy co-doped strontium aluminate composition on mechanoluminescence intensity. *Journal of Luminescence*, 97(1):13–18, 2002.

[228] K.-S. Sohn, W. B. Park, S. Timilsina, and J. S. Kim. Mechanoluminescence of $SrAl_2O_4$:Eu^{2+},Dy^{3+} under cyclic loading. *Optics Letters*, 39(6):1410–1413, 2014.

[229] K.-S. Sohn, M. Y. Cho, M. Kim, and J. S. Kim. A smart load-sensing system using standardized mechano-luminescence measurement. *Optics Express*, 23(5):6073–6082, 2015.

[230] H. Yamada, H. Kusaba, and C.-N. Xu. Anisotropic lattice behavior in elasticoluminescent material $SrAl_2O_4$:Eu^{2+}. *Applied Physics Letters*, 92(10):101909, 2008.

[231] H. Matsuo, K. Ikeda, S. Hata, H. Nakashima, H. Yamada, and C. Xu. Phase transformation behavior and pseudoelastic deformation in $SrAl_2O_4$. *Journal of Alloys and Compounds*, 577:S507–S516, 2013.

[232] J. R. N. Gnidakouong and G. J. Yun. Dislocation density level induced divergence between stress-free afterglow and mechanoluminescence in $SrAl_2O_4$:Eu^{2+},Dy^{3+}. *Ceramics International*, 45(2):1794–1802, 2019.

[233] H. Hara, C. N. Xu, R. Wang, X. G. Zheng, M. Nishibori, and E. Nishibori. Control of crystal structure and performance evaluation of multi-piezo material of $Li_{1-x}Na_xNbO_3:Pr^{3+}$. *Journal of the Ceramic Society of Japan*, 128(8):518–522, 2020.

[234] B. P. Chandra, V. K. Chandra, and P. Jha. Microscopic theory of elastico-mechanoluminescent smart materials. *Applied Physics Letters*, 104(3):031102, 2014.

[235] B. Chandra, V. Chandra, and P. Jha. Piezoelectrically-induced trap-depth reduction model of elastico-mechanoluminescent materials. *Physica B: Condensed Matter*, 461:38–48, 2015.

[236] J. S. Kim, K. Kibble, Y. N. Kwon, and K.-S. Sohn. Rate-equation model for the loading-rate-dependent mechanoluminescence of $SrAl_2O_4:Eu^{2+},Dy^{3+}$. *Optics Letters*, 34(13):1915, 2009.

[237] T. Aitasalo, P. Dereń, J. Hölsä, H. Jungner, J.-C. Krupa, M. Lastusaari, J. Legendziewicz, J. Niittykoski, and W. Stręk. Persistent luminescence phenomena in materials doped with rare earth ions. *Journal of Solid State Chemistry*, 171(1-2):114–122, 2003.

[238] T. Aitasalo, J. Hölsä, H. Jungner, M. Lastusaari, and J. Niittykoski. Thermoluminescence Study of Persistent Luminescence Materials: Eu^{2+}- and R^{3+}-Doped Calcium Aluminates, $CaAl_2O_4:Eu^{2+},R^{3+}$. *Journal of Physical Chemistry B*, 110(10):4589–4598, 2006.

[239] P. Dorenbos. Mechanism of Persistent Luminescence in Eu^{2+} and Dy^{3+} Codoped Aluminate and Silicate Compounds. *Journal of The Electrochemical Society*, 152(7):H107–H110, 2005.

[240] C. Pereyda-Pierre, R. Meléndrez, R. García, M. Pedroza-Montero, and M. Barboza-Flores. Persistent luminescence and thermoluminescence of UV/VIS -irradiated $SrAl_2O_4$: Eu^{2+}, Dy^{3+} phosphor. *Radiation Measurements*, 46(12):1417–1420, 2011.

[241] D. O. A. dos Santos, L. Giordano, M. A. S. G. Barbara, M. C. Portes, C. C. S. Pedroso, V. C. Teixeira, M. Lastusaari, and L. C. V. Rodrigues. Abnormal co-doping effect on the red persistent luminescence srs:eu2+,re3+ materials. *Dalton Transactions*, 49(45):16386–16393, 2020.

[242] K. Korthout, K. Van den Eeckhout, J. Botterman, S. Nikitenko, D. Poelman, and P. F. Smet. Luminescence and x-ray absorption measurements of persistent $SrAl_2O_4$:Eu,Dy powders: Evidence for valence state changes. *Physical Review B*, 84(8):085140, 2011.

[243] J. J. Joos, K. Korthout, L. Amidani, P. Glatzel, D. Poelman, and P. F. Smet. Identification of Dy^{3+}/Dy^{2+} as Electron Trap in Persistent Phosphors. *Physical Review Letters*, 125(3):033001, 2020.

[244] T. Delgado, N. Gartmann, B. Walfort, F. LaMattina, M. Pollnau, A. Rosspeintner, J. Afshani, J. Olchowka, and H. Hagemann. Fundamental Loading-Curve Characteristics of the Persistent Phosphor $SrAl_2O_4$:Eu^{2+},Dy^{3+},B^{3+}: The Effect of Temperature and Excitation Density. *Advanced Photonics Research*, page 2100179, 2022.

[245] J. Hölsä, H. Jungner, M. Lastusaari, and J. Niittykoski. Persistent luminescence of Eu^{2+} doped alkaline earth aluminates, MAl_2O_4:Eu^{2+}. *Journal of Alloys and Compounds*, 323-324:326–330, 2001.

[246] J. J. Joos, I. Neefjes, L. Seijo, and Z. Barandiarán. Charge Transfer from Eu^{2+} to Trivalent Lanthanide Codopants: Systematic Behavior across the Series. *Journal of Chemical Physics*, 154:064704, 2021.

[247] J. J. Joos, D. Van der Heggen, L. Amidani, L. Seijo, and Z. Barandiarán. Elucidation of the electron transfer mechanism in Eu^{2+} and Sm^{3+} codoped CaF_2: A step towards better understanding of trapping and detrapping in luminescent materials. *Physical Review B*, 104:L201108, 2021.

[248] J. Hölsä, T. Aitasalo, H. Jungner, M. Lastusaari, J. Niittykoski, and G. Spano. Role of defect states in persistent luminescence materials. *Journal of Alloys and Compounds*, 374(1-2):56–59, 2004.

[249] T. Takeyama, T. Nakamura, N. Takahashi, and M. Ohta. Electron paramagnetic resonance studies on the defects formed in the Dy(III)-doped $SrAl_2O_4$. *Solid State Sciences*, 6(4):345–348, 2004.

[250] B. F. Dos Santos, M. V. Dos Santos Rezende, P. J. Montes, R. M. Araujo, M. A. Dos Santos, and M. E. Valerio. Spectroscopy study of SrAl 2O 4:Eu 3+. *Journal of Luminescence*, 132(4):1015–1020, 2012.

[251] J. Bierwagen, T. Delgado, J. Afshani, S. Yoon, N. Gartmann, B. Walfort, and H. Hagemann. Observation of multiple sites for trivalent europium ions in $SrAl_2O_4$. *Journal of Luminescence*, 239:118348, 2021.

[252] J. M. Johnson, H.-L. Huang, M. Wang, S. Mu, J. B. Varley, A. F. M. A. U. Bhuiyan, Z. Feng, N. K. Kalarickal, S. Rajan, H. Zhao, C. G. V. d. Walle, and J. Hwang. Atomic scale investigation of aluminum incorporation, defects, and phase stability in β-$(Al_xGa_{1-x})_2O_3$ films. *APL Materials*, 9(5):051103, 2021.

[253] B. Lou, J. Wen, L. Ning, M. Yin, C.-G. Ma, and C.-K. Duan. Understanding the defect levels and photoluminescence in a series of bismuth-doped perovskite oxides: First-principles study. *Physical Review B*, 104:115101, 2021.

[254] W. Jing, M. Liu, J. Wen, L. Ning, M. Yin, and C.-K. Duan. First-principles study of ti-doped sapphire. ii. formation and reduction of complex defects. *Physical Review B*, 104:165104, 2021.

[255] C. Freysoldt, B. Grabowski, T. Hickel, J. Neugebauer, G. Kresse, A. Janotti, and C. G. Van de Walle. First-principles calculations for point defects in solids. *Reviews of Modern Physics*, 86(1):253–305, 2014.

[256] E. Finley, A. Mansouri Tehrani, and J. Brgoch. Intrinsic Defects Drive Persistent Luminescence in Monoclinic $SrAl_2O_4$. *The Journal of Physical Chemistry C*, 122(28):16309–16314, 2018.

[257] W. Lafargue-Dit-Hauret, C. Latouche, B. Viana, M. Allix, and S. Jobic. First-Principles Calculations to Identify Key Native Point Defects in $Sr_4Al_{14}O_{25}$. *Physical Chemistry Chemical Physics*, 24:2482–2490, 2022.

[258] P. W. Anderson. Model for Electronic-Structure of Amorphous-Semiconductors. *Physical Review Letters*, 34(15):953–955, 1975.

[259] Y.-C. Lin, P. Erhart, M. Bettinelli, N. C. George, S. F. Parker, and M. Karlsson. Understanding the Interactions between Vibrational Modes and Excited State Relaxation in $Y_{3-x}Ce_xAl_5O_{12}$: Design Principles for Phosphors Based on $5d- - 4f$ Transitions. *Chemistry of Materials*, 30(6):1865–1877, 2018.

[260] M. P. Prange, N. Govind, and S. N. Kerisit. Ab Initio Calculations of the Rate of Carrier Trapping and Release at Dopant Sites in NaI:Tl Beyond the Harmonic Approximation. *Physical Review. B*, 101:024304, 2020.

[261] J. I. Pankove and N. M. Johnson. *Hydrogen in Semiconductors*, volume 34. Academic Press, 1991.

[262] C. G. Van de Walle and J. Neugebauer. Hydrogen in Semiconductors. *Annual Review of Materials Research*, 36(1):179–198, 2006.

[263] T. Aitasalo, J. Hassinen, J. Hölsä, T. Laamanen, M. Lastusaari, M. Malkamäki, J. Niittykoski, and P. Novák. Synchrotron radiation investigations of the $Sr_2MgSi_2O_7$:Eu^{2+},R^{3+} persistent luminescence materials. *Journal of Rare Earths*, 27(4):529–538, 2009.

[264] S. Carlson, J. Hölsä, T. Laamanen, M. Lastusaari, M. Malkamäki, J. Niittykoski, and R. Valtonen. X-ray absorption study of rare earth ions in $Sr_2MgSi_2O_7$:Eu^{2+},R^{3+} persistent luminescence materials. *Optical Materials*, 31(12):1877–1879, 2009.

[265] M. Lastusaari, H. F. Brito, S. Carlson, J. Hölsä, T. Laamanen, L. C. Rodrigues, and E. Welter. Valences of dopants in Eu^{2+} persistent luminescence materials. *Physica Scripta*, 89(4):044004, 2014.

[266] D. S. McClure and C. Pedrini. Excitons Trapped at Impurity Centers in Highly Ionic-Crystals. *Physical Review B*, 32(12):8465–8468, 1985.

[267] G. Sánchez-Sanz, L. Seijo, and Z. Barandiarán. Yb^{2+}-Doped $SrCl_2$: Electronic Structure of Impurity States and Impurity-Trapped Excitons. *Journal of Chemical Physics*, 133(11):114509, 2010.

[268] P. S. Senanayake, J. P. R. Wells, M. F. Reid, G. Berden, A. Meijerink, and R. J. Reeves. Impurity-Trapped Excitons and Electron Traps in CaF_2:Yb^{2+} and SrF_2:Yb^{2+} Probed by Transient Photoluminescence Enhancement. *Journal of Luminescence*, 133:81–85, 2013.

[269] C. MacKeen, F. Bridges, M. Kozina, A. Mehta, M. F. Reid, J. P. R. Wells, and Z. Barandiarán. Evidence That the Anomalous Emission from CaF_2:Yb^{2+} Is Not Described by the Impurity Trapped Exciton Model. *Journal of Physical Chemistry Letters*, 8(14):3313–3316, 2017.

[270] E. Radzhabov. Optical and Depolarization Spectroscopy of Doubly Doped Alkaline-Earth Fluorides. *Physica Status Solidi B*, 257(8):1900465, 2020.

[271] J. J. Joos, D. Poelman, and P. F. Smet. Energy Level Modeling of Lanthanide Materials: Review and Uncertainty Analysis. *Physical Chemistry Chemical Physics*, 17(29):19058–19078, 2015.

[272] D. R. Hartree. The Wave Mechanics of an Atom with a Non-Coulomb Central Field. Part I. Theory and Methods. *Mathematical Proceedings of the Cambridge Philosophical Society*, 24(1):89–110, 1928.

[273] V. Fock. Näherungsmethode zur Lösung des quantenmechanischen Mehrkörperproblems. *Zeitschrift für Physik*, 61(1):126–148, 1930.

[274] J. E. Lennard-Jones. The Electronic Structure of Some Diatomic Molecules. *Transactions of the Faraday Society*, 25(0):668–686, 1929.

[275] J. S. Griffith and L. E. Orgel. Ligand-field theory. *Quarterly Reviews Chemical Society*, 11(4):381–393, 1957.

[276] F. Bloch. Über die Quantenmechanik der Elektronen in Kristallgittern. *Zeitschrift für Physik*, 52(7):555–600, 1929.

[277] L. Brillouin. Les Electrons Libres dans les Métaux et le Role des Réflexions de Bragg. *Journal de Physique et Le Radium*, 1(11):377–400, 1930.

[278] A. Sommerfeld. Zur Elektronentheorie der Metalle auf Grund der Fermischen Statistik. *Zeitschrift für Physik*, 47(1):1–32, 1928.

[279] E. Wigner. On the Interaction of Electrons in Metals. *Physical Review*, 46:1002–1011, 1934.

[280] P.-O. Löwdin. Quantum Theory of Many-Particle Systems. III. Extension of the Hartree-Fock Scheme to Include Degenerate Systems and Correlation Effects. *Physical Review*, 97:1509–1520, 1955.

[281] N. F. Mott. The Basis of the Electron Theory of Metals, with Special Reference to the Transition Metals. *Proceedings of the Physical Society*, 62(7):416–422, 1949.

[282] J. Hubbard and B. H. Flowers. Electron Correlations in Narrow Energy Bands. *Proceedings of the Royal Society of London. Series A*, 276(1365):238–257, 1963.

[283] L. González, D. Escudero, and L. Serrano-Andrés. Progress and Challenges in the Calculation of Electronic Excited States. *ChemPhysChem*, 13(1):28–51, 2012.

[284] H. Lischka, D. Nachtigallová, A. J. A. Aquino, P. G. Szalay, F. Plasser, F. B. C. Machado, and M. Barbatti. Multireference Approaches for Excited States of Molecules. *Chemical Reviews*, 118(15):7293–7361, 2018.

[285] M. C. Böhm. On the Quantum Chemical Origin for the Nonvalidity of Koopmans' Theorem in Transitionmetal Compounds. *Theoretica chimica acta*, 61(6):539–558, 1982.

[286] J. M. Luttinger and W. Kohn. Motion of Electrons and Holes in Perturbed Periodic Fields. *Physical Review*, 97:869–883, 1955.

[287] G. F. Koster and J. C. Slater. Wave Functions for Impurity Levels. *Physical Review*, 95(5):1167–1176, 1954.

[288] G. F. Koster and J. C. Slater. Simplified Impurity Calculation. *Physical Review*, 96(5):1208–1223, 1954.

[289] W. Shockley and J. T. Last. Statistics of the Charge Distribution for a Localized Flaw in a Semiconductor. *Physical Review*, 107:392–396, 1957.

[290] P. Dorenbos. Valence Stability of Lanthanide Ions in Inorganic Compounds. *Chemistry of Materials*, 17(25):6452–6456, 2005.

[291] P. Dorenbos. Charge Transfer Bands in Optical Materials and Related Defect Level Location. *Optical Materials*, 69:8–22, 2017.

[292] A. von Hippel. Einige Prinzipielle Gesichtspunkte zur Spektroskopie der Ionenkristalle und ihre Anwendung auf die Alkalihalogenide. *Zeitschrift für Physik*, 101(11):680–720, 1936.

[293] F. Seitz. Interpretation of the Properties of Alkali Halide-Thallium Phosphors. *Journal of Chemical Physics*, 6(3):150–162, 1938.

[294] N. F. Mott. On the Absorption of Light by Crystals. *Proceedings of the Royal Society of London. Series A*, 167(930):384–391, 1938.

[295] S. B. Piepho, E. R. Krausz, and P. N. Schatz. Vibronic Coupling Model for Calculation of Mixed Valence Absorption Profiles. *Journal of the American Chemical Society*, 100(10):2996–3005, 1978.

[296] G. Dieke, H. Crosswhite, and H. Crosswhite. *Spectra and energy levels of rare earth ions in crystals*. Interscience Publishers, 1968.

[297] Y. Tanabe and S. Sugano. On the Absorption Spectra of Complex Ions. I. *Journal of the Physical Society of Japan*, 9(5):753, 1954.

[298] Y. Tanabe and S. Sugano. On the Absorption Spectra of Complex Ions II. *Journal of the Physical Society of Japan*, 9(5):766, 1954.

[299] Y. Tanabe and S. Sugano. On the Absorption Spectra of Complex Ions, .III. The Calculation of the Crystalline Field Strength. *Journal of the Physical Society of Japan*, 11(8):864–877, 1956.

[300] Y. Tanabe and H. Kamimura. On the Absorption Spectra of Complex Ions .IV. The Effect of the Spin-Orbit Interaction and the Field of Lower Symmetry on d Electrons in Cubic Field. *Journal of the Physical Society of Japan*, 13(4):394–411, 1958.

[301] H. Bethe. Termaufspaltung in Kristallen. *Annalen der Physik*, 395(2):133–208, 1929.

[302] J. H. Van Vleck. Theory of the Variations in Paramagnetic Anisotropy Among Different Salts of the Iron Group. *Physical Review*, 41(2):208–215, 1932.

[303] C. W. Struck and W. H. Fonger. Unified Model of Temperature Quenching of Narrow-Line and Broad-Band Emissions. *Journal of Luminescence*, 10(1):1–30, 1975.

[304] W. Hoogenstraaten. Electron Traps in Zinc-Sulphide Phosphors. *Philips Res. Rep.*, 13(R357):515–693, 1958.

[305] F. E. Williams. Theory of the energy levels of donor-acceptor pairs. *Journal of Physics and Chemistry of Solids*, 12(3):265–275, 1960.

[306] Z. Barandiarán, A. Meijerink, and L. Seijo. Configuration coordinate energy level diagrams of intervalence and metal-to-metal charge transfer states of dopant pairs in solids. *Physical Chemistry and Chemical Physics*, 17:19874–19884, 2015.

[307] F. A. Kröger and H. J. Vink. Relations between the concentrations of imperfections in crystalline solids. *Solid State Physics*, 3:307–435, 1956.

[308] N. S. Hush. Distance dependence of electron transfer rates. *Coordination Chemistry Reviews*, 64:135–157, 1985.

[309] J.-P. Launay. Long-Distance Intervalence Electron Transfer. *Chemical Society Reviews*, 30(6):386–397, 2001.

[310] A. Zych, J. Ogieglo, C. Ronda, C. D. Donega, and A. Meijerink. Analysis of the shift of zero-phonon lines for f-d luminescence of lanthanides in relation to the dorenbos model. *Journal of Luminescence*, 134:174–179, 2013.

[311] I. Neefjes, J. J. Joos, Z. Barandiarán, and L. Seijo. Mixed-Valence Lanthanide-Activated Phosphors: Invariance of the Intervalence Charge Transfer (IVCT) Absorption Onset across the Series. *The Journal of Physical Chemistry C*, 2020.

[312] J. J. Joos, D. Van der Heggen, L. Martin, L. Amidani, P. F. Smet, Z. Barandiarán, and L. Seijo. Broadband Infrared LEDs Based on Europium-to-Terbium Charge Transfer Luminescence. 11:3647, 2020.

[313] N. F. Mott. On the absorption of light by crystals. *Proceedings of the Royal Society of London. Series A. Mathematical and Physical Sciences*, 167(930):384–391, 1938.

[314] P. M. Morse and E. C. G. Stueckelberg. Lösung des Eigenwertproblems eines Potentialfeldes mit Zwei Minima. *Helvetica Physica Acta*, 4:337, 1931.

[315] K. S. Gilroy and W. A. Phillips. An asymmetric double-well potential model for structural relaxation processes in amorphous materials. *Philosophical Magazine B*, 43(5):735–746, 1981.

[316] A. J. Atkins and L. González. Trajectory Surface-Hopping Dynamics Including Intersystem Crossing in $[Ru(bpy)_3]^{2+}$. *Journal of Physical Chemistry Letters*, 8(16):3840–3845, 2017.

[317] F. Plasser, S. Gómez, M. F. S. J. Menger, S. Mai, and L. González. Highly Efficient Surface Hopping Dynamics Using a Linear Vibronic Coupling Model. *Physical Chemistry Chemical Physics*, 21(1):57–69, 2019.

[318] S. Mai, M. F. S. J. Menger, M. Marazzi, D. L. Stolba, A. Monari, and L. González. Competing Ultrafast Photoinduced Electron Transfer and Intersystem Crossing of $[Re(CO)_3(Dmp)(His124)(Trp122)]^+$ in Pseudomonas Aeruginosa Azurin: A Nonadiabatic Dynamics Study. *Theoretica chimica acta*, 139(3):65, 2020.

[319] C. W. Struck and W. H. Fonger. Unified Model of Temperature Quenching of Narrow-Line and Broad-Band Emissions. *Journal of Luminescence*, 10(1):1–30, 1975.

[320] C. W. Struck and W. H. Fonger. Temperature Quenching of Luminescence for Linear and Derivative Nuclear Operators. *Journal of Luminescence*, 14(4):253–279, 1976.

[321] C. Koepke, A. Lempicki, and A. J. Wojtowicz. Luminescence Quenching of Strongly Coupled Systems. *Physica Status Solidi B*, 179(1):233–240, 1993.

[322] Y. Murayama, S. Watanabe, M. Akase, and K. Matsui. Effects of composition and reduction conditions on persistent luminescence of $sral_2o_4$:eu,dy prepared via a solid-state reaction. *Journal of Luminescence*, 251:119248, 2022.

[323] S. P. Keller, J. E. Mapes, and G. Cheroff. Studies on Some Infrared Stimulable Phosphors. *Physical Review*, 108:663–676, 1957.

[324] S. P. Keller and G. D. Pettit. Quenching, Stimulation, and Exhaustion Studies on Some Infrared Stimulable Phosphors. *Physical Review*, 111:1533–1539, 1958.

[325] A. H. Krumpel, E. van der Kolk, D. Zeelenberg, A. J. J. Bos, K. W. Krämer, and P. Dorenbos. Lanthanide 4f-level location in lanthanide doped and cerium-lanthanide codoped $NaLaF_4$ by photo- and thermoluminescence. *Journal of Applied Physics*, 104(7):073505, 2008.

[326] A. H. Krumpel, A. J. J. Bos, A. Bessiere, E. van der Kolk, and P. Dorenbos. Controlled Electron and Hole Trapping in YPO_4:Ce^{3+},Ln^{3+} and LuPO4:Ce^{3+},Ln^{3+} (Ln=Sm, Dy, Ho, Er, Tm). *Physical Review B*, 80(8), 2009.

[327] H. D. Luo, A. J. J. Bos, A. Dobrowolska, and P. Dorenbos. Low-temperature VUV Photoluminescence and Thermoluminescence of UV Excited Afterglow Phosphor Sr3$Al_xSi_{1-x}O_5$:Ce^{3+}, Ln^{3+} (Ln = Er, Nd, Sm, Dy and Tm). *Physical Chemistry Chemical Physics*, 17(23):15419–15427, 2015.

[328] H. D. Luo, A. J. J. Bos, and P. Dorenbos. Controlled Electron-Hole Trapping and Detrapping Process in $GdAlO_3$ by Valence Band Engineering. *Journal of Physical Chemistry C*, 120(11):5916–5925, 2016.

[329] A. Feng, J. J. Joos, D. J., and P. F. Smet. Revealing Trap Depth Distributions in Persistent Phosphors with a Thermal Barrier for Charging. *Physical Review B*, accepted, 2022.

[330] D. Van der Heggen, J. J. Joos, D. Rodríguez Burbano, J. Capobianco, and P. F. Smet. Counting the Photons: Determining the Absolute Storage Capacity of Persistent Phosphors. *Materials*, 10(8):867, 2017.

[331] T. Nakanishi, Y. Katayama, J. Ueda, T. Honma, S. Tanabe, and T. Komatsu. Fabrication of Eu:$SrAl_2O_4$-based glass ceramics using Frozen sorbet method. *Journal of the Ceramic Society of Japan*, 119(7):609–615, 2011.

[332] T. Nakanishi, K. Watanabe, J. Ueda, K. Fushimi, S. Tanabe, and Y. Hasegawa. Enhanced Light Storage of $SrAl_2O_4$ Glass-Ceramics Controlled by Selective Europium Reduction. *Journal of the American Ceramic Society*, 98(2):423–429, 2015.

[333] Y. G. Alves, D. V. Sampaio, N. R. Souza, D. C. Silva, T. R. Cunha, C. T. Meneses, E. J. Fonseca, and R. S. Silva. Persistent luminescence properties of $SrB_XAl_{2-X}O_4$:Eu,Dy laser-sintered ceramics. *Optical Materials*, 70:63–68, 2017.

[334] B. Walfort, N. Gartmann, J. Afshani, A. Rosspeintner, and H. Hagemann. Effect of excitation wavelength (blue vs near UV) and dopant concentrations on afterglow and fast decay of persistent phosphor $SrAl_2O_4$:Eu^{2+},Dy^{3+}. *Journal of Rare Earths*, page doi: 10.1016/j.jre.2021.07.014., 2021.

[335] B. Yang and P. D. Townsend. Patterns of glow peak movement in rare earth doped lanthanum fluoride. *Journal of Applied Physics*, 88(11):6395–6402, 2000.

[336] T. D. Dunbar, W. L. Warren, B. A. Tuttle, C. A. Randall, and Y. Tsur. Electron paramagnetic resonance investigations of lanthanide-doped barium titanate: Dopant site occupancy. *Journal of Physical Chemistry B*, 108(3):908–917, 2004.

[337] L. Yuan, Y. Jin, Y. Su, H. Wu, Y. Hu, and S. Yang. Optically Stimulated Luminescence Phosphors: Principles, Applications, and Prospects. *Laser & Photonics Reviews*, 14:2000123, 2020.

[338] M. Autzen, N. R. Poolton, A. S. Murray, M. Kook, and J. P. Buylaert. A new automated system for combined luminescence and exo-electron measurements. *Nuclear Instruments and Methods in Physics Research Section B: Beam Interactions with Materials and Atoms*, 443:90–99, 2019.

[339] T. Stassin, R. Verbeke, A. John Cruz, S. Rodríguez-Hermida, I. Stassen, J. Marreiros, M. Krishtab, M. Dickmann, W. Egger, I. F. J Vankelecom, S. Furukawa, D. De Vos, D. Grosso, M. Thommes, and R. Ameloot. Porosimetry for Thin Films of Metal–Organic Frameworks: A Comparison of Positron Annihilation Lifetime Spectroscopy and Adsorption-Based Methods. *Advanced Materials*, 33(17):2006993, 2021.

[340] S. Mai and L. González. Molecular Photochemistry: Recent Developments in Theory. *Angewandte Chemie, International Edition*, 59(39):16832–16846, 2020.